NUMERICAL INVESTIGATION OF A SINGLE BUBBLE AND A PAIR OF BUBBLES RISING IN NEWTONIAN AND NON NEWTONIAN FLUIDS WITH INTERFACIAL PASSIVE SCALAR TRANSFER

Koorosh Kazemi

UNIVERSITAT
ROVIRA i VIRGILI

Numerical investigation of a single bubble and a pair of bubbles rising in Newtonian and non-Newtonian fluids with interfacial passive scalar transfer

---

Koorosh Kazemi

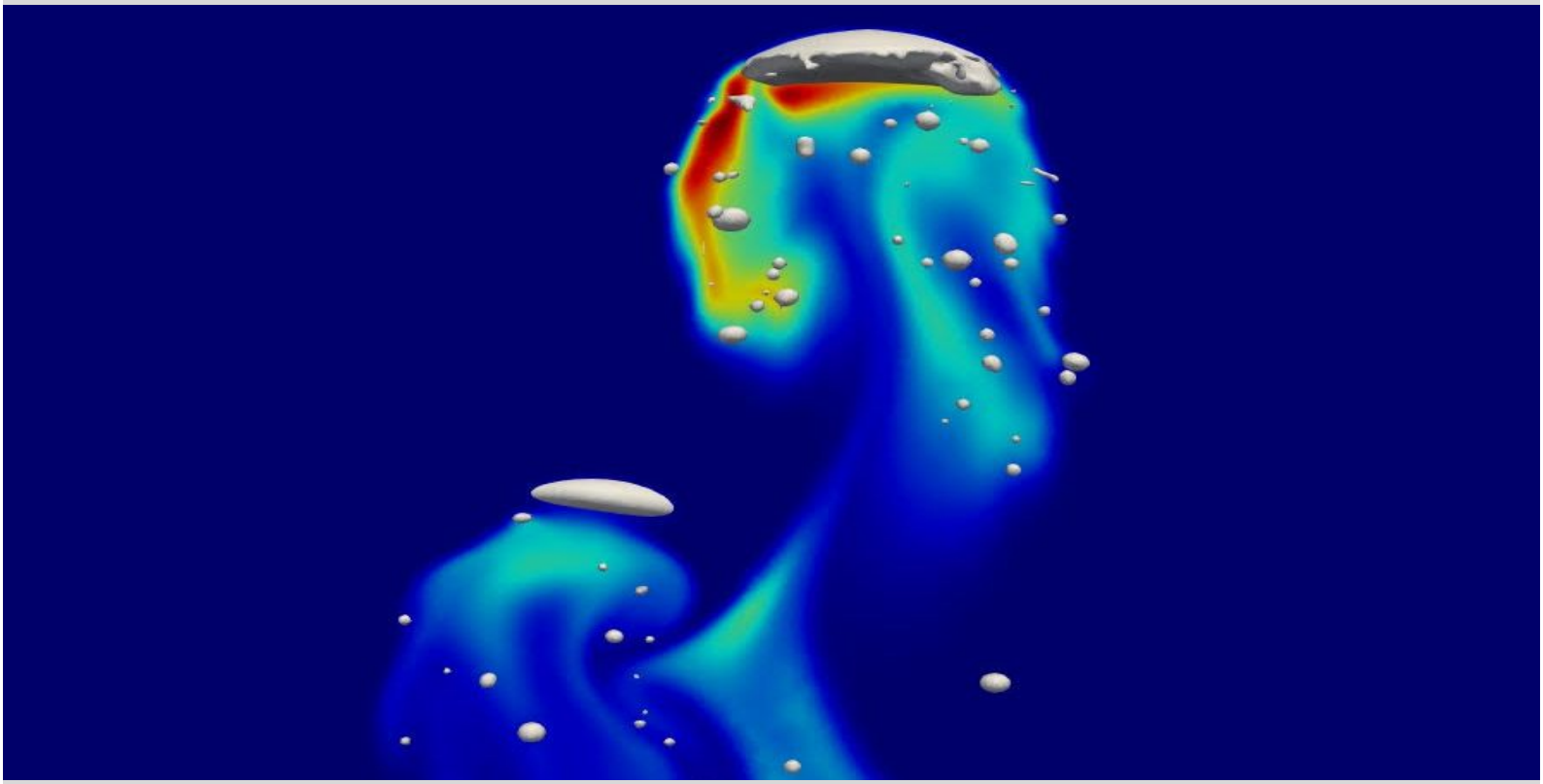

DOCTORAL THESIS
2023

UNIVERSITAT ROVIRA I VIRGILI,
NUMERICAL INVESTIGATION OF A SINGLE BUBBLE AND A PAIR OF BUBBLES RISING IN NEWTONIAN AND NON NEWTONIAN FLUIDS WITH INTERFACIAL PASSIVE SCALAR TRANSFER
Koorosh Kazemi

UNIVERSITAT
ROVIRA i VIRGILI

Numerical investigation of a single bubble and a pair of bubbles rising in Newtonian and non-Newtonian fluids with interfacial passive scalar transfer

DOCTORAL THESIS

Author:
KOOROSH KAZEMI

Supervisors:
Dr. SALVATORE CITO
Dr. ANTON VERNET
Dr. ALEXANDRE FABREGAT

A thesis submitted in fulfillment of the requirements
for the degree of Doctor of Philosophy

in the

Departament d'Enginyeria Mecànica

UNIVERSITAT ROVIRA I VIRGILI

May 15, 2023

UNIVERSITAT ROVIRA I VIRGILI,
NUMERICAL INVESTIGATION OF A SINGLE BUBBLE AND A PAIR OF BUBBLES RISING IN NEWTONIAN AND NON NEWTONIAN FLUIDS WITH INTERFACIAL PASSIVE SCALAR TRANSFER
Koorosh Kazemi

Declaration of Authorship

We state that the present study, entitled: **"Numerical investigation of a single bubble and a pair of bubbles rising in Newtonian and non-Newtonian fluids with interfacial passive scalar transfer"** presented by KOOROSH KAZEMI for the award of Doctor of Philosophy, has been carried out under our supervision at the Department of Mechanical Engineering of Rovira i Virgili university.

Tarragona, March 31, 2023

Supervised by:

Dr. SALVATORE CITO

Dr. ANTON VERNET

Dr. ALEXANDRE FABREGAT

UNIVERSITAT ROVIRA I VIRGILI,
NUMERICAL INVESTIGATION OF A SINGLE BUBBLE AND A PAIR OF BUBBLES RISING IN NEWTONIAN AND NON NEWTONIAN FLUIDS WITH INTERFACIAL PASSIVE SCALAR TRANSFER
Koorosh Kazemi

UNIVERSITAT ROVIRA I VIRGILI

Abstract

Departament d'Enginyeria Mecànica

Doctor of Philosophy

Numerical investigation of a single bubble and a pair of bubbles rising in Newtonian and non-Newtonian fluids with interfacial passive scalar transfer

by KOOROSH KAZEMI

Bubble rising and heat/mass transfer in bubble rising are important phenomena in many industrial processes such as wastewater treatment, fermentation, and chemical reactions. Understanding the behavior of bubbles and their interaction with fluids is crucial for optimizing the efficiency of these processes. In wastewater treatment, for example, bubbles are introduced to increase the transfer of oxygen from the gas phase to the liquid phase, which promotes the growth of microorganisms and enhances the efficiency of the treatment. In fermentation, bubbles are introduced to provide oxygen and remove carbon dioxide, which is important for cell growth and product formation. In chemical reactions, bubbles can be used to mix reactants and facilitate heat transfer, which can enhance reaction rates and product yields. Therefore, the study of bubble rising and mass transfer in bubble rising has significant implications for various industrial processes and can contribute to the development of more efficient and sustainable technologies.

This doctoral thesis comprises two main parts: a numerical investigation of a single gas bubble rising in different types of fluids, and an analysis of a pair of bubbles rising in-line in two types of fluids. The first part considers Newtonian, shear-thinning, and shear-thickening fluids and analyzes the effects of Peclet number and rheological properties on the transfer of a scalar across the bubble interface. The second part investigates heat/mass transfer in Newtonian and shear-thinning fluids and analyzes the effects of several parameters, including Galilei and Bond numbers, bubble pair radius ratio, inelastic time constant, and flow index. The simulation is

carried out using Basilisk, with adaptive mesh refinement techniques dependent on the velocity magnitude, passive scalar value, and interface position.

The findings reveal that for a single bubble, the rising dynamics are strongly influenced by the flow index. For example, the bubble trajectory in shear-thinning fluids exhibits an oscillatory path, while in Newtonian and shear-thickening fluids, the bubble rises along the vertical axis. Moreover, the viscosity field and bubble shape are significantly affected by the rheological properties of the fluid. Furthermore, the results show that the mass transfer rate increases with the Peclet number and is highly dependent on the flow index. A reduction in the flow index of the ambient fluid leads to a higher degree of deformation of the rising bubble and an increase in its velocity, which in turn, results in an increase in the heat/mass transfer rates across the bubble interface. Moreover, a correlation is proposed in this study that relates the surface-averaged Sherwood number to both the flow index and the Peclet number.

The investigation of a pair of bubbles rising in different types of fluids provides crucial insights into the interplay between the dynamics of multiple bubbles and their surrounding fluid medium, particularly in non-Newtonian rheologies. The study revealed that the behavior of two bubbles rising in-line is characterized by various motion patterns, and a new scenario of coalescence-breakup is introduced. The analysis highlights the complex interactions between different regimes and the dynamic behavior of bubbles in different fluid media. The results show that the heat/mass transfer rate is optimized in regimes where the bubbles follow side escape or Drafting-Kissing-Tumbling scenarios. The radius ratio of the leading to trailing bubble has a significant impact on the behavior of bubbles during rising. Additionally, the study highlights that the inelastic time constant influences the behavior of bubbles during rising, leading to more instability and oscillatory motion of the bubbles. The study also revealed that the flow index is a crucial rheological parameter that affects the behavior of bubbles, and decreasing the flow index leads to an increase in the instabilities of the bubble during rising. These findings provide valuable insights into the complex behavior of bubbles in non-Newtonian fluids, with implications for a range of industrial processes.

Acknowledgements

Firstly, I am extremely grateful to my supervisors, Prof. Salvatore Cito, Prof. Anton Vernet, and Prof. Alexandre Fabregat for their invaluable advice, continuous support, patience, and guidance me well throughout the research work from title's selection to finding the results and discussing them. Their immense knowledge and plentiful experience have encouraged me in all the time of my academic research and daily life. I could not have imagined having a better advisor and mentor for my Ph.D. study.

Besides my supervisors, I will not forget to express my gratitude to the rest of the ECoMMFIT research group, especially Prof. Francesc X. Grau, and Prof. Jordi Pallarès for their insightful comments and encouragement, but also for the hard question which incented me to widen my research from various perspectives.

I am also pleased to say thanks to Mr. Lluís Vàzquez and Ms. Núria Juanpere for their technical and logistical assistance throughout my research. This would not have been possible without their help.

Moreover, I would like to thank jury committee members, who so generously took time out of their schedules to read the dissertation and present valuable comments.

My sincere thanks also goes to Prof. Marc Avila, who provided me an opportunity to join his team as an intern, and who gave me access to the laboratory and research facilities.

I also thank my fellow labmates and friends (Mohsen Goraki Fard, Mohammad Javad Norouzi, Masoud Norouzi, and Jordi Iglesias) for the stimulating discussions, for thier comments, and for all the fun we have had in the last four years.

I would like to acknowledge the generous financial support by the Spanish Ministerio de Ciencia, Innovación y Universidades through the grants DPI2016-75791-C2-1-P and RTI2018-100907-A-I00 (MCIU/AEI/FEDER, UE) and also by the Generalitat de Catalunya through the grant 2017-SGR-1234.

Last but not the least, I would like to thank my father, my wife, and my brother for supporting me spiritually throughout writing this thesis and my life in general.

I consider myself nothing without them. They gave me enough moral support, encouragement, and motivation to accomplish my personal goals.

Contents

List of Figures

List of Tables

UNIVERSITAT ROVIRA I VIRGILI,
NUMERICAL INVESTIGATION OF A SINGLE BUBBLE AND A PAIR OF BUBBLES RISING IN NEWTONIAN AND NON NEWTONIAN FLUIDS WITH INTERFACIAL PASSIVE SCALAR TRANSFER
Koorosh Kazemi

List of Abbreviations

Roman Symbols

A	bubble interface area
Bo	Bond number
CB	**C**oalescence-**B**reakup
CLSVOF	**C**oupled **L**evel-**S**et **V**olume **O**f **F**luid
CMC	**C**arboxy**M**ethyl **C**ellulose
d	non-dimensional diameter of the bubble
DKT	**D**rafting-**K**issing-**T**umbling
f	volume fraction of fluid
FFT	**F**ast **F**ourier **T**ransfer
g	gravitational acceleration
Ga	Galilei number
n	flow index
NSE	**N**avier-**S**tokes **E**quations
L	non-dimensional length of the cube
LB	**L**eading **B**ubble
MB	**M**erged **B**ubble
NRCH	**N**umerical **R**esults of **CH**akraborty et al.
p	non-dimensional pressure
Pe	Peclet number
R	non-dimensional radius of the bubble
Re	Reynolds number
SB	**S**ingle **B**ubble
Sh	Sherwood number

t	non-dimensional time
TB	**T**railing **B**ubble
$\mathbf{u}$	non-dimensional velocity vector
u, v, w	velocity components in the x, y, and z directions, respectively
VOF	**V**olume **O**f **F**luid
x, y, z	Cartesian coordinate system directions

Greek Symbols

δ	dirac delta function
λ	inelastic time constant
μ	dynamic viscosity
ν	kinematic viscosity
ρ	density
σ	surface tension coefficient
ϕ	passive scalar

Other Symbols and operators

A_0	initial bubble interface area
$\mathcal{D}$	passive scalar diffusion coefficient
$\boldsymbol{\jmath}$	unit vector in the vertical direction
l^*	non-dimensionalized length scale
u^*	non-dimensionalized velocity scale
p^*	non-dimensionalized pressure scale
ρ^*	density ratio
μ^*	viscosity ratio
R_r	bubble pair radius ratio
$\vec{\mathbf{n}}$	outward-pointing unit normal vector to the fluid interface
$\|\|V\|\|$	bubble rising velocity magnitude
∇	gradient differential operator

∂	partial derivative
$\tilde{\kappa}$	interfacial curvature
$\langle Sh \rangle$	surface-averaged Sherwood number
q_ϕ	density flux of scalar ϕ
$\langle \phi_s \rangle$	surface-average value of scalar ϕ

Subscripts

a_A	variable a of fluid A
a_B	variable a of fluid B
a_{LB}	variable a of leading bubble
a_{TB}	variable a of trailing bubble

Superscripts

$\tilde{\mathbf{a}}$	dimensional form of variable a

UNIVERSITAT ROVIRA I VIRGILI,
NUMERICAL INVESTIGATION OF A SINGLE BUBBLE AND A PAIR OF BUBBLES RISING IN NEWTONIAN AND NON NEWTONIAN FLUIDS WITH INTERFACIAL PASSIVE SCALAR TRANSFER
Koorosh Kazemi

*I am dedicating this thesis to my beloved people my **Father**, **Wife**, and **Brother**. Love you so much. ♡♡♡*

UNIVERSITAT ROVIRA I VIRGILI,
NUMERICAL INVESTIGATION OF A SINGLE BUBBLE AND A PAIR OF BUBBLES RISING IN NEWTONIAN AND NON NEWTONIAN FLUIDS WITH INTERFACIAL PASSIVE SCALAR TRANSFER
Koorosh Kazemi

Chapter 1

Introduction

1.1 Overview

The study of the bubbles, which act as interfaces between gas and gas or liquid phases, originated from the need to comprehend various phenomena and applications in fields such as aerosol transfer from sea (*1*), underwater explosions (*2*), oxygen dissolution in freshwater (*3*), gas-liquid reactors (*4*), metallurgical and nuclear power systems (*5*, *6*), jet stability and cavitation in ship propellers and pumps (*7*–*10*), microfluidic transport (*11*), gas-liquid contact equipment such as bubble column reactors and stirred tanks reactors (*12*, *13*), wastewater treatment (*14*), aerobic fermentation (*15*), CO_2 storage (*16*), combustion (*17*, *18*), spray drying (*19*), pharmaceutical industry (*20*), enhanced oil recovery in petroleum industry (*21*), production of polymeric alloys (*22*), and algae growth (*23*), all of which have a high potential for efficiency improvement if we obtain a better knowledge of the phenomenon. Bubbles are often employed in these circumstances because they provide an excellent rate of heat/mass transfer between the gas bubble and the liquid phase as well as minimal maintenance costs due to their ease of fabrication (*24*, *25*). The size, shape, and rising velocity of the bubble, bubble coalescence and breakup, liquid phase rheology, and other factors all influence effective heat/mass transfer. Since bubbles are often not rigid, their deformation changes the interfacial area, which influences bubble hydrodynamics, motion trajectories, and the efficiency of interfacial heat/mass transfer (*26*, *27*). The number of bubbles is also one of the controlling criteria that greatly impacts the transfer efficiency in heat/mass transfer. The buoyancy, external and internal circulations of the two fluids (the inertial and viscous forces), and the

interface forces between two phases (surface tension, surface charge force, and so on) all influence the interdependence of bubble topology, flow hydrodynamics, and transfer coefficient (*28*). A gas bubble's generation, mobility, and deformation are all extremely dynamic behaviors, the outcomes of which are determined not only by the nature of the interface but also by the environment fluid. Despite the fact that carrier fluids are frequently defined as Newtonian, the majority of the aforementioned applications work with non-Newtonian fluids that exhibit shear-thinning or shear-thickening characteristics (*29*–*31*). The majority of fluids encountered in nature or industry are non-Newtonian, such as chemical reactants, polymers, blood, slurries, proteins, emulsions, suspensions, and so on (*32*). Non-Newtonian fluids have numerous applications, including bioreactors, chemical, biochemical, and biological engineering, culinary, pharmaceutical, and petrochemical industries, and polymer manufacturing (*33*–*35*). Shear-thinning fluids, also known as pseudoplastic fluids, are the most prevalent form of time-independent non-Newtonian fluids and their apparent viscosity reduces with increasing shear rate. On the other hand, shear-thickening fluids are those whose apparent viscosity rises as the shear rate does. Shear-thinning and shear-thickening fluids are utilized often in a variety of engineering applications, such as energy absorbers, vibration controllers, safety protectors, pharmaceutical, and food sectors, due to their unique properties.

Heat/mass transfer is frequently the design parameter of the processes outlined above. Consequently, the calculation of the heat/mass transfer rate is necessary for the optimal design of such equipment. It is essential to precisely predict the rising velocity of the bubble, deformation of the bubble during rising, bubbles interactions, breakup, and coalescence, surrounding fluid rheology, mass/heat transfer characteristics, and hence the performance of the equipment, for the design and optimization of equipment containing bubbly flows. Nonetheless, thorough research into heat/mass transmission in gas-liquid systems remains difficult. Advection and diffusion within each phase, as well as transfer across the interface, should be addressed when calculating the heat/mass transfer rate. Heat/mass transfer prediction can be a challenging endeavor due to bubble interactions, deformable interfaces, and changes in diffusion coefficients between phases (which could be of orders of magnitude). Experimental research encounters limitations in terms of available

measuring tools, which are either intrusive or limiting in terms of data collection. Numerical research, on the other hand, is constrained by computational capability (*36*). As processing capacity has increased, and with the help of parallel computing, numerical simulation has shown to be an excellent method for getting a fundamental knowledge of multi-phase gas-liquid flows.

Experimental measurements of the rate of carbon dioxide absorption into the water from single rising bubbles were made by Baird and Davidson (*37*). An innovative method for figuring out the mass transfer rate in specific air bubbles rising in water was developed by Bischof et al. (*38*). Ponoth and McLaughlin (*39*) proposed correlations for the Sherwood number, bubble size, and Reynolds number by statistically simulating axisymmetric rising bubbles in aqueous solutions of surfactants. The mass transfer processes in axisymmetric viscous droplets in the Newtonian fluid were studied by Feng and Michaelides (*40*) using a finite-difference method. They reported their findings on the Sherwood number's dependence on the Peclet number (ranging from 1 to 10^3) and the Reynolds number (ranging from 1 to 5×10^2). The effects of the viscosity ratio on the mass transfer of an axisymmetric bubble rising in water were numerically examined by Saboni et al. (*41*). They obtained a correlation between the surface-average Sherwood number and the Reynolds and Peclet numbers over the 1-400 and 0-10^6 ranges, respectively. Experimental research on the dissolution of carbon dioxide in a zigzagging single bubble in aqueous media was conducted by Huang and Saito (*42*), who explored the effect of water contamination on the mass transfer rate.

As previously indicated, many relevant multiphase flow applications with interfacial transport involve liquid carrier phases with non-Newtonian behavior. Barnett et al. (*43*) experimentally explored the carbon dioxide transfer in an aqueous (Newtonian) environment and in carboxymethyl cellulose (CMC) solutions (shear-thinning), demonstrating that the rheology can alter both the drag and mass transfer coefficients. Bhavaraju et al. (*44*) investigated the dependence of the Sherwood number in single bubble systems under a creeping flow regime employing power-law ambient fluids and derived correlations for the mass transfer coefficient using perturbation methods. Kishore et al. (*45*) numerically investigated the impact of the Reynolds and Peclet numbers as well as the flow index on the mass transfer

in power-law fluids under the assumptions of a spherical bubble and steady and fully developed circumstances. They were able to forecast how these characteristics would affect the surface-average Sherwood number for modest Reynolds values based on the findings. Dhole et al. (*46*) also considered power-law fluids to investigate the Sherwood number dependency of the Reynolds and Peclet numbers under the axisymmetric steady flow assumption. Using numerical simulations of a rising bubble in two-dimensional yield stress fluids and the assumption of constant mass transfer, Cao et al. (*47*) derived a correction factor to enhance the prediction of surface-averaged Sherwood numbers. Vasconcelos et al. (*48*) and Gomez-Diaz et al. (*49*) employed potential flows at high Reynolds numbers with entirely mobile surfaces in their improvements to the Sherwood number estimation. The Sherwood number for spherical bubbles was correlated throughout a wide range of regimes, from creeping flow to high Reynolds numbers, by Clift et al. (*50*). Coppus and Rietema (*51*) proposed a correlation for the mass transfer coefficient in spherical cap bubbles under the potential flow assumption. Kendoush (*52*, *53*) also researched spherical cap bubbles. The analysis was expanded to include ellipsoidal bubbles in potential flows, and a Sherwood number correlation under forced convection was revealed.

One of the most crucial problems in bubbly flows is bubble interaction between the bubbles, which can lead to significant physical processes in the system such as coalescence and breakup. Coalescence, for example, can impact the system's performance by modifying the heat/mass transfer rate induced by changing the interfacial area. The evolution, flow dynamics, and scalar transport in a system comprised of only two bubbles can be of aid to better understanding the nature of bubbly flows and enhance the design of gas-liquid apparatus.

Under various circumstances, the dynamics of a pair of rising bubbles have been examined experimentally. Two bubbles rising in-line in a viscous liquid were the subject of research by Bhaga and Weber (*54*), who presented a correlation for the wake velocity throughout a range of Reynolds numbers ($10 < Re < 100$). Katz and Meneveau (*55*) experimentally examined the rising velocity of the bubble pairs rising in water with different initial separations and different bubble diameters at the Reynolds number range between 0.2 and 35 and Bond numbers of less than 0.3.

Watanabe and Sanada (*56*) numerically and experimentally analyzed the motion of a pair of bubbles, demonstrating that at moderate Reynolds numbers ($5 < Re < 150$), there is an equilibrium distance between bubbles, although it is unstable due to three-dimensional (3D) effects. In order to determine the required Reynolds number and Weber number for the bubbles to bounce, Sanada et al. (*57*) conducted an experimental study on the coalescence of a pair of bubbles rising in silicone oil and water side by side. They also demonstrated that, upon coalescence, the bubbles' rising velocities diminish. A correlation for the drag coefficient of a single bubble for various Reynolds numbers ($50 < Re < 300$) was introduced by Kusuno and Sanada (*58*)in their experimental study of a pair of bubbles ascending in-line in ultra-pure water. They also investigated how the bubble radius affected the dynamics, which revealed four distinct motions: separating, approaching, merging, and overtaking. Experimental research was conducted by Kusuno et al. (*59*) in which they estimated the drag and lift coefficients for a Reynolds number range of 20 to 60 for two clean air bubbles rising in-line in silicone oil.

Numerical simulation has developed into a potent tool to reach in-demand characteristics and behavior of the bubble rising and bubbles interaction mechanism in various surrounding fluids. This is due to the rapid growth and development of numerical methods as well as the limitations and restrictions of experiments. Using a combined spectral/finite-difference approach, Yuan and Prosperetti (*60*) carried out a numerical analysis on an undeformable axisymmetric pair of bubbles rising in-line in a viscous fluid at Reynolds numbers up to 200. They demonstrated that the wake effect and inertial repulsion are balanced, resulting in a stable equilibrium distance between the bubbles. In order to examine the impact of initial separation on the dynamics of the bubbles, Chen et al. (*61*) employed a modified Volume-of-Fluid (VOF) approach to model the motion of a pair of initially spherical bubbles rising at Reynolds numbers up to 200 and two distinct Bond values (50 and 420). They discovered that the bubbles merge for small initial separation values, but not for big values. With two different Reynolds numbers (8.5 and 10) and four different Bond numbers (4.25, 5, 42.5, and 50), Hasan and Zakaria (*62*) used VOF to simulate the coalescence process of two in-line bubbles. Their results demonstrate that the high surface tension force delays the coalescence for a fixed value of the density and viscosity ratios.

Chen et al. (63) used the moving particle semi-implicit (MPS) approach to perform a two-dimensional numerical simulation of a pair of bubbles rising in-line and also side-by-side in a liquid pool. They investigated the impact of bubble radius on the bubble dynamics and coalescence, discovering that the coalesced bubble rises with volume and velocity oscillations and that raising the bubble radius increases the time of the volume oscillations. In their numerical analysis, Tripathi et al. (28) looked at six distinct $Ga - Bo$ sets, including $(Ga, Bo) = (22.4, 4), (32, 4), (60, 4), (25, 1), (100, 2)$, and $(25, 4)$. They explored how Ga, Bo, and initial separation affected the dynamics of the bubbles and demonstrated that there is a mirror symmetry in the bubble trajectories even in a high-inertia environment (high Ga). Zhang et al. (64) investigated the coalescence and interaction of two bubbles rising in-line in viscous liquids using axisymmetric simulations. They investigated the influence of surrounding fluid viscosity on coalescence and proposed a bifurcation diagram depicting four distinct coalescence regimes. Cao and Macián-Juan (65) studied the effects of initial separation on the dynamics of two in-line bubbles rising in quiescent liquid using a numerical simulation. They discovered that at a modest initial separation, the trailing bubble collides with the leading bubble, resulting in a central breakup of the trailing bubble caused by elongation. They also demonstrated that at greater initial separation, the trailing bubble experiences lateral motion due to the wake of the leading bubble. Kumar et al. (66) also numerically investigated the coalescence and interaction of two in-line bubbles rising in a quiescent liquid. They explored the impacts of initial separation and the ratio of the bubbles radius on coalescence, discovering that increasing the initial separation lengthens the coalescence duration.

While many materials found in both nature and industry are non-Newtonian fluids, such as blood, polymers, and carboxymethyl cellulose (CMC) solutions, a large portion of studies in the literature concentrated on the bubble rising in Newtonian fluids. In contrast to Newtonian fluids, non-Newtonian fluids exhibit more complex bubble rising dynamics and interactions, and there is little relevant research available. By conducting experiments on a pair of bubbles rising in Xanthan gum with flow indices (n) of 0.85 and 0.55, Rodrigo Vélez-Cordero et al. (67) were able to demonstrate that as the flow index decreases, the wake behind the leading bubble draws the trailing bubble more quickly. Using the VOF approach coupled with

the Continuous Surface Force (CSF) method, Fan and Yin (*68*) carried out a numerical simulation to examine the interaction of two bubbles rising in shear-thinning fluids, provided by the power-law model. They took into account various bubble arrangements (side-by-side and oblique) and initial separations, demonstrating that for side-by-side bubbles, the repulsive effect decreases with the initial separation and that for two oblique bubbles, there may be an equilibrium angle at which the repulsive and attractive interactions are balanced. Tariqul Islam et al. (*69*) numerically examined the side-by-side and oblique configurations for a pair of bubbles rising in shear-thinning fluids described by the power-law. They noted that as the flow index is reduced, the bubbles' shape shifts from spherical to irregular, and there is also significant oscillation between the bubbles. Liu et al. (*70*) studied the coalescence and interaction of several horizontal bubbles rising in shear-thinning fluids with various arrangements and initial separations, determining the critical bubble separation for coalescence under various situations using VOF simulations. Sun et al. (*71*) investigated the dynamical behavior of multiple bubbles rising in shear-thinning fluids with equilateral triangle arrangements at Reynolds numbers ranging from 5 to 300, using the correlation of the interaction coefficient among the bubbles as the ratio of the bubble drag coefficient for multiple systems and a single bubble rising under the same conditions. They (*72*) also employed the VOF approach to model three horizontal bubbles of varying diameters in shear-thinning fluids, proposing a correlation for the bubbles' drag coefficient.

1.2 Thesis goals and structure

The title of the research project is "Numerical investigation of a single bubble and a pair of bubbles rising in Newtonian and non-Newtonian fluids with interfacial passive scalar transfer". Its primary aims are to examine the dynamic behavior of the bubble/bubbles and the heat/mass transfer from the bubble/bubbles to the surrounding fluid.

To achieve this, the study investigates the influence of several factors on the dynamics and heat/mass transfer across the bubble interface in two primary configurations: a single bubble and a pair of bubbles rising in Newtonian or non-Newtonian

fluids. The factors under consideration include:

1. Galilei number ($Ga = \frac{\rho g^{1/2} R^{3/2}}{\mu_A}$): It is the ratio of the gravitational force to the viscous force. Greater Ga indicates that the bubble is subjected to more inertial force. It can be changed by adjusting the bubble radius or the viscosity of the surrounding fluid.

2. Bond number ($Bo = \frac{\rho_A g R^2}{\sigma}$): This evaluates the influence of surface tension and gravity on the movement of the liquid front and describes the shape of the bubble as it moves through the fluid. A high value of Bo implies that surface tension has little effect on the system, whereas a low value (usually less than one) suggests that surface tension is dominant (73). The bubble radius or surface tension can be modified to alter this parameter.

3. Flow index (n): It is often used to describe the rheological characteristics of the fluids and is defined as the ratio of shear stress to shear rate, measuring the non-Newtonian flow characteristics of a fluid. When n equals one, the fluid is Newtonian. If n exceeds one, the fluid is classified as dilatant or shear-thickening (the apparent viscosity increases as the shear rate increases). If n is between zero and one, the fluid is Pseudoplastic and shear-thinning (the apparent viscosity decreases as the shear rate increases) (74).

4. Inelastic time constant (λ): it is the relaxation time constant of the Carreau rheological model (75).

5. Peclet number (Pe): It is defined as the ratio of the rate of advection of a physical quantity caused by flow to the rate of diffusion of the same quantity caused by an adequate gradient, reflecting the relative importance of advection against diffusion. A high number of Pe denotes an advectively dominated distribution, while a low number of Pe denotes a diffuse flow (76).

The study involved a comprehensive investigation of the impact of various parameters on bubble dynamics and heat/mass transfer in different fluid configurations. The attained results contribute to a deeper understanding of the fundamental physics of bubbly flows and the effect of rheological properties on such flows. The

numerical models and simulation techniques developed in this study provide a basis for future research in the field of multiphase flow and heat transfer. The findings of this study also have potential applications in various fields such as chemical engineering, biotechnology, and environmental engineering.

The thesis is arranged in the following chapters:

Chapter 1 is dedicated to an introduction to the thesis, outlining its aims and objectives, and providing a list of the main scientific contributions.

Chapter 2 provides a detailed description of the numerical and mathematical models used in the research project. It explains the governing equations of fluid dynamics and heat/mass transfer, as well as the numerical methods used to solve them. The chapter also outlines the Carreau model used to describe the non-Newtonian behavior of the fluids and the phase-field model used to simulate the dynamics of the bubble/bubbles. Furthermore, the chapter describes the validation of the numerical models against experimental and analytical results to ensure the accuracy and reliability of the simulations.

Chapter 3 examines the scalar transfer rate from a single bubble to a fluid that is quiescent and exhibits Carreau rheological behavior, with Galilei and Bond numbers of 30 and 2, respectively, and a non-dimensional inelastic time constant of 6. The bubble dynamics regime remains in steady and oscillatory regions under these circumstances. The mass transfer equation of a scalar is coupled to the Navier-Stokes equations, which are numerically solved in a non-stationary three-dimensional domain, and the impact of the Peclet number and flow index of the quiescent fluid on the Sherwood number is investigated.

Chapter 4 presents a numerical study that investigated the motion, interaction, and passive scalar transport of a pair of bubbles rising in Newtonian and shear-thinning fluids. The study aimed to better understand the complex mechanisms underlying heat and mass transfer in multiphase systems by evaluating the impact of various parameters, such as the Galilei and Bond numbers, the radius ratio of the bubble pair, and the flow index and inelastic time constant of the fluid. The results provided valuable insights into the behavior of bubbles

in industrial processes, which can help in the development of more efficient and cost-effective methods for mass transfer. Overall, the study demonstrated the importance of considering the dynamic behavior of multiple bubbles when analyzing heat and mass transfer in real-world industrial scenarios.

Chapter 5 concludes the thesis by summarizing the research objectives, the methodologies used to achieve them, and the major findings of the study. It also discusses potential future directions for this research, including the impact of different factors on the dynamics and heat/mass transfer in various fluid types and configurations.

1.3 Related Contributions

Throughout the course of this research, the following significant contributions were made:

- **Journal articles**
  - Kazemi, Koorosh; Vernet, Anton; Grau, Francesc X.; Cito, Salvatore; Fabregat, Alexandre. (2022) "Passive scalar transfer rate at bubble interface in Carreau liquid in a transition regime", Int. Journal of Multiphase Flow, 150, DOI: https://doi.org/10.1016/j.ijmultiphaseflow.2022.104000.
- **Conference contributions**
  - Kazemi, Koorosh; Vernet, Anton; Grau, Francesc X.; Cito, Salvatore; Fabregat, Alexandre. (2021) "Study of bubble rising dynamics and interfacial scalar transport in Carreau-Yasuda quiescent fluid model", Annual European Rheology Conference, Nantes, France.
  - Kazemi, Koorosh; Vernet, Anton; Cito, Salvatore; Fabregat, Alexandre. (2020) "Numerical simulation of interfacial transport phenomena of bubbles immersed on non-Newtonian fluids", XIV International Conference on Rheology and Fluid Mechanics, Rome, Italy.
- **Presentations**

- Kazemi, Koorosh. (2022) "Study of bubble rising dynamics and interfacial scalar transport", University of Bremen, Bremen, Germany.
- Kazemi, Koorosh; Vernet, Anton; Grau, Francesc X.; Cito, Salvatore; Fabregat, Alexandre. (2022) "Passive scalar transfer rate at bubble(s) interface in a Carreau liquid", 17th Doctoral Day in Nanoscience, Materials and Chemical Engineering, Universitat Rovira Virgili (URV), Spain.
- Kazemi, Koorosh. (2021) "A single bubble rising in a non-Newtonian fluid with mass transfer across the bubble interface", Ecommfit, URV, Tarragona, Spain.
- Kazemi, Koorosh. (2021) "Introduction to multi-phase flows", European night, Tarragona, Spain.

UNIVERSITAT ROVIRA I VIRGILI,
NUMERICAL INVESTIGATION OF A SINGLE BUBBLE AND A PAIR OF BUBBLES RISING IN NEWTONIAN AND NON NEWTONIAN FLUIDS WITH INTERFACIAL PASSIVE SCALAR TRANSFER
Koorosh Kazemi

Chapter 2

Numerical study

The present research project aimed to investigate the dynamics of bubbles rising in Newtonian or non-Newtonian fluids and the accompanying heat/mass transfer across the bubble-fluid interface through three-dimensional numerical simulations. To accurately simulate bubble dynamics, the mass continuity equation and the momentum or Navier-Stokes equations (NSE) must be numerically solved, and the advection-diffusion equation must be employed to model heat and mass transport. Additionally, the rheology of non-Newtonian fluids is described using the Carreau model. The simulation results are used to gain insights into the dynamic behavior of single and multiple bubbles and the underlying heat/mass transfer mechanisms, while also examining the impact of various factors on the system's behavior. The simulation results are validated against experimental data and established numerical benchmarks from previous studies to ensure the accuracy and reliability of the code.

2.1 Formulations

A Cartesian system (x, y, z) is used to represent the motion of a gas bubble (fluid B) of initial radius R rising due to buoyancy inside a cubic box of length L filled with an incompressible Newtonian or non-Newtonian fluid A.

To determine the flow characteristics, mass and momentum (NSE) conservation equations for incompressible binary and immiscible flows must be solved, as given by (77):

$$\nabla \cdot \tilde{\mathbf{u}} = 0 \tag{2.1}$$

$$\rho\left[\frac{\partial \tilde{\mathbf{u}}}{\partial \tilde{t}} + \tilde{\mathbf{u}} \cdot \nabla \tilde{\mathbf{u}}\right] = -\nabla \tilde{p} + \nabla \cdot (\mu \nabla \tilde{\mathbf{u}}) + \delta \sigma \tilde{\kappa} \vec{\mathbf{n}} - \rho g \jmath \tag{2.2}$$

where $\tilde{\mathbf{u}}(\tilde{u}, \tilde{v}, \tilde{w})$ is the velocity vector with components $\tilde{u}$, $\tilde{v}$ and $\tilde{w}$ aligned in the $\tilde{x}$, $\tilde{y}$ and $\tilde{z}$ directions, respectively. ρ, $\tilde{t}$, $\tilde{p}$, g, and μ represent density, time, pressure, gravitational acceleration, and dynamic viscosity, respectively. The concentrated nature of the surface tension term at the interface is expressed by the Dirac delta function, δ, and the constant surface tension coefficient is denoted by the symbol σ. $\vec{\mathbf{n}}$ represents the outward-pointing unit normal to the fluid "A" at the interface, $\tilde{\kappa}\vec{\mathbf{n}}$ denotes interfacial curvature and $\jmath$ is the unit vector in the vertical direction (along gravity- negative y direction). The tilde indicates dimensional variables. Here, the surface tension force is considered as a body force term using the continuum method suggested in (*78*).

For two-phase flows, the density and viscosity can be written as:

$$\rho \equiv \rho(f) = \rho_A f + \rho_B (1 - f) \tag{2.3}$$

$$\mu \equiv \mu(f) = \mu_A f + \mu_B (1 - f). \tag{2.4}$$

where A denotes the phase of ambient fluid with the properties of density ρ_A and dynamic viscosity μ_A, and B denotes the phase of bubble fluid with the properties of density ρ_B and dynamic viscosity μ_B. The densities of both phases are assumed to be constant. The gas phase is considered to be Newtonian with a constant dynamic viscosity whereas the liquid phase can be Newtonian or non-Newtonian whose rheology is described by the Carreau model. The interface between the two phases is monitored using the volume fraction of fluid f, which is bounded between 0 (fluid B) and 1 (fluid A).

2.2 Non-dimensionalization

The governing equations are non-dimensionalized using the following scaling for length, velocity, and pressure:

$$l^* = R \tag{2.5}$$

$$u^* = \sqrt{gR} \tag{2.6}$$

$$p^* = \rho_A (u^*)^2 \tag{2.7}$$

where R represents the radius of the initially spherical bubble. In this case, the set of non-dimensional parameters yield:

$$Ga = \frac{\rho_A u^* l^*}{\mu_A} = \frac{g^{1/2} R^{3/2}}{\nu_A} \tag{2.8}$$

$$Bo = \frac{\rho_A u^{*2} l^*}{\sigma} = \frac{\rho_A g R^2}{\sigma} \tag{2.9}$$

where Ga and Bo are Galilei and Bond numbers, respectively.

The non-dimensional governing NSE can be written as:

$$\frac{D\mathbf{u}}{Dt} = \frac{1}{\alpha}\left[-\nabla p + \frac{1}{Ga}\nabla \cdot (\beta \nabla \mathbf{u}) + \frac{1}{Bo}\delta\kappa\vec{\mathbf{n}}\right] - \jmath \tag{2.10}$$

where $\alpha = \frac{\rho}{\rho_A} = f + \rho^\star(1-f)$, $\beta = \frac{\mu}{\mu_A} = f + \mu^\star(1-f)$ and the density and dynamic viscosity ratios are defined as $\rho^\star = \frac{\rho_B}{\rho_A}$ and $\mu^\star = \frac{\mu_B}{\mu_A}$, respectively.

2.3 Non-Newtonian model

The viscosity of a non-Newtonian surrounding fluid (fluid A) is proportional to the shear rate. To simulate the viscosity of the surrounding fluid, the Carreau rheological model is employed. Although the Carreau model is most commonly used for shear-thinning fluids, it has also been applied to shear-thickening fluids (79–81). The model can be expressed as follows (75):

$$\mu_A = \mu_A^0 \eta = \mu_A^0 \left[1 + (\lambda\Pi)^2\right]^{(n-1)/2}. \tag{2.11}$$

where μ_A^0 represents the dynamic viscosity of fluid A corresponding to the zero shear rates. λ and n are the inelastic time constant and flow index, respectively. $\Pi =$

$(E_{ij}E_{ij})^{0.5}$ is the second invariant of the strain rate tensor, wherein $E_{ij} = \frac{1}{2}(\frac{\partial u_i}{\partial x_j} + \frac{\partial u_j}{\partial x_i})$. Unless otherwise specified, the value of λ remains constant at 6 throughout this study.

Applying the predetermined scaling, the non-dimensional NSE for the bubble rising in Newtonian/non-Newtonian fluids can be expressed as follows:

$$\frac{D\mathbf{u}}{Dt} = \frac{1}{\alpha}\left[-\nabla p + \frac{1}{Ga^0}\nabla\cdot(\beta\nabla\mathbf{u}) + \frac{1}{Bo}\delta\kappa\vec{\mathbf{n}}\right] - \jmath \tag{2.12}$$

where the $Ga^0 = \frac{\rho_A g^{1/2} R^{3/2}}{\mu_A^0}$, $\beta = \frac{\mu}{\mu_A^0}$ and $\mu^\star = \frac{\mu_B}{\mu_A^0}$. In this study, the density ratio, $\rho^\star$, and the initial viscosity ratio, $\mu^\star$, are set to 0.001 and 0.01, respectively.

2.4 Passive scalar transport

The general equation that describes the transport of a passive scalar ϕ can be written as:

$$\frac{\partial\widetilde{\phi}}{\partial\tilde{t}} + \nabla\cdot\tilde{\mathbf{u}}\widetilde{\phi} = \nabla\cdot\left(\mathcal{D}\nabla\widetilde{\phi}\right) \tag{2.13}$$

where $\mathcal{D}$ is the passive scalar diffusion coefficient and varies among different phases, indicating distinct values for each phase.

The equation above can be non-dimensionalized using $\phi = (\widetilde{\phi} - \widetilde{\phi}_\infty)/(\widetilde{\phi}_0 - \widetilde{\phi}_\infty)$ where $\widetilde{\phi}_0$ and $\widetilde{\phi}_\infty$ are the initial scalar within the bubble and far-field values, respectively. Thus, the non-dimensional equation reads:

$$\frac{\partial\phi}{\partial t} + \nabla\cdot\mathbf{u}\phi = \frac{1}{Pe}\nabla^2\phi \tag{2.14}$$

where $Pe = \frac{u^* l^*}{\mathcal{D}}$ is Peclet number. Initial value of ϕ inside the bubble is 1 and everywhere else is zero and the expression for the Peclet number in a two-phase flow can be formulated as follows:

$$Pe \equiv Pe(f) = Pe_A f + Pe_B(1-f) \tag{2.15}$$

The density flux of the scalar $\widetilde{\phi}$ can be written as:

$$q''_\phi = -\mathcal{D}\nabla\widetilde{\phi} \tag{2.16}$$

where $\mathcal{D}$ is the scalar diffusion coefficient.

This quantity can also be expressed using Newton's Law of Cooling as:

$$q''_\phi = h_\phi \left(\widetilde{\phi}_s - \widetilde{\phi}_\infty\right). \tag{2.17}$$

where h_ϕ is the local convective transport coefficient, $\widetilde{\phi}_s$ is the local value of $\widetilde{\phi}$ at the bubble surface and $\widetilde{\phi}_\infty$ is the environment value of the scalar (assumed constant).

The amount of $\widetilde{\phi}$ transferred from the bubble to the environment through the interface $\widetilde{S}(\tilde{t})$ can be written as:

$$\widetilde{q_\phi} = \frac{\partial}{\partial\tilde{t}}\int_{\widetilde{\mathcal{V}}}\widetilde{\phi}d\widetilde{\mathcal{V}} = \int_{\widetilde{S}} -\mathcal{D}\nabla\widetilde{\phi}\cdot\vec{\mathbf{n}}d\widetilde{S} = \int_{\widetilde{S}} h_\phi\left(\widetilde{\phi}_s - \widetilde{\phi}_\infty\right)d\widetilde{S} \tag{2.18}$$

where $\widetilde{\mathcal{V}}(\tilde{t})$ is the bubble volume (assumed constant). Using the Gauss Theorem, the non-dimensional form of the Eq. (2.18) can be written as:

$$\frac{\widetilde{q_\phi}}{l^*\phi^*\mathcal{D}} = q_\phi = Pe\frac{\partial}{\partial t}\int_{\mathcal{V}}\phi d\mathcal{V} = -\int_{\mathcal{V}}\nabla^2\phi d\mathcal{V} = \int_S \frac{h_\phi l^*}{\mathcal{D}}\phi_s dS \tag{2.19}$$

Using $\langle\rangle$ to denote interface averaged quantities, $\langle h_\phi\rangle$ is the surface-averaged convective transport coefficient and $\langle\phi_s\rangle$ is the surface-averaged value of ϕ, and Eq. (2.19) can be written as:

$$\langle Sh\rangle = \frac{q_\phi}{\langle\phi_s\rangle} = -\frac{\int_V\nabla^2\phi dV}{\langle\phi_s\rangle} = \frac{l^*\langle h_\phi\rangle}{\mathcal{D}} \tag{2.20}$$

And therefore,

$$q_\phi = \langle Sh\rangle\langle\phi_s\rangle \tag{2.21}$$

where $\langle Sh\rangle$ is the surface-averaged Sherwood number.

2.5 Numerical method

NSE and advection-diffusion are solved numerically using *Basilisk* (82), a Volume-of-Fluid (VOF) open-source solver widely used to numerically investigate multi-phase flows (83, 84). In order to quantitatively examine the evolution of complex surfaces that may eventually break up and/or coalesce under high density and viscosity ratios, *Basilisk* adopts a surface-tracking approach. Besides this, *Basilisk* Using balanced-force continuum surface force formulation to calculate the surface tension force, *Basilisk* ensures the minimizing of parasitic currents at the interface by computing the surface tension force using a balanced-force continuum surface force formulation (85). Additionally, by dynamically increasing the local mesh resolution in accordance with user-specified requirements, numerical efficiency is ensured.

In the current application, the oct-tree-based mesh refinement technique controls the error on local values of velocity magnitude and passive scalar concentration, as well as the bubble interface position. In order to improve the accuracy and extend the capabilities of the simulation code, several new features were added to *Basilisk*:

1. The Carreau model to compute the viscosity of the surrounding fluid.

2. Advection-diffusion equation to model heat/mass transfer from the bubble to the surrounding fluid, and compute the transfer rate directly without any further post-processing.

3. The procedure of calculating q_ϕ by using the volume integral inside the bubble as well as the surface-averaged value of the scalar, $\langle \phi_s \rangle$, which is necessary to calculate $\langle Sh \rangle$.

4. A finite difference approach for calculating the surface-averaged Sherwood number, $\langle Sh \rangle$.

5. A method for converting data into the VTK files during parallel processing to facilitate data visualization and analysis.

These additions were implemented and tested to enhance the accuracy and efficiency of the simulations and improve the overall reliability of the code.

2.6 Grid study and validation

To ensure the accuracy and reliability of the simulations and outcomes, it is crucial to study the grid resolution and validate the results. These validation tests demonstrate that the numerical models and simulation code are accurate and reliable for simulating bubble dynamics and heat/mass transfer in Newtonian and non-Newtonian fluids.

The grid resolution determines the accuracy and reliability of the numerical solutions, and it can significantly impact the results. Therefore, it is essential to conduct grid sensitivity studies to ensure that the grid resolution is adequate for the intended purpose and to evaluate the impact of grid resolution on the simulation results. The ideal domain size was determined by comparing various tank volumes in order to ensure that the effects of the walls, which were modeled as no-slip surfaces, are negligible. Consequently, a cubic box with a non-dimensional length of 120 was chosen. The background mesh resolution level was set to refinement level 2^5 under the octtree mesh hierarchy utilized by the solver, which equates to a mesh resolution of 32 cells in each direction. The mesh refinement strategy resulted in an increase in the total number of cells of up to 10^7 cells.

Mesh-independence results for a single bubble rising in a shear-thinning fluid ($n = 0.3$) with $Pe = 1000$ are shown in figure 2.1 using the temporal evolution of the non-dimensional density flux q_ϕ and local Reynolds number $Re_l = \frac{\rho_A u_b d}{\mu_A^0}$ where u_b is the bubble rising velocity and d is initial diameter of the bubble. The differences between the three distinct mesh levels (m = 10, 11, and 12) imply that $m = 11$ produces adequate grid resolutions. Mesh level, m, represents the level of mesh refinement based on the various parameters applied to the initial mesh resolution (here, local values of velocity magnitude, the passive scalar concentration, and bubble interface position).

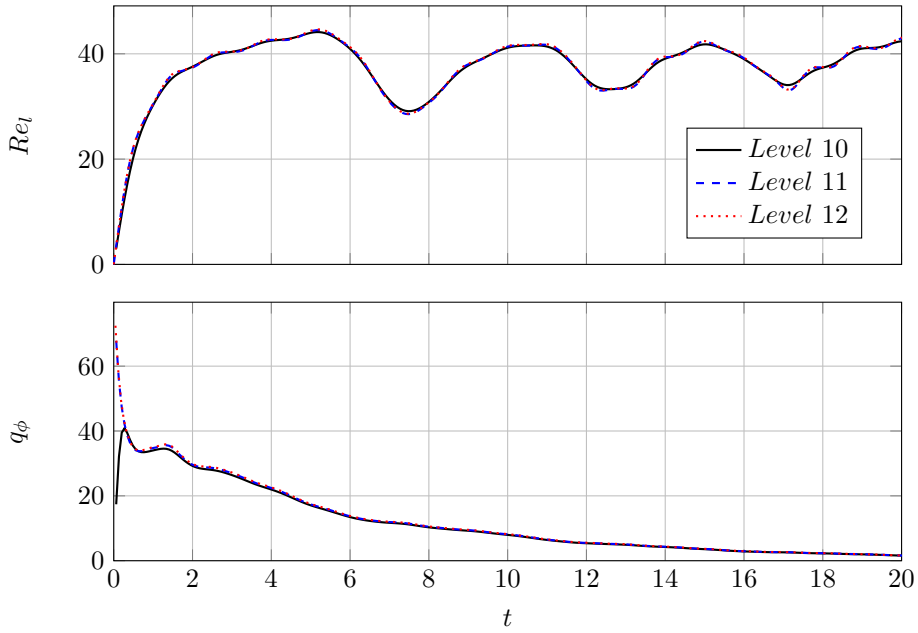

FIGURE 2.1: Evolution of local Reynolds number (top) and non-dimensional density flux (bottom) for a single bubble rising with different mesh levels, $n = 0.3$ and $Pe = 1000$.

Furthermore, the fluctuation in bubble volume is used to define the mass conservation error:

$$\mathcal{E} = 100\frac{\mathcal{V}(t) - \mathcal{V}_0}{\mathcal{V}_0} \tag{2.22}$$

where $\mathcal{V}_0$ is the initial volume of the bubble and $\mathcal{V}(t) = (1 - f)\int_V dV(t)$. Figure 2.2 shows that the error is under 0.05 % for different ambient fluids. It should be noted that the minor changes shown in figure 2.2 are principally attributable to the use of adaptive mesh refinement, which requires a different mesh resolution for each scenario.

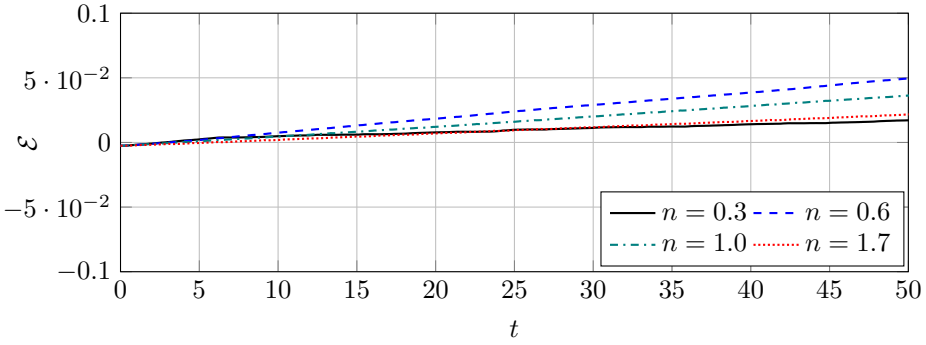

FIGURE 2.2: The evolution of the mass conservation error for different ambient fluids.

The methodology is also validated for the case of two in-line bubbles rising in

a quiescent liquid with an initial separation of $S = 3R$. The current findings are compared to experiments and numerical simulations previously documented in the literature. The Galilei, Bond, and density and dynamic viscosity ratios are identical to those used in the experiments by Brereton and Korotney (*86*) who used $Ga = 23.78$, $Bo = 4$, and $\rho^\star = \mu^\star = 0.01$. Figure 2.3 compares the coalescence process of the bubbles to the experimental observations of Brereton and Korotney (*86*) and numerical findings of Chakraborty et al. (*87*).

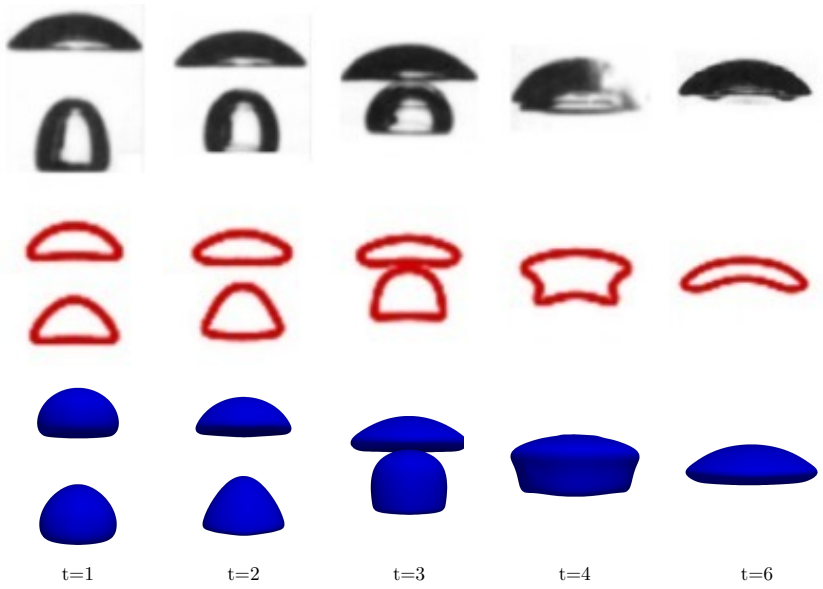

FIGURE 2.3: The evolution of the bubble shapes and the coalescence process. Top: Experimental observations of Brereton and Korotney (*86*); Middle: Numerical results of Chakraborty et al. (*87*); Bottom: Present work.

Although numerical and experimental results agree fairly well, the lag existing between the release times of two bubbles in the experiments and slight deviations from the spherical shape result in distinct wake characteristics. This is in contrast to the numerical simulations, in which the bubbles are perfectly spherical and released simultaneously in a completely quiescent ambient fluid.

Our results are also compared with those of Chakraborty et al. (*87*) who used coupled level-set and volume of fluid (CLSVOF) to simulate the same case in a two-dimensional domain. Using the instantaneous Reynolds number Re for the leading (LB) and trailing (TB) bubbles (based on the initial diameter and instantaneous rising velocity, $Re = \frac{\rho_A u_b R}{\mu_A^0}$), Figure 2.4 provides the comparison between the present

findings and numerical results of Chakraborty et al. (*87*) (shown with the legend of NRCH) methodologies.

Despite the differences in the two numerical approaches, the results show that both simulations predict a similar evolution of the Re number up to the quasi-terminal conditions when this parameter plateaus at $Re = 49.1$, a value very close to the experimental value of $Re = 50$ obtained from the bubble diagram of Bhaga and Weber (*88*) and Clift et al. (*89*).

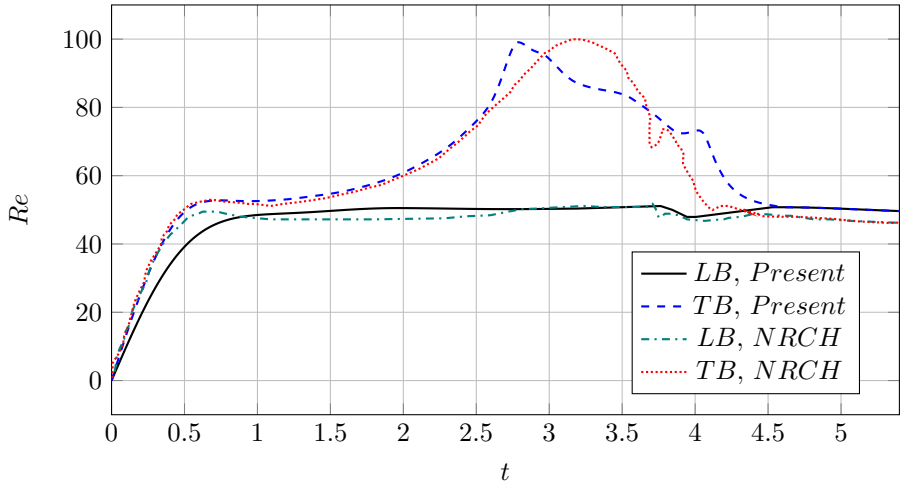

FIGURE 2.4: Evolution of the instantaneous Re for the trailing and leading bubbles; Present work and numerical results of Chakraborty et al. (*87*).

Chapter 3

A single bubble rising

This chapter focuses on the numerical simulation of gas-liquid heat/mass transfer from a single bubble to a fluid with Carreau viscosity, which can be either Newtonian, shear-thinning, or shear-thickening. The simulations are carried out under a fixed set of (Ga,Bo) conditions, and the effects of the Peclet number and flow index on the Sherwood number and bubble dynamics are investigated.

3.1 Physical model

A schematic of the numerical domain with a cubic box filled with Newtonian or non-Newtonian fluids and a length of 120 is shown in figure 3.1. The spherical bubble with a radius of 0.5 is first released at $(x_0, y_0, z_0) = (0, 15, 0)$ with zero velocity. Due to the huge box dimensions, the impacts of the walls on the bubble dynamics are kept to a minimum. Note that all the parameters are non-dimensional.

The distinct regimes of the air-water system are represented in a $Ga - Bo$ phase plot in figure 3.2, using the interface topology. The five regimes are axisymmetric, oscillatory (zigzag or spiral), skirted, peripheral breakup, and central breakup regions ((*90*)), according to the plot. It is reasonable that the bubble maintains its integrity in regime I because of the high surface tension and low gravity. A typical example of a constant ellipsoidal shape is depicted in that area of the figure taking on a terminal velocity going straight upwards. In this regime, the bubble is axisymmetric. A thin skirt that follows the main body of the bubble and an axisymmetric cap are the two distinguishing characteristics of the bubble in regime II. The skirt has minor

deviations from axisymmetry in the form of waves. Bubbles in this regime also migrate in a vertical line upwards, almost reaching a terminal velocity after the initial transients.

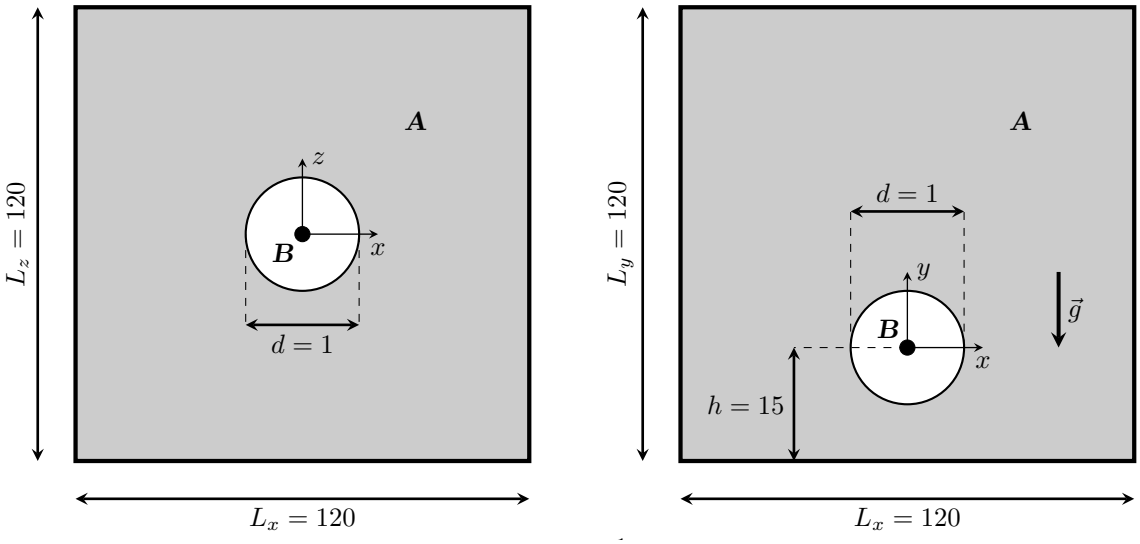

FIGURE 3.1: Top and side views of the computational domain (not to scale) showing the flow configuration with an initially spherical bubble of fluid B and non-dimensional diameter $d = 1$ placed at $y = h = 15$ in a $L_x = L_y = L_z = 120$ cubical box filled with fluid A.

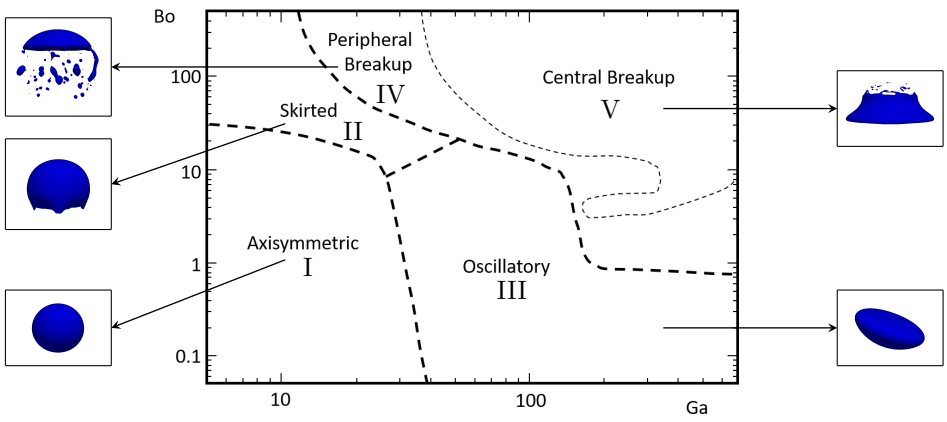

FIGURE 3.2: $Ga - Bo$ phase plot of an air bubble rising in water. This figure is taken from Tripathi et al. (*90*).

Surface tension and inertial forces are both considerable and of the same order in regime III. Bubbles deviate significantly from axisymmetry in this region early on, rising in a zigzag or spiral pattern. Bubbles remain integral, although their shapes alter throughout time. In regimes IV and V, the bubble usually breaks up due to greater gravity and very weak surface tension. Regime IV is a limited zone that has a moderate value of the product $Ga - Bo$. The bubble in this regime breaks into a

big axisymmetric spherical cap and several small satellite bubbles in the cap's wake. Ultimately, high inertial and low surface tension forces are acting on the bubbles in regime V. A profoundly different types of dynamics can be observed here. A dimple creation in the bottom center causes a shift in topology, as seen in the figure, to a doughnut-like or toroidal shape. The shift in topology may be accompanied by the ejection of tiny satellite bubbles toward the edge of regime IV. Further increases in Ga and Bo in this area result in a fully axisymmetric alteration in the topology of the entire bubble. This new shape is temporary, in contrast to the other areas. It gradually develops into several bubble fragments and loses its symmetry.

To investigate the effect of the rheology on the bubble dynamics, the Bond and Galilei numbers are set to 2 and 30, respectively, located near the border of regimes I and III. Therefore, it is expected to see deviations from the axisymmetric trajectory displayed by the air bubble when released in water, which is a Newtonian fluid. The values of λ and n for the shear-thinning fluids used in this chapter are taken from the experiments of Zhang et al. (*91*) and also the numerical simulation of Premlata et al. (*92*). Additionally, a value of flow index for shear-thickening fluids is used to study this case as well.

3.2 Results

In a large tank, a single bubble rising in Newtonian, shear-thinning, and shear-thickening fluids is simulated, and the impact of the rheological properties on the bubble dynamics, as well as the effects of the Peclet number and rheological properties on heat/mass transfer across the bubble interface, are explored.

3.2.1 Effects of the rheological properties on the dynamics of the bubble

The rheological characteristics, such as the flow index, have a significant impact on the bubble rising dynamics. Defining effective Galilei number, $Ga_{eff} = \frac{\rho_A u_b L}{\mu_A}$ and effective Bond number,$Bo_{eff} = \frac{\rho_A {u_b}^2 L}{\sigma}$, where u_b is the bubble rising velocity and characteristic length scale is $L = V/A$, the effects of n on $Ga - Bo$ phase plot can be seen in figure 3.3. As can be observed, the bubble dynamics behavior switches to the

axisymmetric area for the shear-thickening case, whereas it shifts to the oscillatory region for the shear-thinning cases.

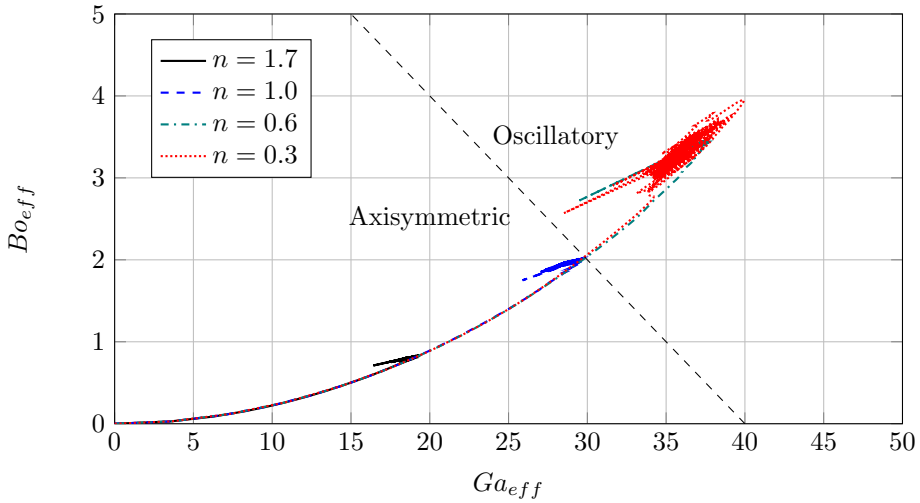

FIGURE 3.3: History of $Ga - Bo$ phase plot for different flow indexes.

The impacts of the flow index on the dynamics of the single bubble as it rises, including bubble trajectory, rising velocity, bubble topology, and the viscosity field are investigated in this section. Four different flow indexes, n, are considered: 0.3 and 0.6 for the shear-thinning fluids, 1 for the Newtonian fluid, and 1.7 for the shear-thickening fluid.

Bubble trajectory

The position of the bubble's center of mass, originally placed at ($x_0 = 0, y_0 = 15, z_0 = 0$), versus time for various scenarios is represented in figure 3.4. The findings show that the bubble rises vertically when $n = 1.0$ as well as when $n = 0.6$ and $= 1.7$. On the contrary, the most intense shear-thinning scenario, with $n = 0.3$, exhibits an oscillatory pattern with a zigzag motion. Consequently, this case has more dramatic bubble excursions and lateral departures. This implies that the bubble dynamics may finally mirror those displayed by a Newtonian ambient fluid at higher Galilei numbers when the background flow behaves as a shear-thinning fluid. Furthermore, by zooming into figure 3.4, it can be seen that for $n = 0.3$, the bubble rises more quickly compared to the case of $n = 0.6$ until $t = 0.5$ when the oscillatory behavior of the bubble begins to expand.

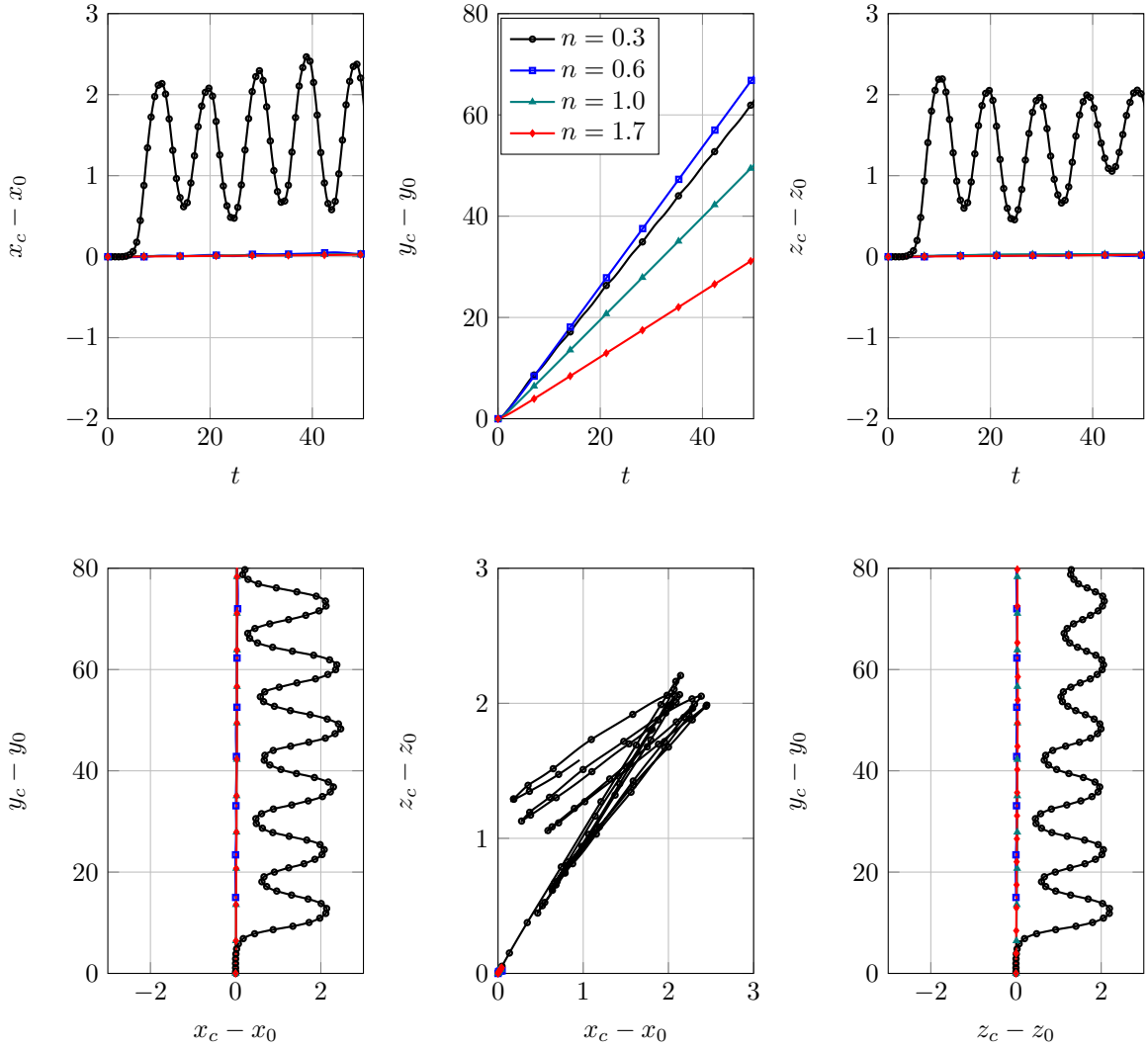

FIGURE 3.4: Bubble trajectory for different flow indexes; top: coordinates of the bubble versus time, and bottom: 2D position of the bubble on each slice.

Interface topology

Figure 3.5 displays $x = 0$ slices of the viscosity field at two distinct times for different flow indexes, as well as the shape of the bubble (in white). Shear-thinning ambient fluids cause large deviations from the spherical shape of the bubble, which tends to flatten as it rises in comparison to $n = 1$. Shear-thickening ambient fluid, on the other hand, typically prevents the bubble from deforming significantly. The oscillatory behavior of the bubble in figure 3.4 results in oscillatory changes in the bubble topology when growing in a shear-thinning fluid. Changes in the bubble shape are minor for $n = 0.6, 1.0, and 1.7$ compared to $n = 0.3$. Figure 3.6 which presents the

temporal history of the rising velocity magnitude, $\|V\|$, of the bubble (top) and the normalized bubble interface area (bottom), makes this observation quite evident.

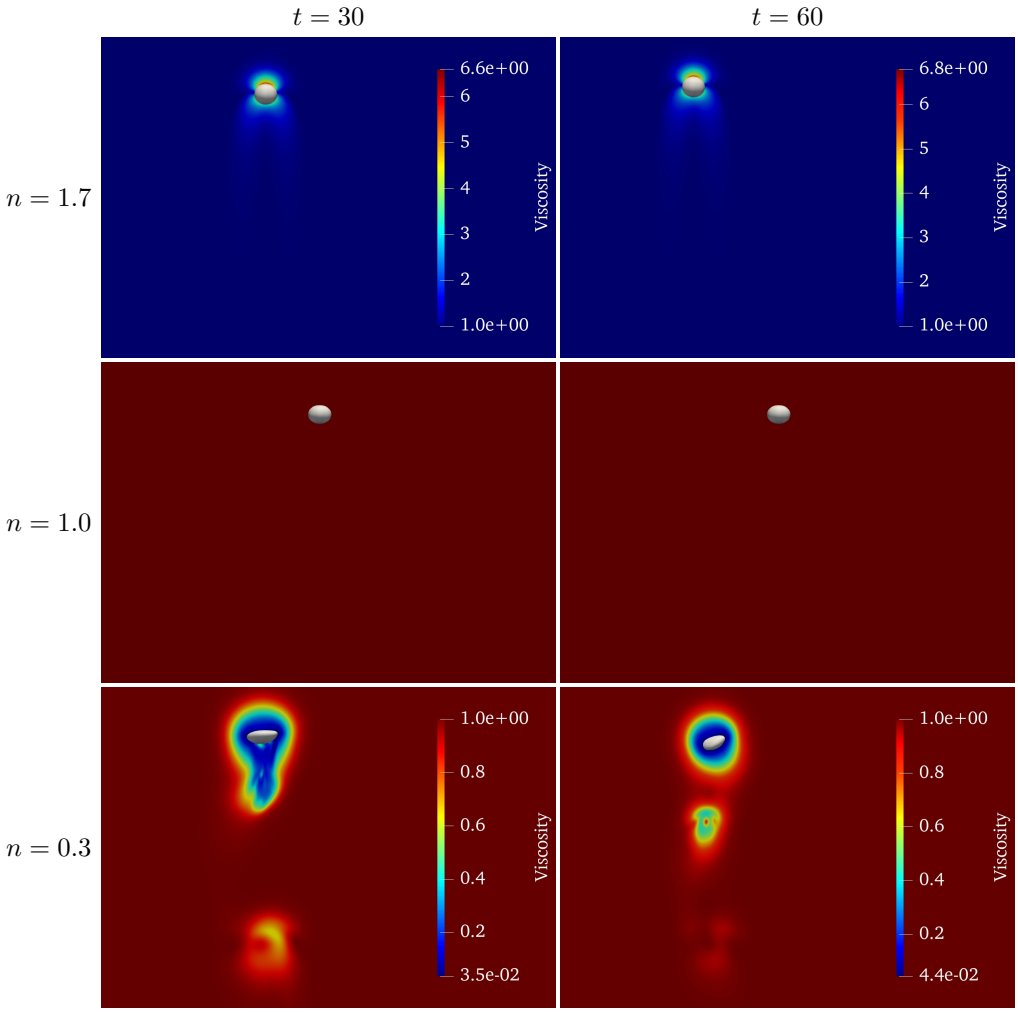

FIGURE 3.5: Viscosity profiles around the bubble for different flow indexes at different times in $y - z$ plane.

Shear-thickening ambient fluid results in a substantially lower rising velocity than the Newtonian case because of locally elevated viscous friction. Reduced viscosity near the interface, on the other hand, causes quicker rising bubbles for both $n = 0.6$ and $n = 0.3$. The bubble, however, displays an oscillating behavior in the latter case, with a vertical rising velocity mean value that is very similar to the constant value displayed by the $n = 0.6$ case.

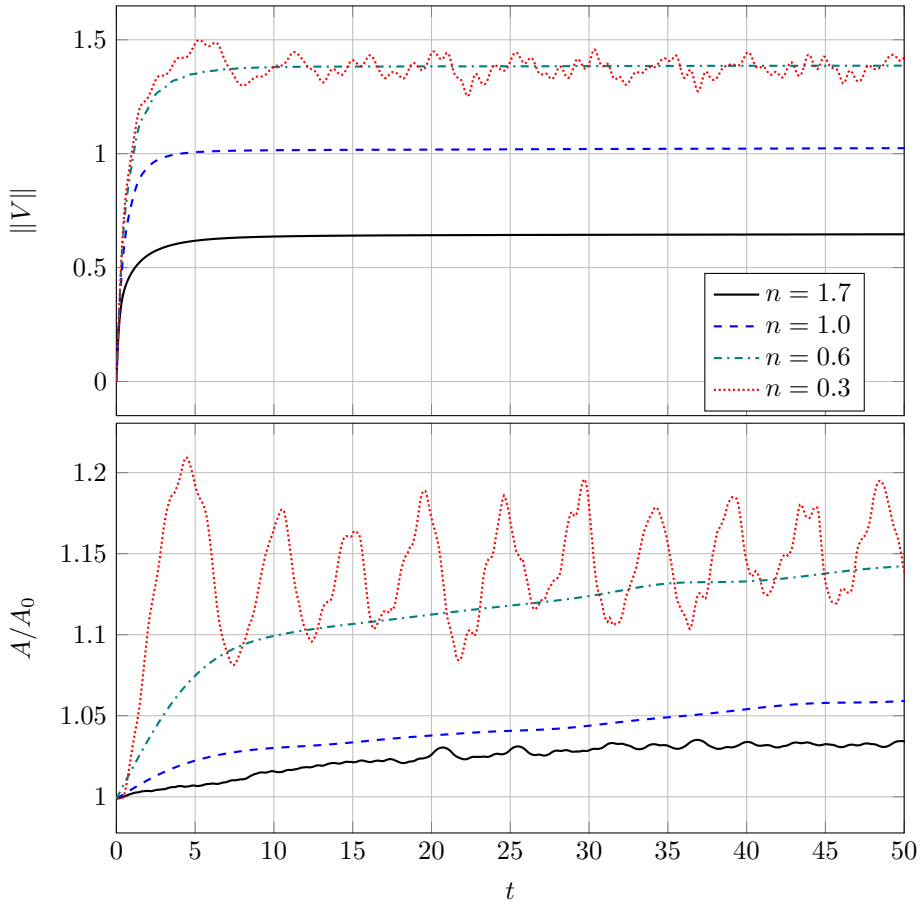

FIGURE 3.6: Time evolution of the bubble rising velocity magnitude (top) and the bubble interface area ratio (bottom) for different flow indexes.

Notably, the information presented at the bottom of figure 3.6 is distinct because it uses the actual normalized bubble interface area rather than a bubble shape factor, measuring based on the maximum and minimum characteristics length, to trace the evolution of the interface growth. The explanation provided in this context is more accurate because it allows for a direct calculation of the surface area of the bubble, which provides a more precise measurement. For $n = 0.6$, 1.0, and 1.7, the rate of bubble interface deformation quickly saturates and stays almost constant throughout the numerical experiment. On the contrary, even though there is an oscillating pattern in the interface area for $n = 0.3$, it seems to increase at a slower rate compared to the other cases. When the bubble area, the velocity of the bubble in the y-direction, and the velocity magnitude for the case where $n = 0.3$ are subjected to a fast Fourier transform, the dominant frequency for both the bubble area and velocity in the y-direction is 0.2, while for the velocity magnitude, it is 0.4.

3.2.2 Effects of the Peclet number and rheological characteristics on the heat/mass transfer across the bubble interface

This section examines how the mass transfer across the bubble interface is influenced by both the flow index and Peclet number. In addition to analyzing several flow indexes as done previously, the study also explores seven different Peclet numbers, namely 10, 100, 200, 400, 600, 800, and 1000. The relationship between the surface-averaged Sherwood number and time for various Peclet numbers and flow indexes is illustrated in figure 3.7. The figure reveals that, for $n = 1$ and $n = 1.7$, the surface-averaged Sherwood number stabilizes at a constant value, while for the shear-thinning cases, it fluctuates periodically over time. The reason for the periodic fluctuations observed in the surface-averaged Sherwood number in shear-thinning fluids is because of the time-varying diameter of the bubble and the oscillatory nature of its rising velocity. Performing a fast Fourier transform on the surface-averaged Sherwood number as a function of time revealed that, in the case where $n = 0.3$, the main frequency of the surface-averaged Sherwood number is 0.2. This frequency is equivalent to the frequency of the bubble rising velocity in the y-direction and the frequency of the bubble area. In order to obtain a constant value for the surface-averaged Sherwood number in shear-thinning cases, the time-averaged value of $\langle Sh \rangle$ is computed.

According to Kishore et al. (45), a correlation was developed for the average Sherwood number to describe the mass transfer between a fluid sphere and power-law liquids. Their study utilized a simplified model in which a spherical and rigid drop was assumed to move steadily in an infinite two-dimensional power-law fluid medium, with the drop size remaining constant despite mass transfer between the two phases. This simplification allowed for the use of quasi-steady state assumptions in the analysis. Under the assumption of a quasi-steady state, Kishore et al. (45) derived a correlation for the average Sherwood number, which is a function of the Reynolds number, Peclet number, flow index, and viscosity ratio. This correlation describes the mass transfer between a fluid sphere and power-law liquids, assuming that the transfer occurs steadily from the fluid sphere to the surrounding fluid. Specifically, they assumed that the quantity of scalar (e.g. mass, heat, or

momentum) inside the sphere is constant over time.

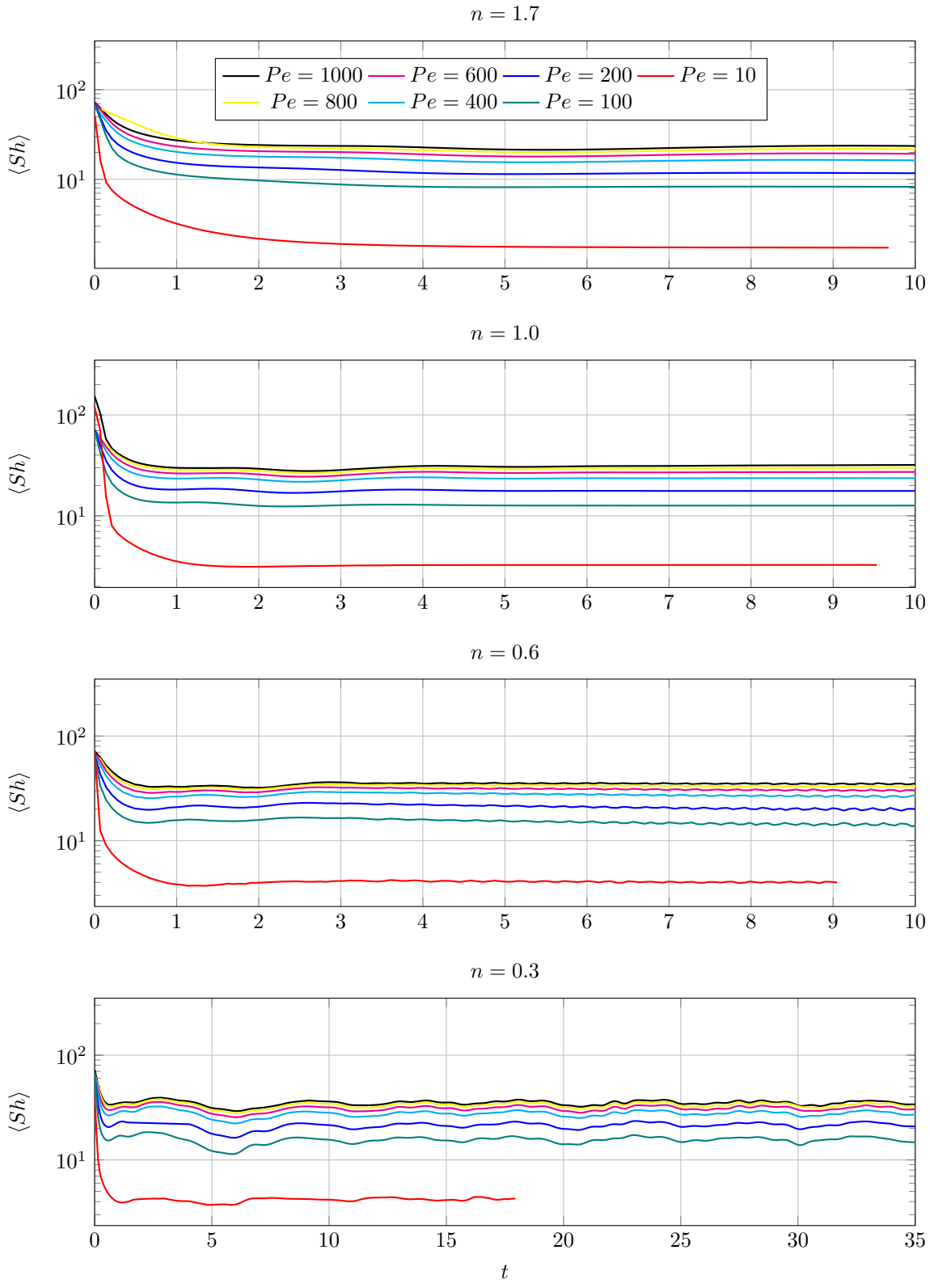

FIGURE 3.7: Time evolution of the surface-averaged Sherwood number for different Peclet numbers and flow indexes

The correlation developed by Kishore et al. (45) for the average Sherwood number, under the assumptions of quasi-steady state and constant scalar quantity inside the fluid sphere, is as follows:

$$\langle Sh \rangle = \left[\frac{1.19(n+1)}{1.7n+1.5}\right] Re_A^{0.53}\left(\frac{Pe}{Re_A}\right)^{0.42}(\mu^\star)^{-0.14} + \left(\frac{n+1}{1.5n}\right) Pe^{-0.15}(\mu^\star)^{0.25}. \quad (3.1)$$

Figure 3.8 (top) compares the surface-averaged Sherwood number with the experimental results of Roudet et al. (93) for the Newtonian case, while Figure 3.8 (bottom) compares the surface-averaged Sherwood number obtained in the present study with the averaged Sherwood number calculated by Kishore et al. (45). In Figure 3.8 (top), the comparison of the present study results with the experimental data of Roudet et al. (93) for the Newtonian case shows good agreement, indicating that the present study model is capable of accurately predicting mass transfer in this case. The present study's surface-averaged Sherwood number prediction has some slight differences from the experimental results, which may be attributed to the simplifying assumptions made in the study or possible experimental uncertainties. The dissimilarities between the results obtained in the present study and those obtained by Kishore et al. can be attributed to the different conditions in each study. Specifically, Kishore et al. considered a non-deformable and axisymmetric liquid drop with a constant scalar value within the bubble, situated in an infinite power-law fluid. Conversely, the current study focuses on a deformable gas bubble that rises within both Newtonian and non-Newtonian fluids modeled using the Carreau method, with a varying scalar value within the bubble. Figure 3.9 presents a comparison of the surface-averaged Sherwood number against the flow index for various Peclet numbers, showcasing the differences between our findings and those of (45).

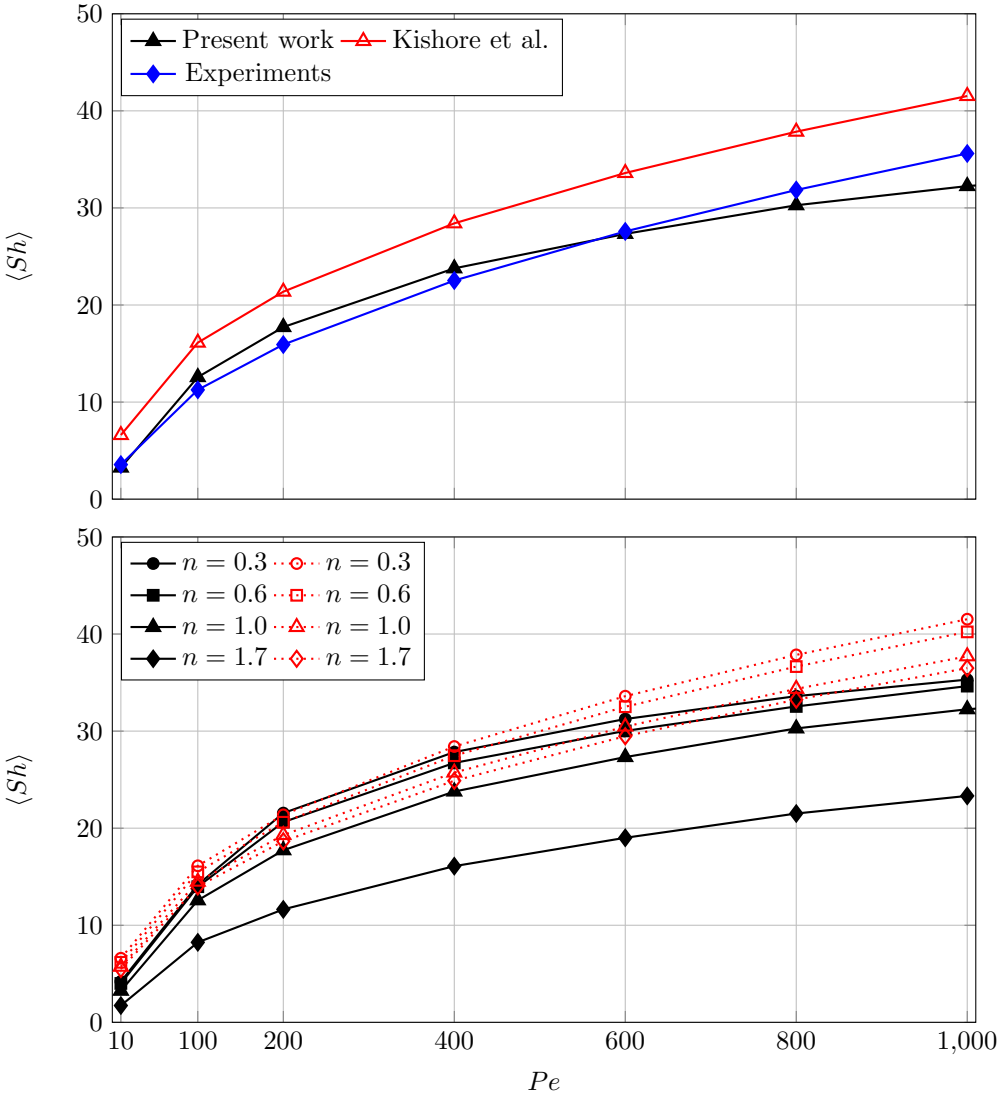

FIGURE 3.8: Surface-averaged Sherwood number versus Peclet number. Top panel: comparison among the results of the present study, the results of Kishore et al. (*45*), and experimental results of Roudet et al. (*93*) for $n = 1.0$. Bottom panel: comparison between the present study in black and a study by Kishore et al. (*45*) in red for several different flow indexes.

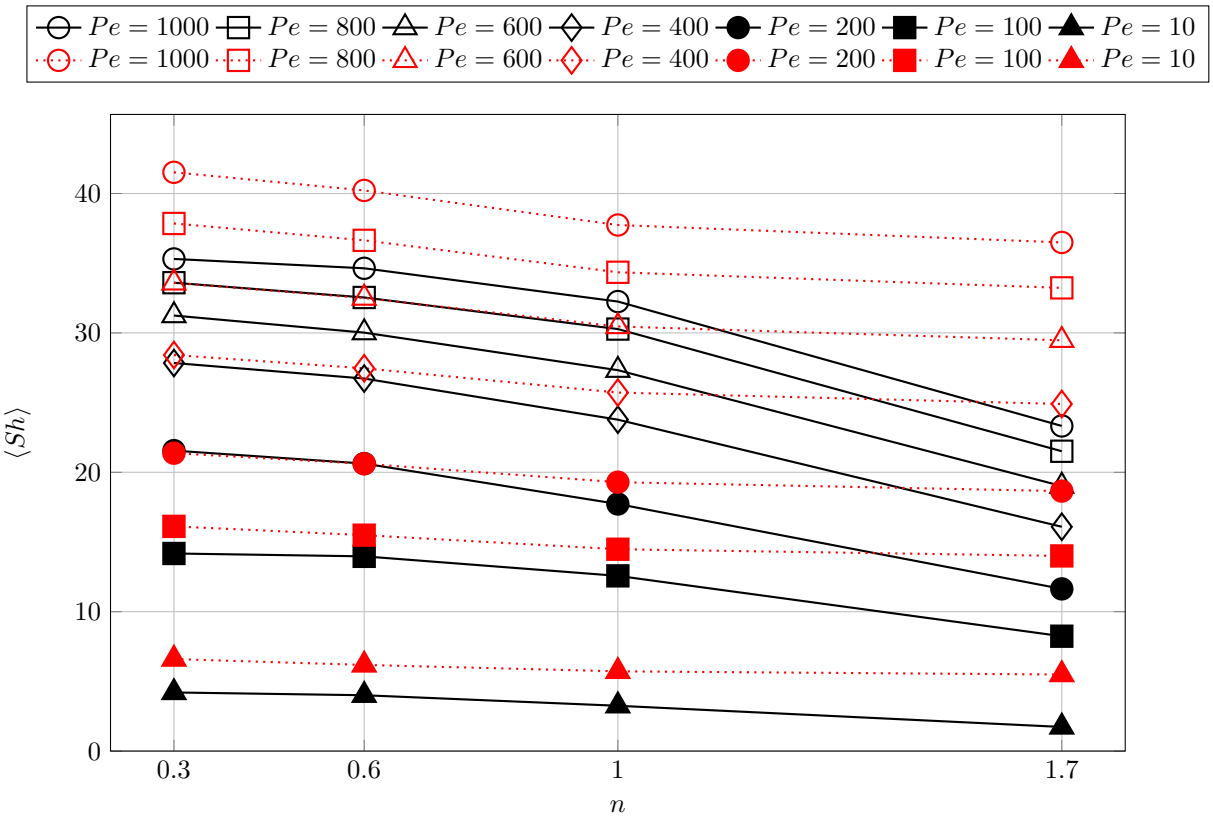

FIGURE 3.9: Surface-averaged Sherwood number versus flow index for different Peclet numbers. The results of the present study and the results of Kishore et al. (*45*) are in black and red, respectively.

The current numerical results allow for the development of a straightforward correlation (*94*) for the surface-averaged Sherwood number. This correlation can be used to calculate the mass transfer rate in a gas-liquid system with a rising deformable bubble, regardless of whether the ambient fluid is Newtonian or non-Newtonian:

$$\langle Sh \rangle = 2.15 \ln\left(\frac{Pe}{n^n}\right) \qquad \begin{matrix} 0.3 \leq n \leq 1.7 \\ 10 \leq Pe \leq 1000 \end{matrix} . \tag{3.2}$$

The local deformation of fluid interfaces is significantly influenced by the strain-rate tensor in non-Newtonian cases, as investigated in this article. This finding is consistent with the work of Vela-Martín and Avila (*95*), who demonstrated that the local variation of surface energy is dependent on the strain rate tensor. In this study, it is observed that the strain-rate tensor has a strong impact on the local deformation of fluid interfaces, as shown in figure 3.6 (bottom). Shear-thinning fluids exhibit

greater deformation due to larger velocity gradients, whereas shear-thickening fluids experience less deformation due to smaller velocity gradient values. Additionally, the strain-rate tensor magnitude at the interface is greater for shear-thinning fluids than for shear-thickening fluids.

3.3 Discussion

This study involves numerical simulations of a single rising bubble in a large tank, aimed at investigating the effects of rheological properties on bubble dynamics and heat/mass transfer in the surrounding fluids. For the specified parameters, the bubble rises vertically along the center line of the cavity in Newtonian fluids. However, decreasing the flow index (shear-thinning) results in an increase in the rising velocity of the bubble, leading to a rise in the local Ga number and causing the bubble trajectory to shift to a zigzag motion. This shift indicates that the bubble dynamics have moved to the oscillatory region in Figure 3.2. Conversely, an increase in the flow index (shear-thickening) leads to a decrease in the rising velocity and local Ga number, causing the bubble dynamics to shift to the axisymmetric region.

In shear-thickening fluids, the local viscosity increases, which results in a reduction of momentum diffusion and smoothing of local velocity gradients, leading to a decrease in the rate of strain. Consequently, the deformation of the fluid interface is not significant, and the bubble shape remains nearly spherical with a slight increase in bubble area. On the other hand, decreasing the flow index results in a decrease in the local viscosity near the bubble, leading to an increase in momentum diffusion, local velocity gradients, and ultimately, the rate of strain. This increase in the rate of strain causes more deformation of the bubble, resulting in a larger bubble area. The increase in both bubble area and rising velocity results in faster heat/mass transfer from the bubble to the surrounding fluid.

At low Peclet numbers, variations in the flow index have a negligible impact on the surface-averaged Sherwood number. However, at high Peclet numbers, decreasing the flow index results in an increase in the surface-averaged Sherwood number, indicating reduced efficiency of mass transfer at higher flow indexes. Decreasing

the flow index leads to an increase in the thickness of the scalar boundary layer surrounding the bubble. Additionally, the oscillatory behavior and deformation of the bubble increase in complexity and three-dimensionality as the flow index decreases.

To find correlations for the surface-averaged Sherwood number and rising velocity magnitude of a single bubble, simulations were performed for 28 different sets of (Ga, Bo) as presented in table 3.1, along with 6 different Peclet numbers (10, 100, 200, 400, 800, and 1000) and 2 different flow indexes (0.3 and 1.0), resulting in a total of 336 cases. The correlations were based on Ga, Bo, n, and Pe for the surface-averaged Sherwood number and on Ga, Bo, and n for the rising velocity magnitude of the bubble. However, to keep the thesis concise, the related results are not presented.

Ga	Bo	Ga	Bo	Ga	Bo	Ga	Bo
10	1	30	40	60	20	200	0.8
10	10	40	15	60	40	200	3
10	30	40	30	60	50	200	10
20	20	40	40	70	20	300	0.7
20	70	50	30	70	50	300	3
30	2	50	70	100	15	300	10
30	10	50	100	100	20	300	100

TABLE 3.1: Different sets of (Ga, Bo).

Chapter 4

A pair of bubbles rising

In the previous section, we delved into a research study that scrutinized the transfer of heat and mass across a single bubble interface. However, in real-world industrial scenarios, it is far more common to encounter multiple bubbles, and their interactions can significantly influence the heat and mass transfer process. As bubbles rise through gas-liquid systems, they repeatedly merge and break apart upon contact with other bubbles. This dynamic process causes alterations in both the interfacial area of the bubbles and their rising velocity, ultimately leading to changes in the rate of heat and mass transfer.

To investigate this phenomenon, this section presents a numerical study that explores the motion, interaction, and passive scalar transport of a pair of bubbles as they rise in Newtonian and shear-thinning fluids. The study evaluates the impact of various parameters such as (Ga, Bo), the radius ratio of the bubble pair, n, and λ on the system. By considering the effects of these parameters, the study aims to better understand the complex mechanisms underlying heat and mass transfer in multiphase systems.

4.1 Physical model

Figure 4.1 provides an illustration of the numerical domain employed in this study. The domain is a cubic box filled with either a Newtonian or non-Newtonian fluid, with a non-dimensional length of 120. The characteristic length scale of the problem is $d = 2R$, where R denotes the radius of the leading bubble (LB) and trailing bubble (TB), both of which are spherical in shape. The LB and TB are initially located at $(x_{LB}, y_{LB}, z_{LB}) = (0, 17, 0)$ and $(x_{TB}, y_{TB}, z_{TB}) = (0, 15, 0)$, respectively, and have zero

velocity. The use of a large box ensures that the influence of wall effects on bubble dynamics is minimized. The initial separation distance between the centers of the bubbles, denoted by s, is set at $4R$ for all cases. Additionally, the Peclet number of the gas bubbles is held constant at 1000, while that of the surrounding fluid is fixed at 10^7. Finally, the values of λ and n for the shear-thinning fluids used in this study are taken from the experiments of Zhang et al. (*91*), as well as numerical simulations conducted by Premlata et al. (*92*) and Cano-Lozano and Mart'ınez-Baz'an (*96*).

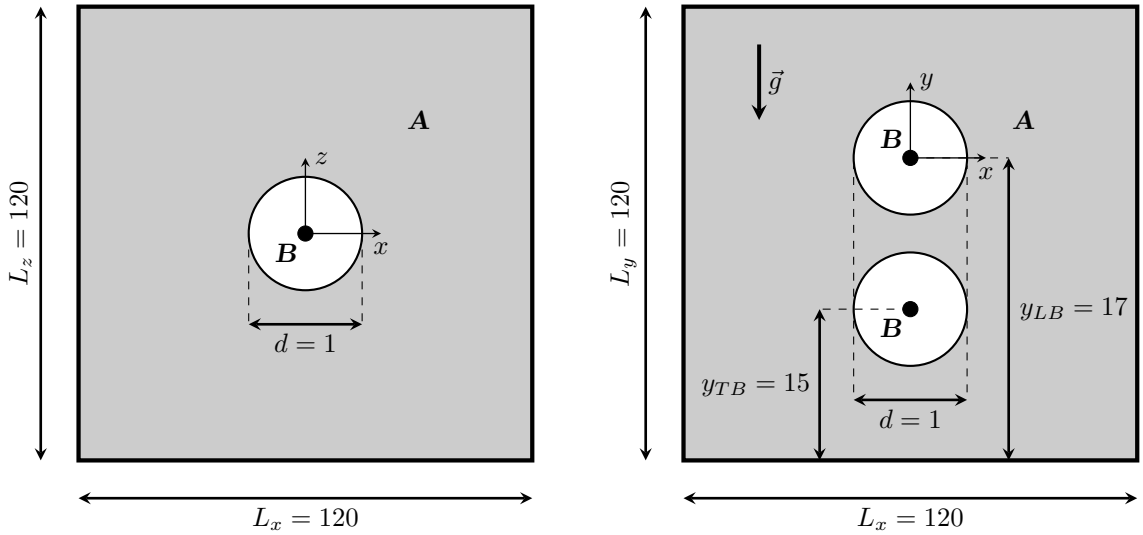

FIGURE 4.1: Top and side views of the computational domain (not to scale) showing the flow configuration with initially spherical bubbles of fluid B and non-dimensional diameter $d = 1$; one placed at $y_{TB} = 15$ and another placed at $y_{LB} = 17$ in a $L_x = L_y = L_z = 120$ cubical box filled with fluid A.

4.2 Results and discussion

The aim of this section is to investigate the dynamics of a pair of bubbles rising in a tank filled with either a Newtonian or a shear-thinning fluid. The investigation will focus on analyzing how various parameters impact the transfer of passive scalar across the interface of the bubbles, with a particular emphasis on the influence of the *Ga* and *Bo* numbers, which are dimensionless groups representing the relative importance of buoyancy and viscous forces, respectively, as well as the ratio of the bubble pair radius, the inelastic time constant λ, and the flow index n. The results of this section will provide valuable insights into the behavior of bubbles in industrial

processes and aid in the development of more efficient and cost-effective methods for mass transfer.

Depending on the flow set-up configuration and conditions, a few distinct motion patterns are known to characterize the dynamics of a pair of in-line bubbles, which include side escape, Drafting-Kissing-Tumbling (DKT), and coalescence. In the side escape scenario, the LB provides a sheltering effect that initially increases the rising velocity of the TB. However, the TB eventually deviates from its vertical trajectory and escapes laterally from the wake of the LB. In the DKT scenario, the TB's rising velocity exceeds that of the LB, leading to drafting. The TB eventually touches the LB (kissing) and rotates (tumbling), resulting in both bubbles continuing to rise in a side-by-side configuration. In the coalescence scenario, the LB's sheltering effect once again causes an increase in the rising velocity of the TB, eventually leading to the TB catching up with the LB and both bubbles merging into a single body that continues to rise.

4.2.1 Bubble dynamics and mass transfer rate at different regimes of $Ga - Bo$

Galilei number and Bond number are dimensionless parameters that can significantly impact the dynamic behavior of the bubbles rising in a fluid. The Galilei number is a measure of the ratio of buoyancy forces to viscous forces, while the Bond number is a measure of the relative importance of surface tension forces to gravity forces. On the other hand, the shear-thinning behavior of the fluid can affect the values of Ga and Bo. Therefore, understanding the impact of Ga and Bo on bubble dynamics is crucial for controlling multiphase systems in chemical processing or environmental applications, while studying shear-thinning effects is an active research area with significant implications for these industries.

This section investigates how Ga and Bo numbers impact the dynamic behavior of two bubbles rising in Newtonian ($n = 1.0$) and shear thinning ($n = 0.5, \lambda = 6$) fluids. Additionally, it examines how these numbers affect the transfer of passive scalar from the bubbles into the surrounding fluid. The study considers five different sets of (Ga, Bo) values that correspond to different regimes, namely I. $(10, 1)$, II.

(10, 100), III. (50, 2), IV. (30, 100), and V. (100, 100). This study sheds light on the complex interplay between Ga and Bo numbers, and the dynamic behavior of bubbles in different fluid media. The findings have practical implications in various fields, including chemical engineering, materials science, and environmental sciences, where bubble dynamics play a crucial role.

Regime I

In this regime, if there is only one bubble present in a fluid that behaves according to Newtonian physics, it will rise straight up while maintaining its axisymmetric shape with minimal deformation. However, if there are two bubbles present with differing initial vertical positions, their movements and behavior can become considerably more complex due to the effects of nearby bubble interactions. These interactions can be analyzed and quantified by precisely tracking the position of each bubble in three dimensions, specifically by calculating the instantaneous relative position of each bubble in the i-th direction di_i as $di_x = x_{LB} - x_{TB}$, $di_y = y_{LB} - y_{TB}$, and $di_z = z_{LB} - z_{TB}$.

In figure 4.2(a), a sequence of instantaneous snapshots is presented to illustrate the bubble interfaces and the accompanying streamlines of the background flow for two distinct cases: non-Newtonian ($n = 0.5$, $\lambda = 6$) and Newtonian ($n = 1.0$). The top row depicts the non-Newtonian case, while the bottom row represents the Newtonian case. Figure 4.2(b) and (c) demonstrate the time-dependent changes in the instantaneous distance and rising velocity magnitude of the bubbles, $\|V\|$, respectively.

Despite the differences in rheology, both pairs of bubbles initially rise in tandem and follow a similar trajectory until instability in the wake of the leading bubble causes the pair to shift laterally. In the non-Newtonian case, the faster trailing bubble eventually breaks free from the wake of the leading bubble, resulting in a quasi-steady configuration where both bubbles rise side by side at similar velocities. This case follows the side escape scenario. In contrast, in the Newtonian case, the drafting stage lasts until the trailing bubble catches up with the leading one and they reach the same velocity (known as kissing). The pair then rises in a straight line until they start to separate laterally due to transverse flow disturbances. Eventually, the

trailing bubble rotates (tumbling), breaks free from the wake of the leading bubble, and reaches a side-by-side arrangement with the leading bubble, maintaining this configuration as they continue to rise at similar speeds. This case follows the DKT scenario.

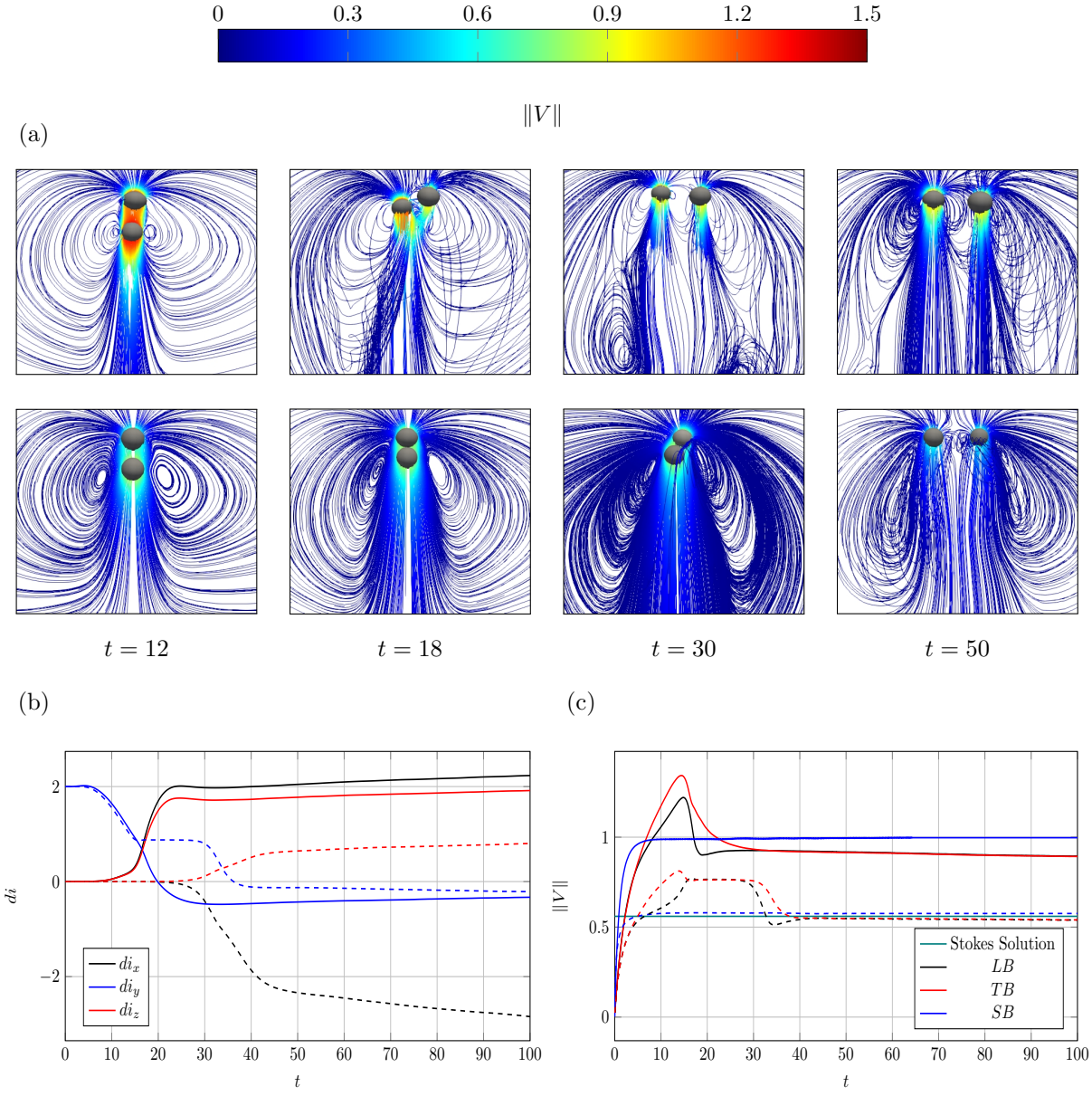

FIGURE 4.2: Evolution of several characteristics for a pair of bubbles rising in regime I with (*Ga*,*Bo*)=(10,1). (a): Streamlines and shape of the bubbles; top: non-Newtonian case ($n = 0.5$, $\lambda = 6$), and bottom: Newtonian case ($n = 1.0$). The colored map represents the velocity magnitude. (b): Instantaneous distance between the bubbles versus time; solid lines: non-Newtonian case, and dashed lines: Newtonian case. (c): Rising velocity magnitude of the bubbles versus time; solid lines: non-Newtonian case, and dashed lines: Newtonian case.

Upon comparison with the single bubble case, the velocity evolution for each bubble in figure 4.2(c) reveals an initial acceleration phase due to the wake sheltering effect, followed by saturation to values slightly lower than those observed in the single bubble case (depicted in blue). Additionally, the Stokes solution for the terminal velocity of a single isolated small bubble (97) is included for completeness (shown as the green solid line).

In contrast to the axisymmetric nature of the single bubble case with limited interface deformation, the introduction of a second bubble induces flow perturbations that considerably enhance the flow dynamics, leading to more significant interface deformations even at such modest values of Ga and Bo.

The surface-averaged Sherwood number for the leading (black) and trailing (red) bubbles rising in shear-thinning (solid) and Newtonian (dashed) ambient fluids are shown in figure 4.3. For comparison, the evolution of the $\langle Sh \rangle$ value for a single bubble rising in the shear-thinning and Newtonian environments is also shown in figure 4.3 using solid and dashed blue lines respectively.

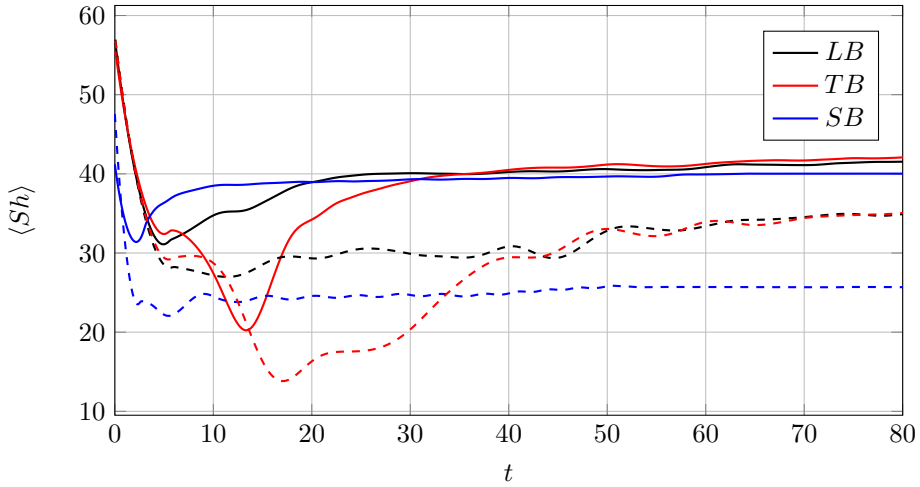

FIGURE 4.3: Evolution of surface-averaged Sherwood number for a pair of bubbles (black and red) and a single bubble (blue) rising in regime I with (Ga,Bo)=(10,1). Solid lines: non-Newtonian case ($n = 0.5$, $\lambda = 6$), and dashed lines: Newtonian case ($n = 1.0$).

After an initial fast decay in $\langle Sh \rangle$, and regardless of rheology, the $\langle Sh \rangle$ of the leading bubble is relatively similar to that found for a single bubble. In contrast, while the TB resides within the LB wake during the drafting stage leads to lower values of the averaged Sherwood number. As the TB abandons the wake during

the side escape or DKT and the pair evolves into a side-by-side arrangement, the average Sherwood grows back until reaching quasi-terminal and identical values for both bubbles. The higher average Sherwood number observed consistently in the shear-thinning scenario, in comparison to the Newtonian one, can be explained by a certain factor. In the shear-thinning case, there is a faster shift to the side-by-side configuration, resulting in an increased interfacial area between the bubbles and the surrounding fluid. As a result of this increased interfacial area, mass transfer rates at the bubble-fluid interface rise, leading to a higher average Sherwood number.

Regime II

If the surface tension is reduced to $Bo = 100$, a single bubble in a Newtonian fluid will fall into Regime II. Figure 4.4(a) shows that regardless of the fluid's rheology, bubbles in a rising pair eventually exhibit the "skirted" topology displayed in Figure 3.2 for a single bubble. In Regime I, the bubble pair will either escape to the side or undergo DKT scenario, which eventually leads to a side-by-side arrangement. However, at $(Ga, Bo) = (10, 100)$, the bubble pair coalesces into a single merged bubble (MB), which continues to evolve as expected according to figure 3.2.

Regarding the impact of rheology, the time for coalescence enabled by the TB acceleration due to the sheltering effects of the LB wake is approximately $t = 5$ for shear-thinning fluids and $t = 7$ for Newtonian fluids. The merged bubble Galilei and Bond numbers are approximately $Ga = 14$ and $Bo = 160$, respectively, which correspond to Regime II of a single bubble rising in a Newtonian fluid.

Figure 4.4(b) and (c) depict the vertical distance and velocity magnitude for both the Newtonian (represented by the dashed line) and non-Newtonian (represented by the solid line) cases. It can be observed that bubbles merge sooner in the non-Newtonian fluid compared to the Newtonian fluid, as they rise faster in the shear-thinning fluid. Similarly, after merging, a skirted merged bubble rises faster in the non-Newtonian fluid than in the Newtonian fluid, following a coalescence scenario. Furthermore, the rising velocity magnitude for a single bubble with the same Ga and Bo numbers is depicted in blue in the figure. It reveals that the rising velocity magnitude of the MB is higher than that of the SB for both Newtonian and non-Newtonian cases.

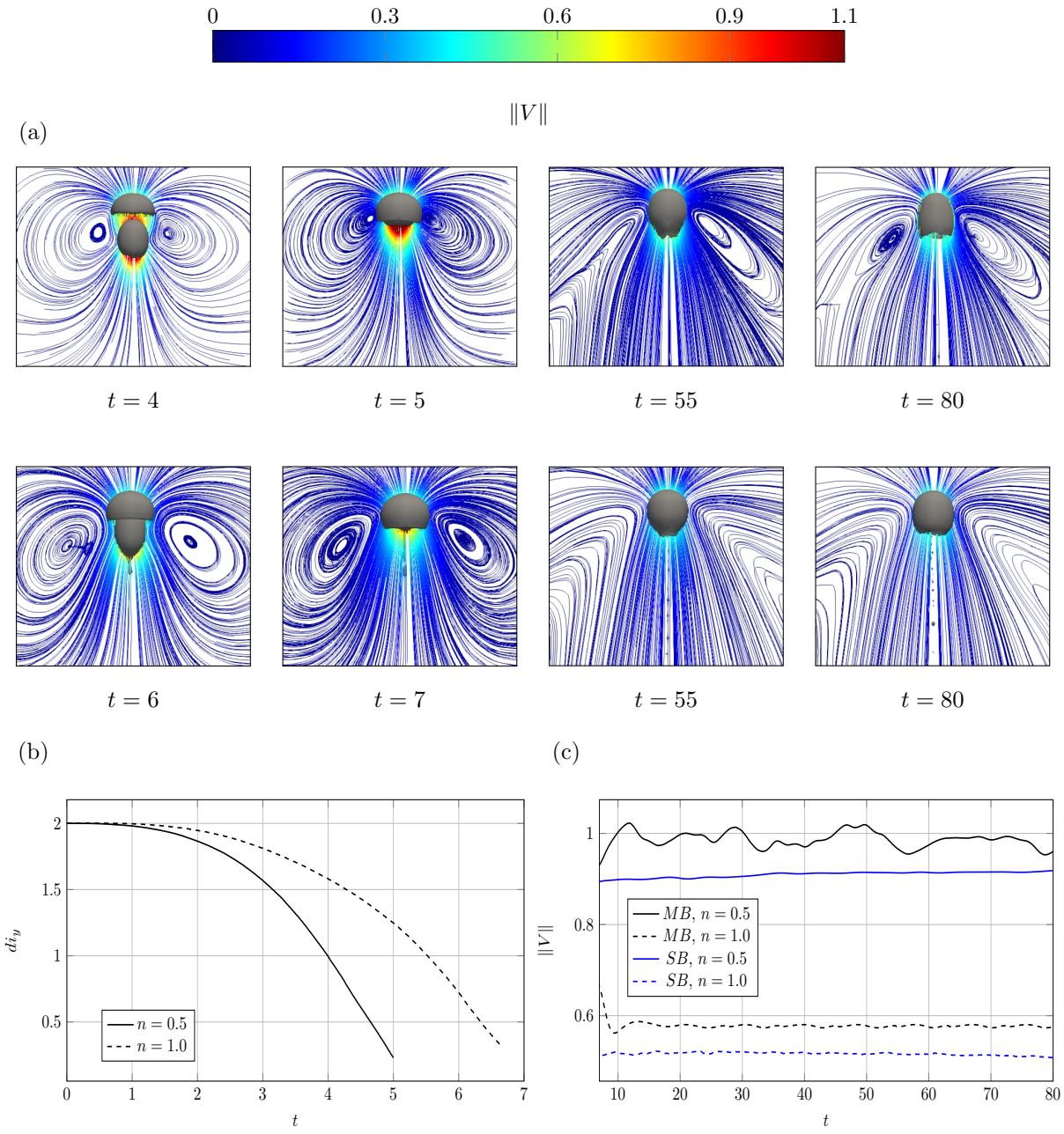

FIGURE 4.4: Evolution of several characteristics for a pair of bubbles rising in regime II with (*Ga*,*Bo*)=(10,100). (a): Streamlines and shape of the bubbles; top: non-Newtonian case ($n = 0.5$, $\lambda = 6$), and bottom: Newtonian case ($n = 1.0$). The colored map represents the velocity magnitude. (b): Instantaneous vertical distance between the bubbles versus time. (c): Rising velocity magnitude of MB (black) and SB(blue) versus time.

Figure 4.5 illustrates the surface-averaged Sherwood number for the merged bubble in both Newtonian and non-Newtonian cases in regime II, with (*Ga*,*Bo*)=(10,100). It is evident that the value of $\langle Sh \rangle$ for the Newtonian case ($\langle Sh \rangle$=16.7) is slightly larger than the non-Newtonian case ($\langle Sh \rangle$=15.5). When considering a single bubble

rising with the same conditions, the value of $\langle Sh \rangle$ is calculated as $\langle Sh \rangle_{SB,n=0.5} = 12.7$ and $\langle Sh \rangle_{SB,n=1.0} = 15.8$. These values are smaller than those observed for two bubbles rising. This finding is consistent with the fact that the overall interface surface for a given volume of the drop is smaller for a single bubble than for two bubbles.

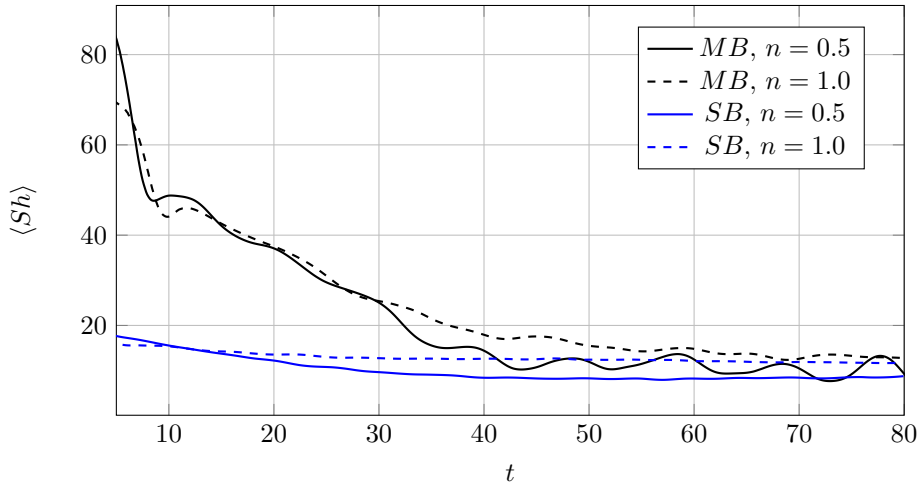

FIGURE 4.5: Surface-averaged Sherwood number of MB (black) and SB (blue) versus time; regime II with (*Ga*,*Bo*)=(10,100)

Regime III

In regime III, the dynamics of a single bubble are characterized by an oscillatory behavior, where the bubble follows a zigzag or spiral path as it rises. However, for a pair of bubbles, the dynamics may be different. It is possible that the presence of the second bubble could influence the path of the rising bubbles and cause them to exhibit different behavior than a single bubble. For instance, the bubbles may interact with each other and form vortices in the surrounding fluid, affecting the trajectory of their motion.

Figure 4.6 provides a detailed visualization of the time evolution of bubble shape, streamlines, instantaneous distance, and rising velocity magnitude of a pair of bubbles rising with *Ga* and *Bo* equal to 50 and 2, respectively. For the non-Newtonian case with $n = 0.5$ and $\lambda = 6$, the bubble pair exhibits the side escape scenario. During the first 10 units of time, the instantaneous distance between the bubbles remains almost constant. However, as the TB bubble rises and begins to shelter under the LB bubble, its rising velocity increases and surpasses that of the LB bubble. Consequently, the vertical distance between the bubbles decreases until TB eventually

escapes from the wake of LB. Following this, the bubbles continue to rise in a zigzag path with almost the same speed.

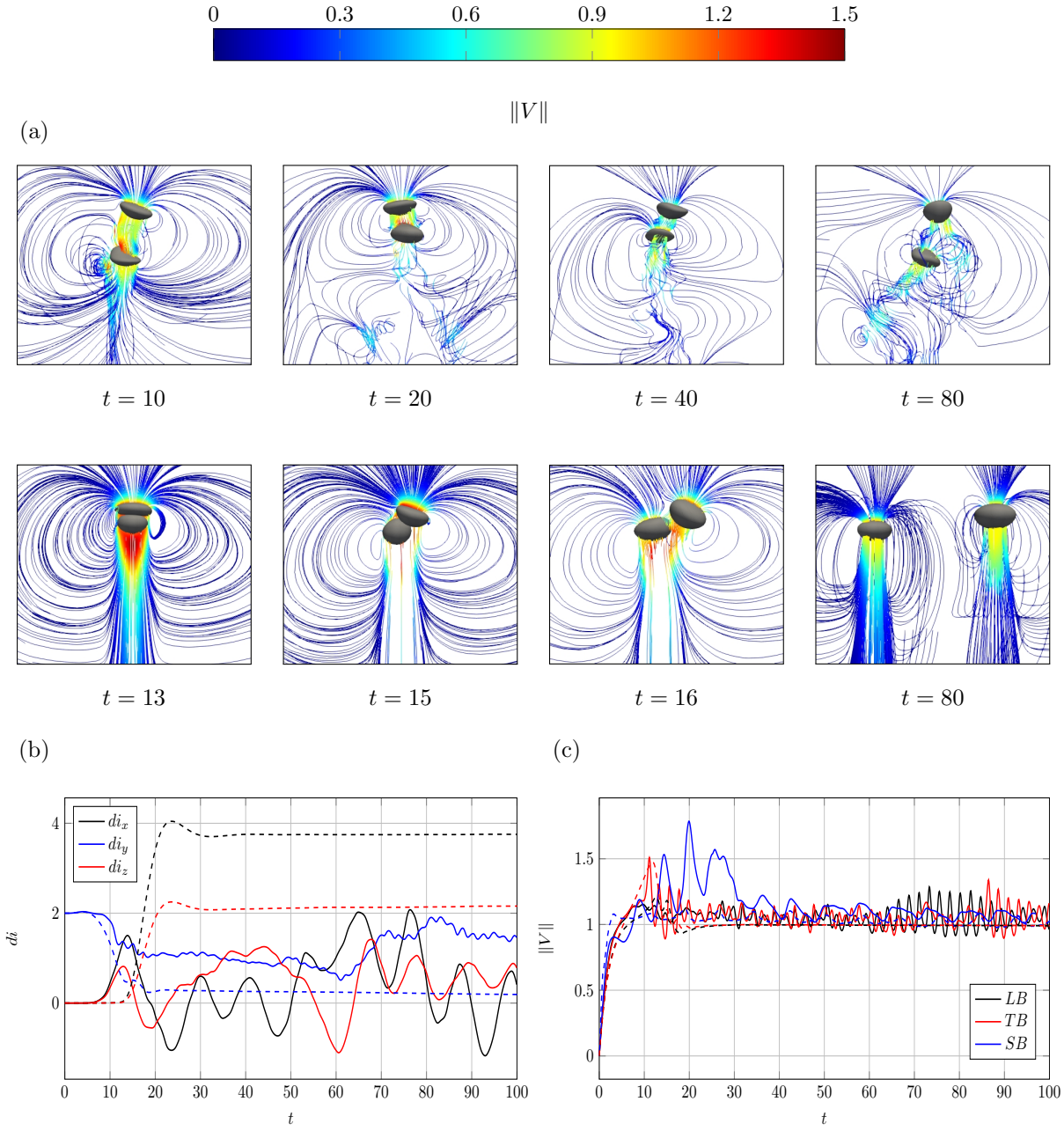

FIGURE 4.6: Evolution of several characteristics for a pair of bubbles rising in regime III with (Ga,Bo)=(50,2). (a): Streamlines and shape of the bubbles; top: non-Newtonian case($n = 0.5$, $\lambda = 6$), and bottom: Newtonian case ($n = 1.0$). The colored map represents the velocity magnitude. (b): Instantaneous distance between the bubbles versus time; solid lines: non-Newtonian case, and dashed lines: Newtonian case. (c): Rising velocity magnitude of the bubbles versus time; solid lines: non-Newtonian case, and dashed lines: Newtonian case.

When $n = 1.0$, the bubbles rise vertically at a constant distance from each other until reaching $t = 5$. Then, the sheltering effect causes TB to move faster than LB, resulting in a decrease in the distance between them. At $t = 13$, the rising velocity magnitude of both bubbles becomes equal and they touch each other, leading to instability to transverse disturbances and causing TB to rotate and escape from the wake of LB, a phenomenon known as tumbling. As TB increases its rising velocity, it moves away from LB. Finally, the vertical distance becomes zero, and the bubbles begin to rise side-by-side with the same velocity magnitude. This behavior corresponds to the DKT scenario. The behavior of a pair of bubbles rising in a non-Newtonian fluid in regime III is comparable to that of a single bubble rising in a Newtonian fluid, in that both exhibit oscillatory behavior. In contrast, a pair of bubbles in a Newtonian fluid eventually rise vertically after a brief transition period.

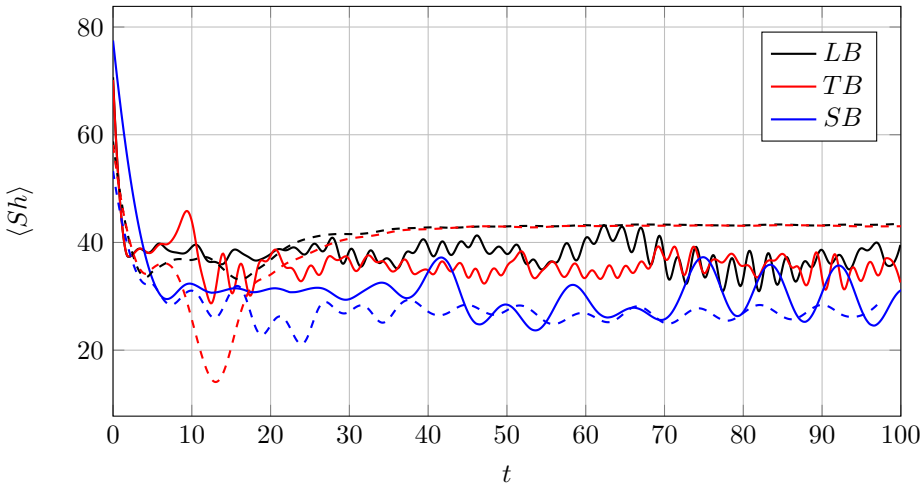

FIGURE 4.7: Evolution of surface-averaged Sherwood number for a pair of bubbles (black and red) and a single bubble (blue) rising in regime III with (Ga,Bo)=(50,2). Solid lines: non-Newtonian case ($n = 0.5$, $\lambda = 6$), and dashed lines: Newtonian case ($n = 1.0$).

Figure 4.7 presents the surface-averaged Sherwood number for LB and TB rising in regime III with (Ga,Bo)=(50,2), demonstrating that $\langle Sh \rangle$ is the same for both Newtonian and non-Newtonian cases, while the Newtonian case has a slightly higher $\langle Sh \rangle$ value ($\langle Sh \rangle$=43.3) compared to the non-Newtonian case ($\langle Sh \rangle$=37.1). The oscillatory behavior of $\langle Sh \rangle$ in the non-Newtonian case is due to the oscillatory dynamics of the bubbles. For a single bubble rising with the same conditions, the surface-averaged Sherwood number is calculated: $\langle Sh \rangle_{SB,n=0.5} = 34.55$ and $\langle Sh \rangle_{SB,n=1.0} = 34.3$, which are smaller than the values for two bubbles rising because of the smaller

interfacial surface area of the single bubble. It should be noted that for oscillatory $\langle Sh \rangle$, the time-averaged value is reported.

Regime IV

Figure 4.8 illustrates the shape of bubbles rising in a non-Newtonian fluid with $n = 0.5$ and $\lambda = 6$, revealing a peripheral breakup for both the LB and TB at the initial stage of rising before their merging at $t = 5$. Subsequently, the bubbles undergo repeated merging and breakup events, giving rise to the formation of larger bubbles and numerous satellites. The unique dynamic behavior of bubbles in regime IV can be distinguished, and a new scenario can be defined as the Coalescence-breakup (CB) scenario, which is marked by frequent mergings and breakups. The repeated merging and breakup of bubbles create intricate interactions between them, leading to the formation of many satellites. This scenario's behavior is more intricate than the three other scenarios (side escape, DKT, and coalescence). The primary cause of this behavior can be attributed to the high values of Ga and Bo numbers, which result in instability in the dynamics of the bubbles. This instability becomes more pronounced when the surrounding fluid is a shear-thinning fluid. When the surrounding fluid is a shear-thinning fluid, the instability in the bubble dynamics increases due to the reduced viscosity with increasing shear rate. This increased instability leads to the formation of many satellites in the CB scenario.

Understanding the dynamic behavior of bubbles in non-Newtonian fluids is crucial for various industrial and environmental applications, such as wastewater treatment and oil recovery. The unique behavior of bubbles in regime IV and the CB scenario highlights the importance of considering fluid rheology when designing and optimizing such processes.

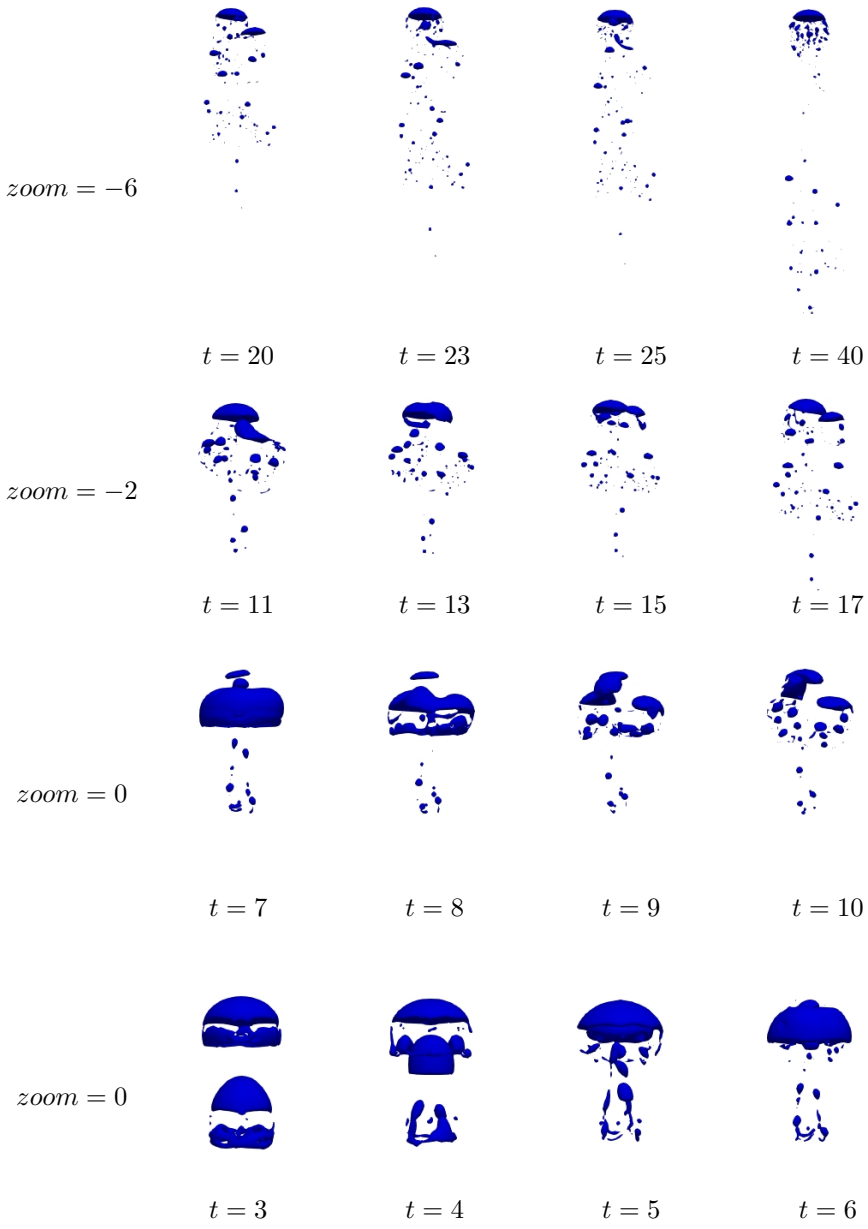

FIGURE 4.8: Shape of the bubbles rising in a non-Newtonian fluid ($n = 0.5$, $\lambda = 6$); regime IV with (Ga,Bo)=(30,100).

Figure 4.9 depicts the shape of bubbles rising in a Newtonian fluid with $n = 1.0$. In contrast to the non-Newtonian case, the bubbles have sufficient time to coalesce before any breakup occurs. The bubbles merge at $t = 5.05$, forming a larger bubble (MB) that rises vertically. Here, when the bubble breaks and small satellites form, they create more surface area that interacts with the surrounding fluid, resulting in a greater drag force acting on the satellites. This increased drag force slows down

the motion of the satellites, and consequently, the rising velocity of the bubble is reduced.

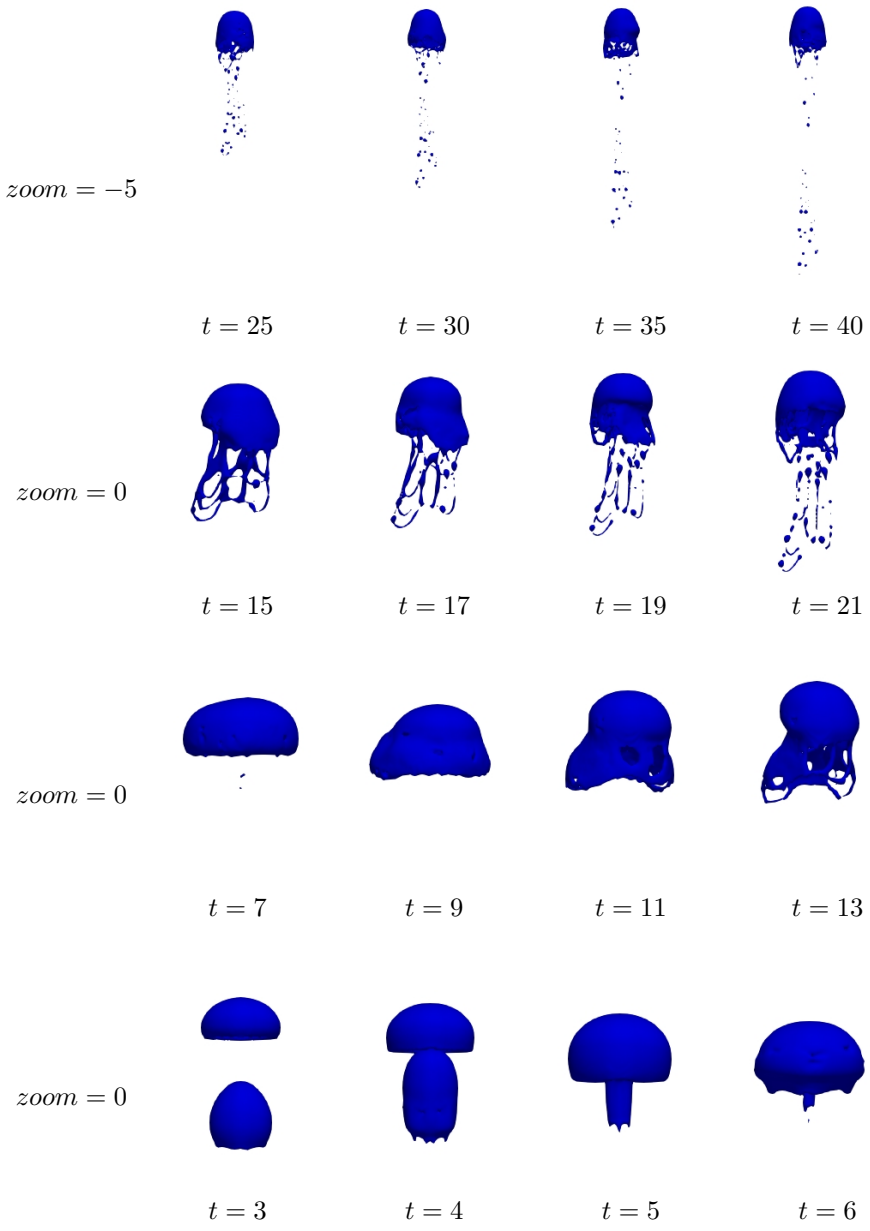

FIGURE 4.9: Shape of the bubbles rising in a Newtonian fluid ($n = 1.0$); regime IV with (*Ga*,*Bo*)=(30,100).

When two bubbles coalesce to form a larger bubble, the Galilei number and Bond number of the resulting larger bubble may be larger or smaller than the initial values of the two individual bubbles, depending on the specific conditions of the coalescence process. In general, if the resulting larger bubble has a larger radius and

a faster rise velocity than the initial bubbles, the Galilei number and Bond number of the larger bubble may be larger than the initial values. However, if the resulting larger bubble has a smaller radius and a slower rise velocity than the initial bubbles, the Galilei number and Bond number of the larger bubble may be smaller than the initial values.

As the MB rises, its shape transforms into a skirted bubble, indicating a shift in the dynamics behavior from regime IV to regime II. In contrast to the bubbles rising in non-Newtonian fluids, the bubbles in the Newtonian case follow a coalescence scenario. In the case of $n = 1.0$, the local Ga number of the merged bubble is smaller than the initial Ga number, owing to the smaller rising velocity of the MB compared to the initial bubbles. This reduction in local Ga number causes the shift in the dynamics behavior of the MB from regime IV to regime II. However, for $n = 0.5$, where the surrounding fluid is a shear-thinning fluid, the local Ga increases, causing the bubbles to break before merging.

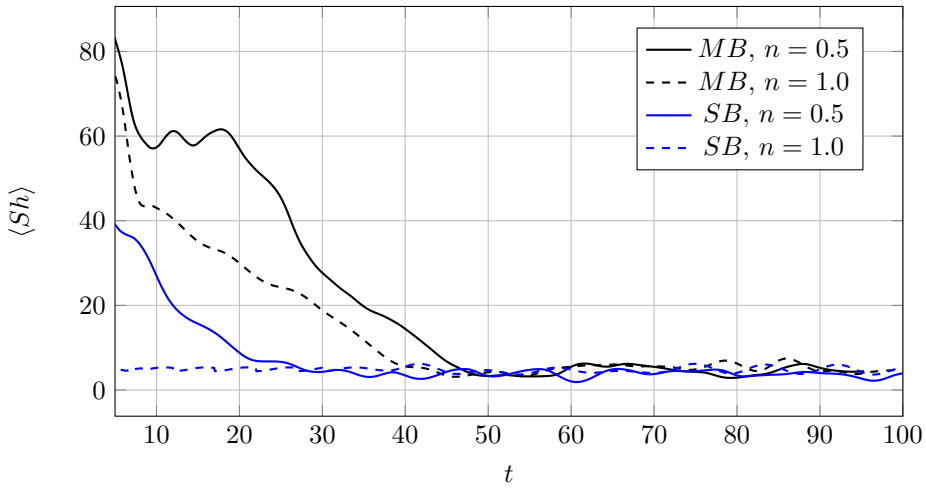

FIGURE 4.10: Surface-averaged Sherwood number of MB (black) and SB (blue) versus time; regime IV with (Ga,Bo)=(30,100).

In Figure 4.10, the Sherwood number averaged over time is presented for regime IV with (Ga,Bo)=(30,100). It should be noted that the reported value of $\langle Sh \rangle$ is the average value for all bubbles in the case of $n = 0.5$, while for $n = 1.0$, it is only reported for the MB. Both cases have a similar $\langle Sh \rangle$ value of approximately 4.5. However, when considering a single bubble rising under the same conditions, the calculated $\langle Sh \rangle$ values are smaller at $\langle Sh \rangle_{SB,n=0.5} = 3.3$ and $\langle Sh \rangle_{SB,n=1.0} = 4.4$, which can be

attributed to the difference in interfacial surface area between a pair of bubbles and a single bubble.

Regime V

Figure 4.11 displays the morphology of bubbles with $n = 0.5$ and $\lambda = 6$.

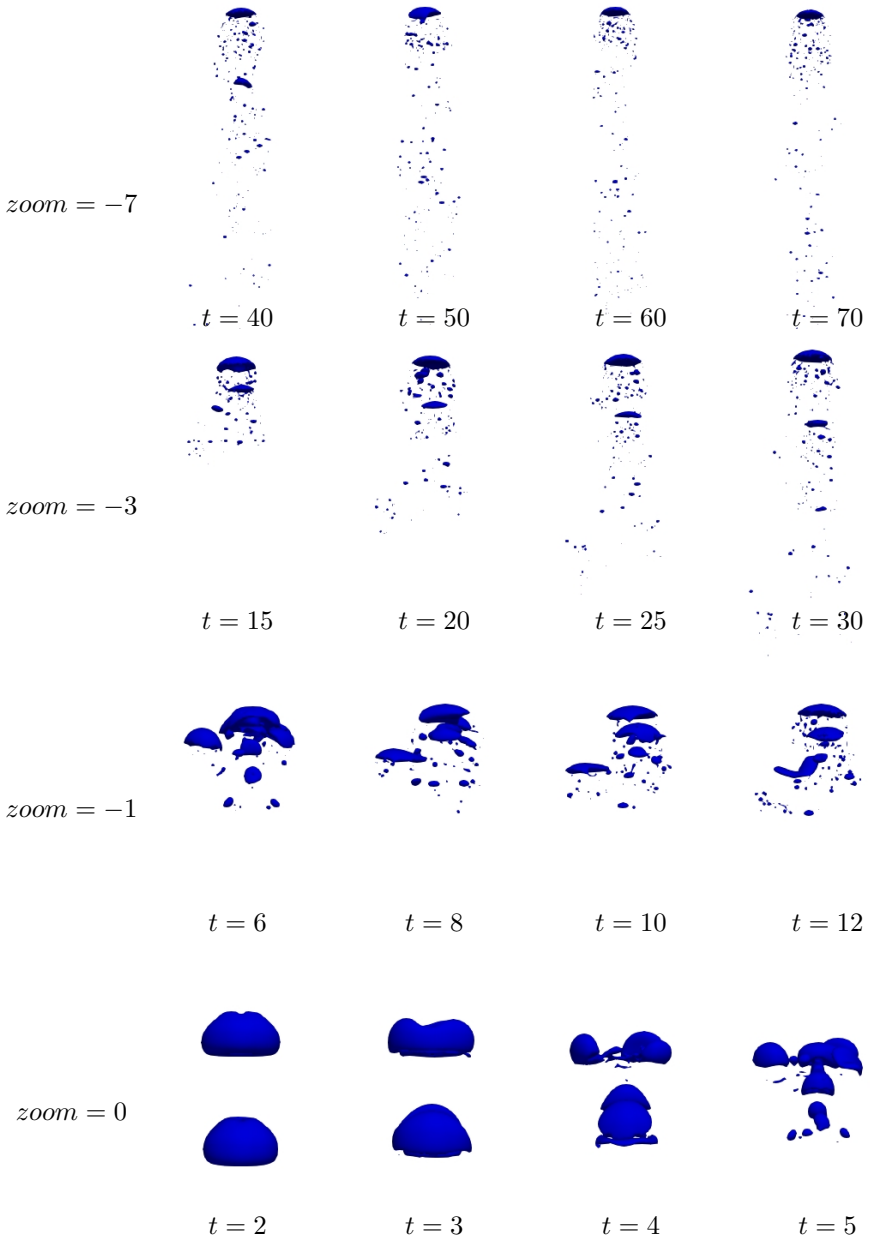

FIGURE 4.11: Shape of the bubbles rising in a non-Newtonian fluid ($n = 0.5$, $\lambda = 6$); regime V with (Ga,Bo)=(100,100).

Initially, both LB and TB experience central breakup at $t = 4$, before any merging occurs. Subsequently, the bubbles repeatedly merge and break, producing larger

bubbles along with numerous satellites. By $t = 15$, two primary bubbles are formed, which are smaller than the initial bubbles and are accompanied by many satellites. By the time $t = 50$ is reached, these two bubbles merge to form a larger bubble, with many small satellites, continuing to ascend. This situation corresponds to the CB scenario.

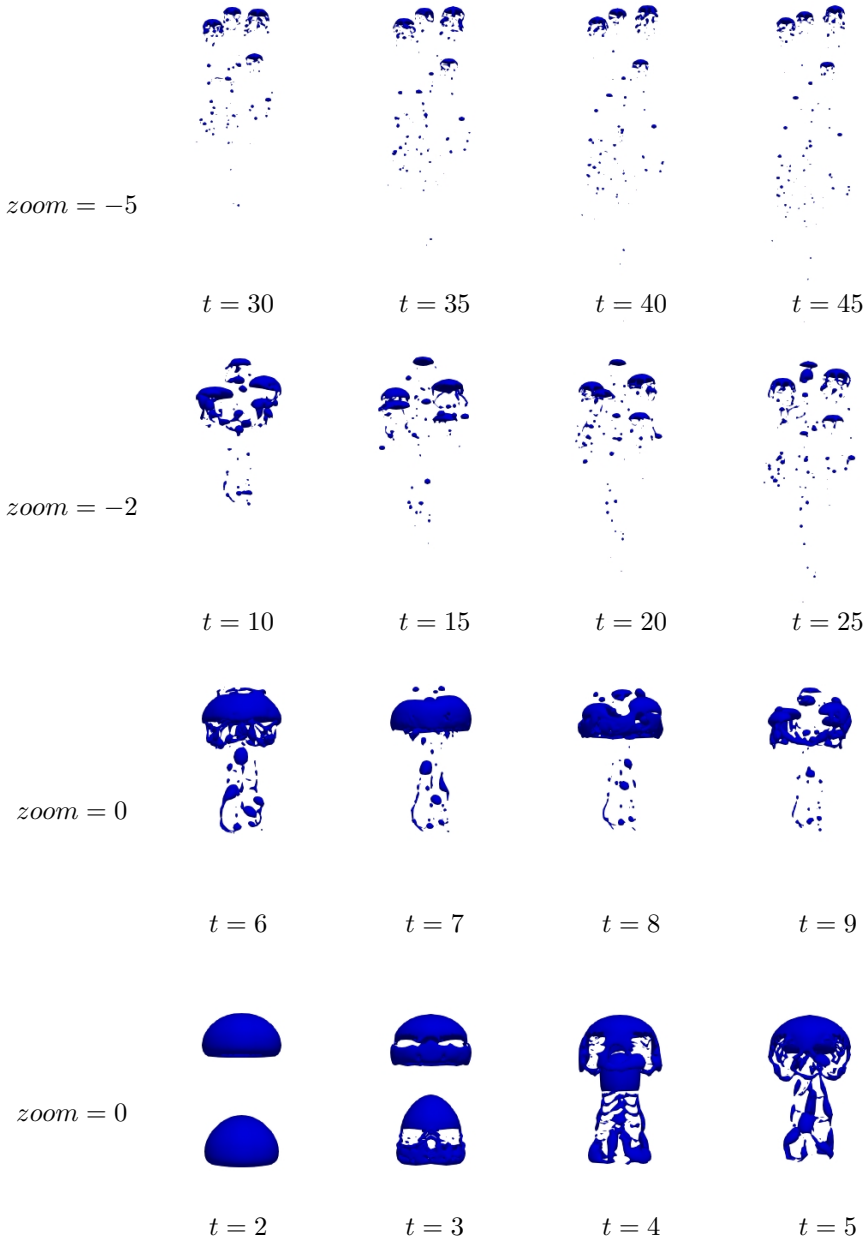

FIGURE 4.12: Shape of the bubbles rising in a Newtonian fluid ($n = 1.0$); regime V with (Ga,Bo)=(100,100).

Figure 4.12 displays the bubbles' shape for $n = 1.0$. Peripheral breakup occurs for both TB and LB at $t = 3$. Then, there is an initial merging at $t = 5$, forming

a merged bubble that continues rising until $t = 7$. At $t = 8$, the merged bubble experiences a central breakup, resulting in the formation of five bubbles and numerous satellites. Finally, at $t = 26$, four large bubbles with many small satellites are produced and continue to rise. This scenario also follows the CB scenario.

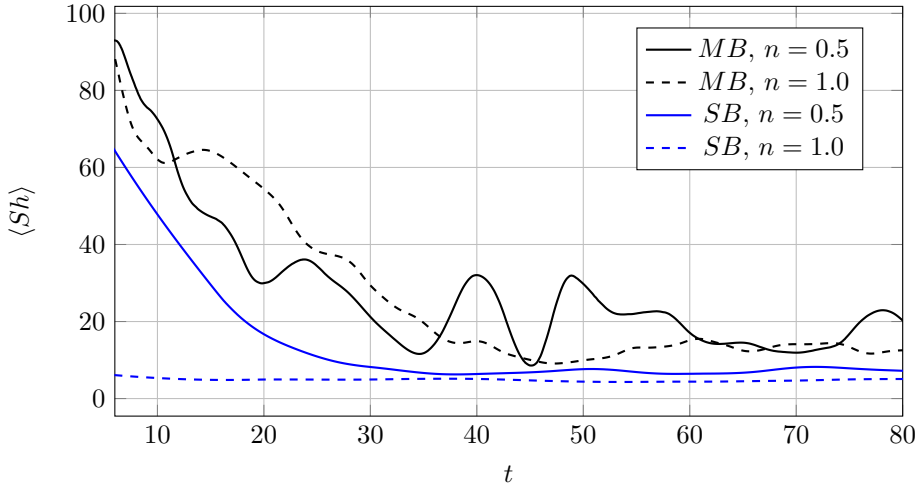

FIGURE 4.13: Surface-averaged Sherwood number of MB (black) and SB (blue) versus time; regime V with (*Ga*,*Bo*)=(100,100).

In figure 4.13, the surface-averaged Sherwood number is shown for regime V with (*Ga*,*Bo*)=(100,100). The mean value of all bubbles is reported for $\langle Sh \rangle$. For $n = 0.5$, the value of $\langle Sh \rangle$ is approximately 12.5, which is slightly larger than the value for $n = 1.0$ ($\langle Sh \rangle \approx 11.8$). When a single bubble rises under the same conditions, the surface-averaged Sherwood number is calculated as $\langle Sh \rangle_{SB,n=0.5} = 8.3$ and $\langle Sh \rangle_{SB,n=1.0} = 3.5$, which are lower than the values for two bubbles rising.

4.2.2 Effects of the bubble pair radius ratio, R_r

The bubbles that form in bubbly flows are not always of the same size. This variation in bubble size can occur due to a number of factors. For example, the size of the bubbles can be affected by the properties of the gas and liquid, the flow rate, and the presence of impurities in the system. In some cases, the bubbles may coalesce, leading to the formation of larger bubbles. The behavior of a bubbly flow system is not only influenced by the size of the bubbles but also by the distribution of bubble sizes, as both factors can have important implications for the overall behavior of the system (*98*).

The effects of the size of the bubbles on their interaction and the mass transfer rate have been studied in this section. The bubble pair radius ratio, defined as $R_r = R_{LB}/R_{TB}$ where R_{LB} and R_{TB} are the radius of the leading and trailing bubbles, respectively, has been used to investigate three different bubble pair radius ratios (1, 2, and 0.5) for $Ga = 50$ and $Bo = 2$ (regime III). Here, $Ga = 50$ and $Bo = 2$ are based on the smaller bubble in each case.

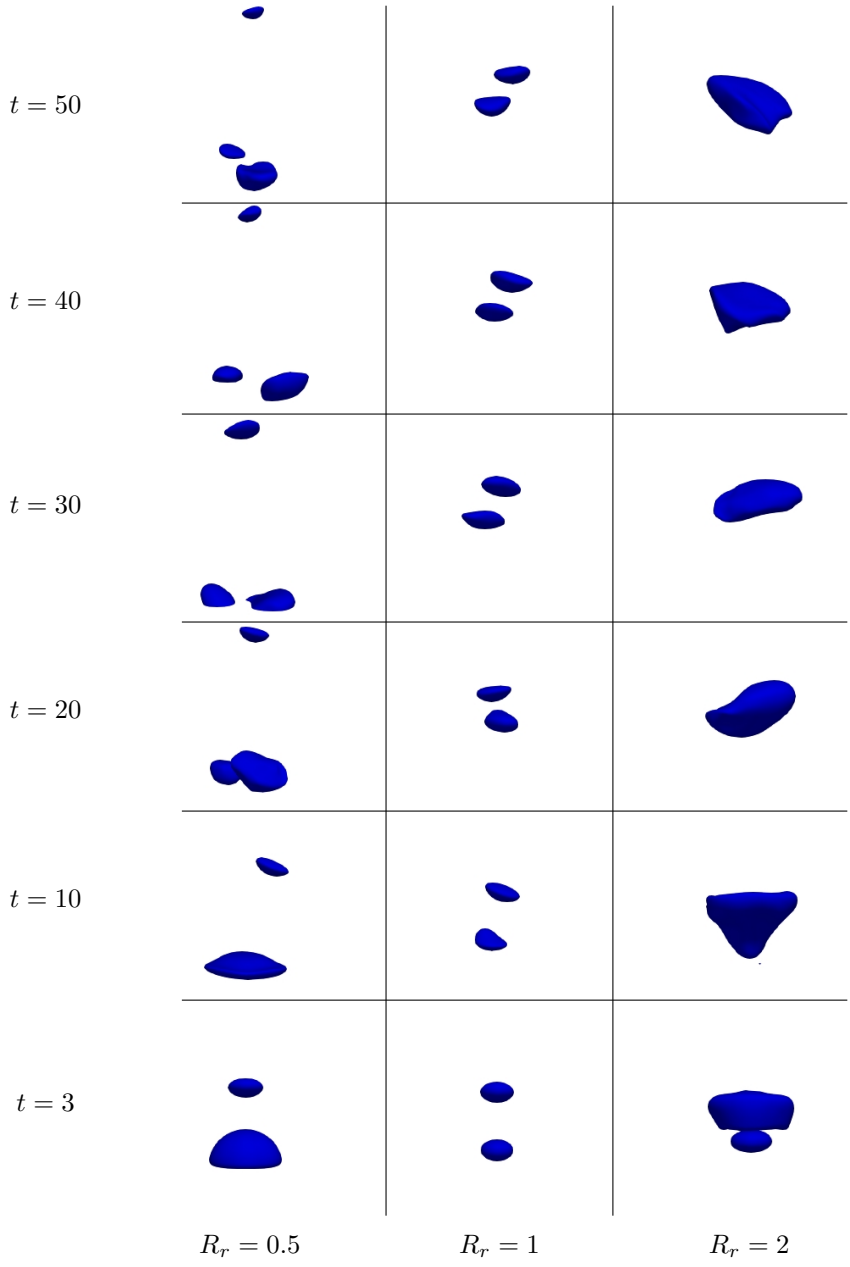

FIGURE 4.14: Shape of the bubbles rising in a non-Newtonian fluid ($n = 0.5$, $\lambda = 6$) for different R_r; regime III with (Ga,Bo)=(50,2).

Figure 4.14 illustrates the shapes of bubbles rising in a non-Newtonian fluid ($n = 0.5$, $\lambda = 6$) with three different values of R_r. For $R_r = 0.5$, TB has a large radius, causing extreme deformations and leading to a breakup at $t = 17$. After the breakup, three bubbles are formed and continue rising in a zigzag path, which corresponds to the dynamic behavior in regime III. The sheltering effect is not strong enough to cause merging at the beginning of the rising between LB and TB, and it only increases the local Ga of TB while the radius of TB increases local Bo before the breakup. The increase in the local Ga and Bo of TB leads to the breakup. After the breakup, it is observed that the bubbles rise at almost the same velocity, and the distance between LB and TB remains almost constant. When $R_r = 2$, the sheltering effect of LB is strong enough to absorb TB. At the time $t = 3$, the bubbles touch and then merge, forming a merged bubble (MB) with $Ga \approx 70$ and $Bo \approx 5$, which corresponds to regime III as shown in figure 3.2. As expected, MB continues to rise in a spiral path with extreme deformations.

The rising velocity magnitude of bubbles for different R_r is displayed in figure 4.15. The velocity magnitude exhibits an oscillatory behavior for $R_r = 0.5$ and $R_r = 1$, indicating that the bubbles rise in a zigzag path. On the other hand, the oscillations are less pronounced for $R_r = 2$, and MB rises in a spiral path with a smaller domain. The rising velocity for $R_r = 0.5$ and $R_r = 1$ is comparable, while MB for $R_r = 2$ rises slightly faster due to its larger radius, which results in a higher local Ga.

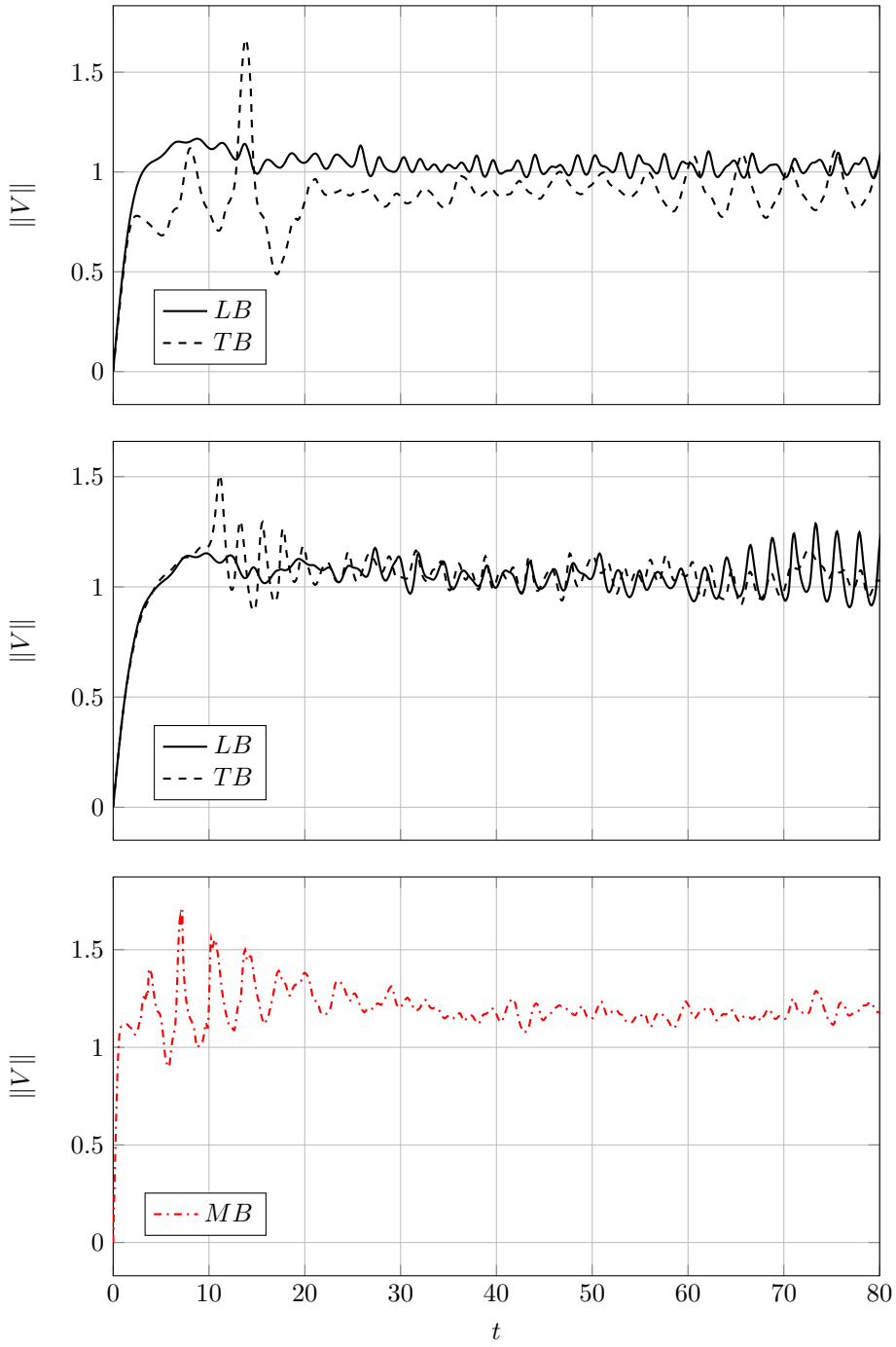

FIGURE 4.15: Rising velocity magnitude for the bubbles rising in a non-Newtonian fluid ($n = 0.5$, $\lambda = 6$) for different R_r; regime III with (Ga,Bo)=(50,2). Top: $R_r = 0.5$, middle: $R_r = 1$ and bottom: $R_r = 2$.

Figure 4.16 illustrates the surface-averaged Sherwood number for bubbles rising in the non-Newtonian fluid with varying R_r. It is observed that the time-averaged $\langle Sh \rangle$ of both LB and TB for $R_r = 0.5$ is slightly greater than that of $R_r = 1$. The difference in the surface-averaged Sherwood number for LB and TB between $R_r = 0.5$ and $R_r = 1$ can be explained by the larger surface area of the bubbles when $R_r = 0.5$,

which results in a slightly higher mass transfer rate. On the other hand, $\langle Sh \rangle$ of MB for $R_r = 2$ is almost the same as that of $R_r = 0.5$.

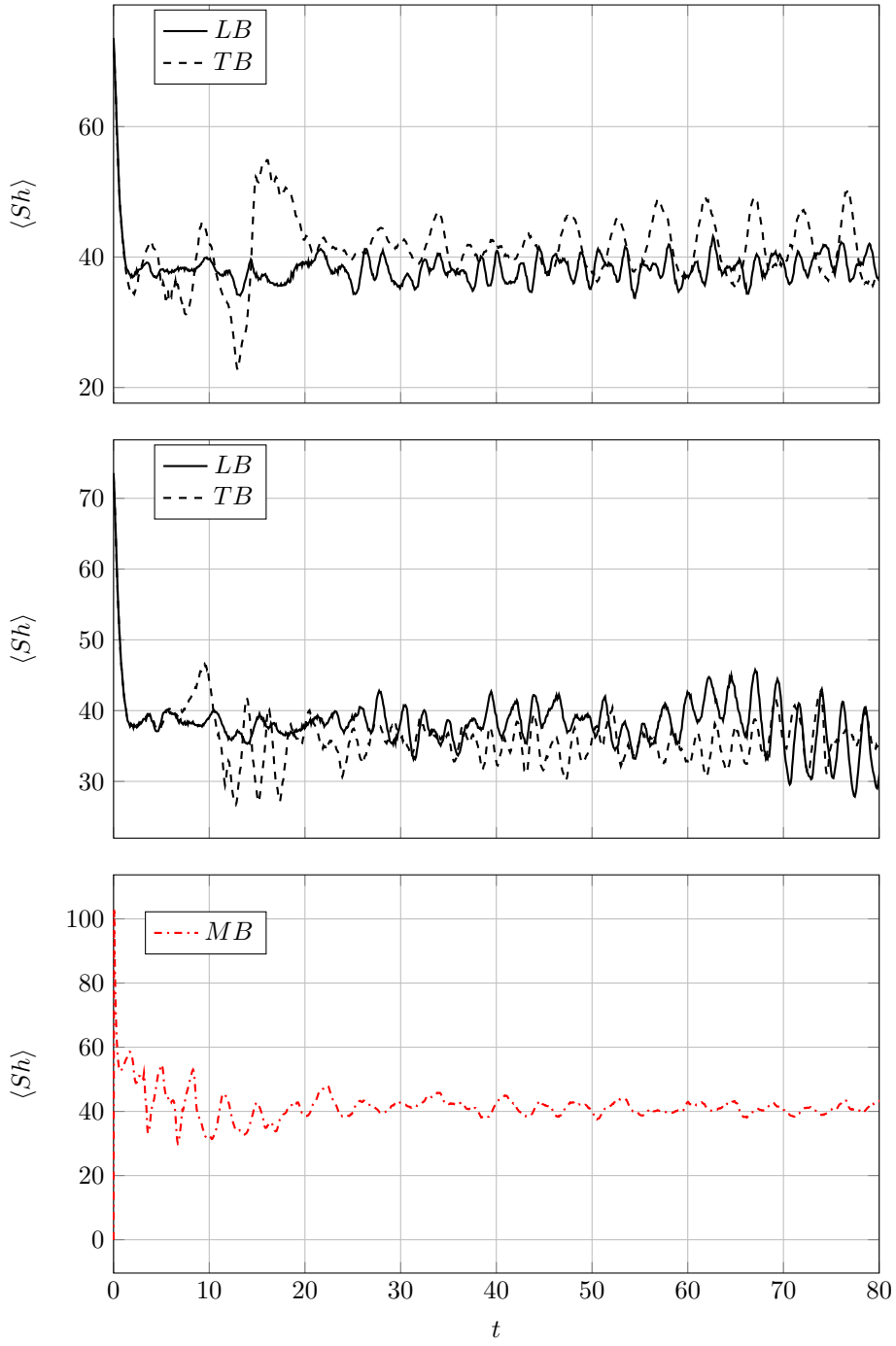

FIGURE 4.16: Surface-averaged Sherwood number for the bubbles rising in a non-Newtonian fluid ($n = 0.5$, $\lambda = 6$) for different R_r; regime III with (Ga,Bo)=(50,2). Top: $R_r = 0.5$, middle: $R_r = 1$ and bottom: $R_r = 2$.

Figure 4.17 displays the shapes of bubbles rising in a Newtonian fluid ($n = 1.0$)

for different values of R_r. When $R_r = 0.5$, the impact of the sheltering effect produced by LB is not strong enough to attract TB, and as a result, the bubbles continue to rise vertically while maintaining their original distance. Even though TB experiences some deformations, unlike in the case of $n = 0.5$, these deformations are not severe enough to cause TB to break up. This is due to the fact that in a Newtonian fluid, the local *Ga* of TB is lower than the local *Ga* of TB in a shear-thinning fluid. In the shear-thinning fluid, the viscosity decreases as the shear rate increases, which causes the local *Ga* of TB to be higher, leading to more significant deformations and possible breakup. On the other hand, in the Newtonian fluid, the viscosity remains constant, resulting in a lower local *Ga* of TB, thus reducing the chances of deformation and breakup.

When $R_r = 2$, LB creates a sheltering effect that causes the rising velocity of TB to surpass that of LB. As a result, TB makes contact with LB, and they merge to form MB, which rises vertically. In comparison to the case of $n = 0.5$, MB experiences less deformation as it rises in a Newtonian fluid due to the larger value of n, which leads to a smaller local *Ga*.

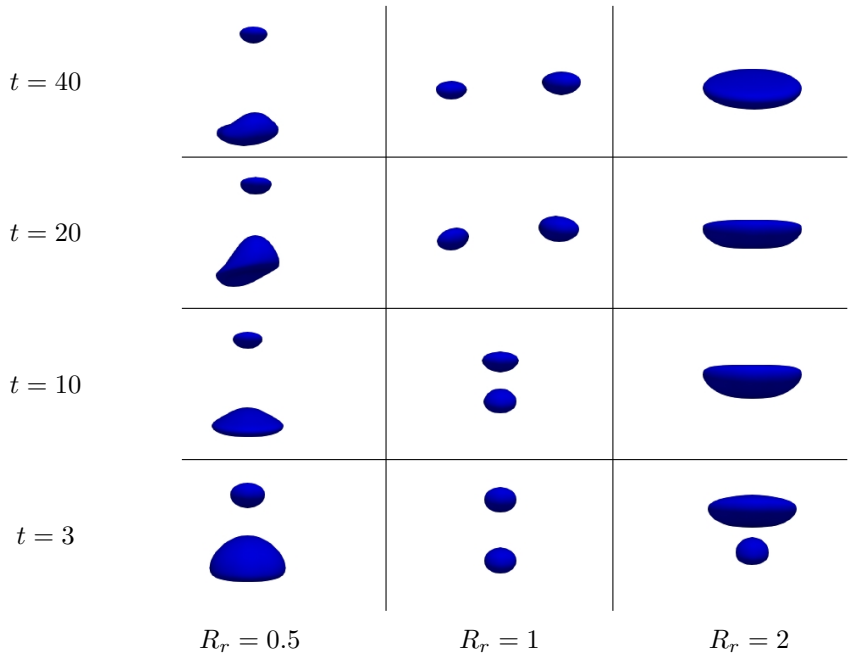

FIGURE 4.17: Shape of the bubbles rising in a Newtonian fluid ($n = 1.0$) for different R_r; regime III with (*Ga*,*Bo*)=(50,2).

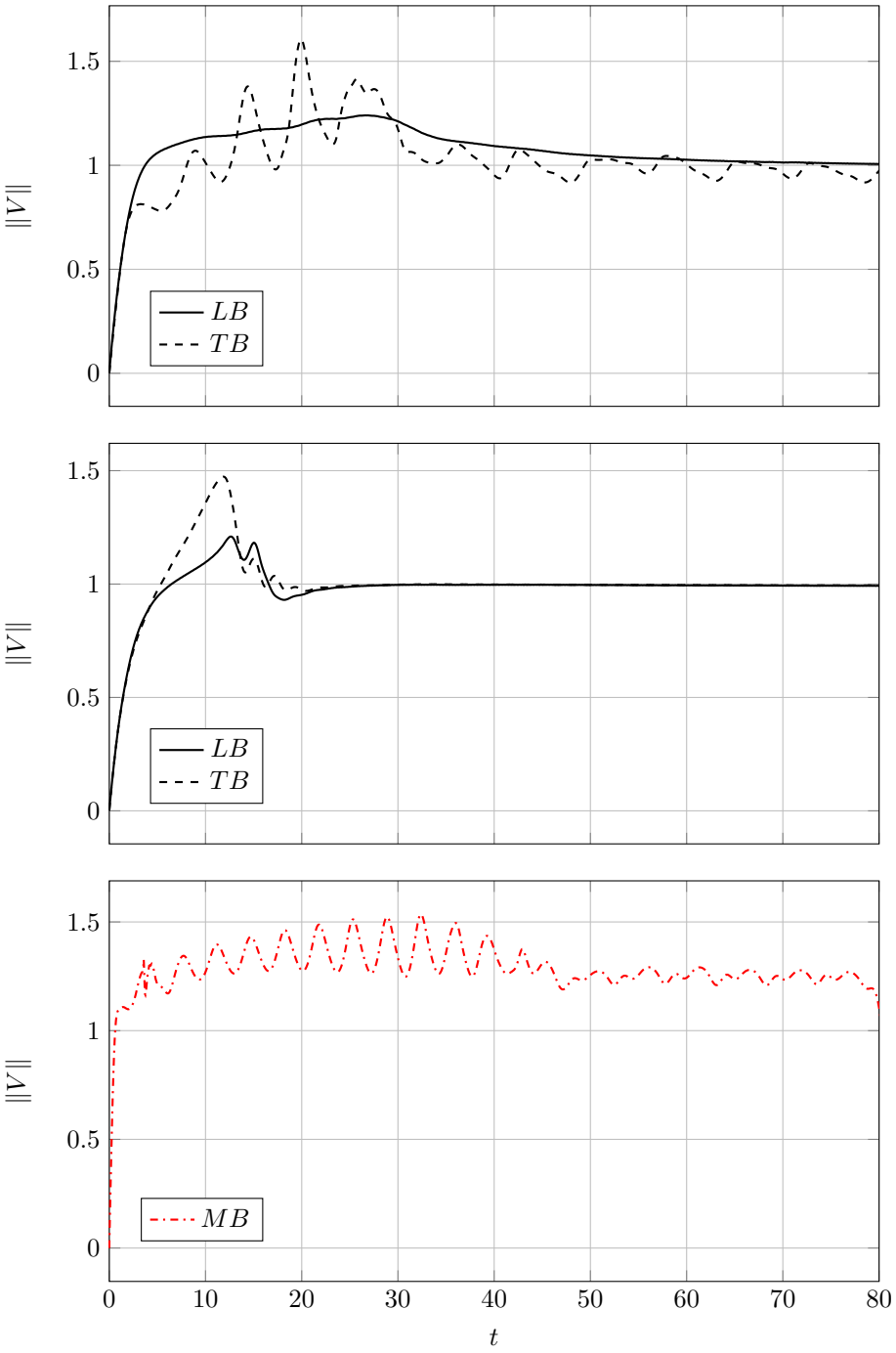

FIGURE 4.18: Rising velocity magnitude for the bubbles rising in a Newtonian fluid ($n = 1.0$) for different R_r; regime III with (Ga,Bo)=(50,2). Top: $R_r = 0.5$, middle: $R_r = 1$ and bottom: $R_r = 2$.

Figure 4.18 illustrates the changes in the magnitude of the rising velocity of bubbles for different values of R_r. Similar to the non-Newtonian case, the magnitude of the rising velocity of MB ($R_r = 2$) is greater than that of the other cases. The higher magnitude of the rising velocity of MB for $R_r = 2$ is due to the sheltering effect induced by LB, which causes TB to merge with LB, resulting in a larger bubble with a

higher rising velocity. This effect is also observed in the non-Newtonian case, where MB has the highest rising velocity magnitude. However, the oscillatory behavior observed in the non-Newtonian case is less pronounced in the Newtonian case due to the constant viscosity of the fluid.

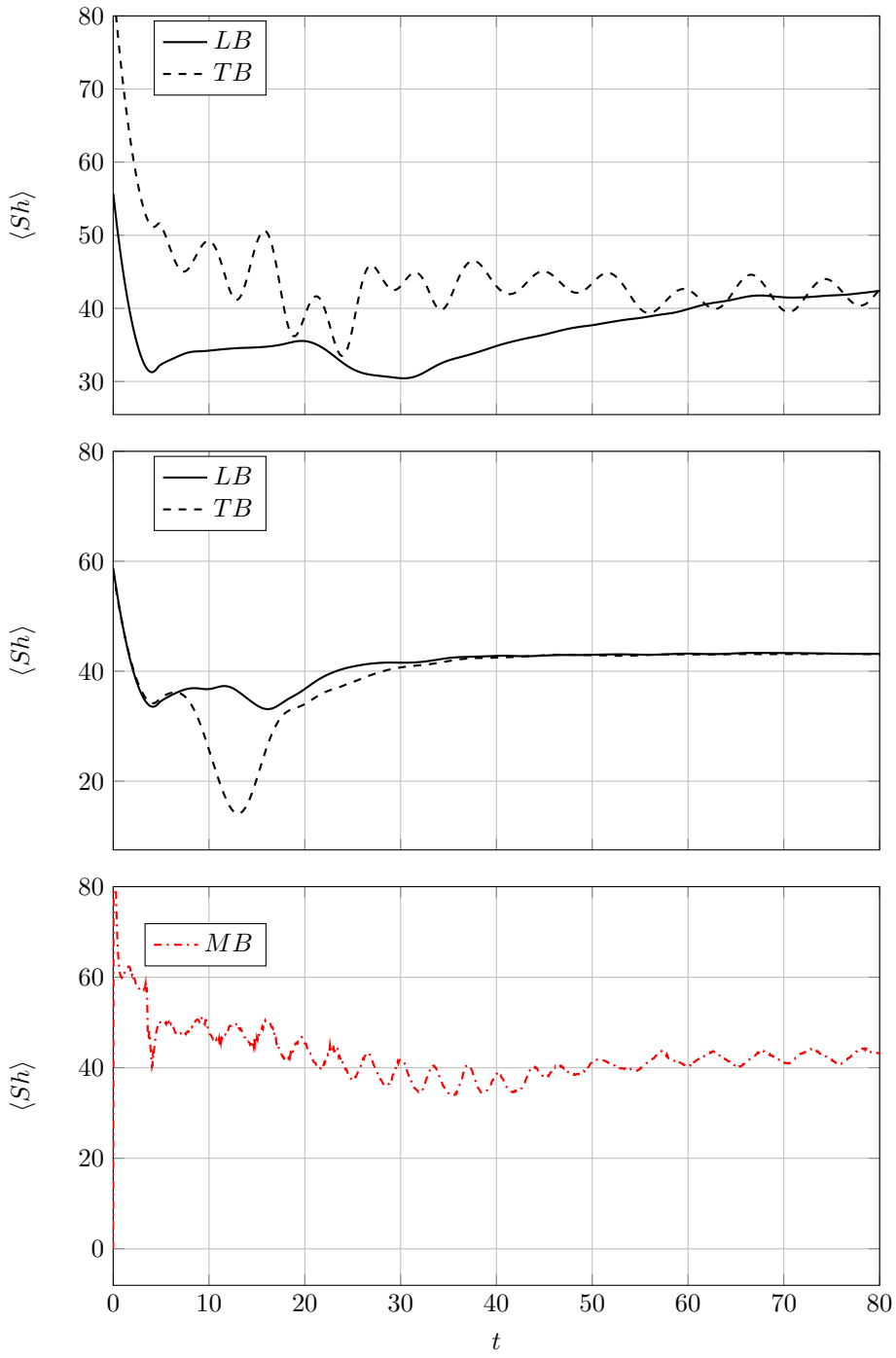

FIGURE 4.19: Surface-averaged Sherwood number for the bubbles rising in a Newtonian fluid ($n = 1.0$) for different R_r; regime III with (Ga,Bo)=(50,2). Top: $R_r = 0.5$, middle: $R_r = 1$ and bottom: $R_r = 2$.

Figure 4.19 displays the surface-averaged Sherwood number for bubbles rising in a Newtonian fluid for different values of R_r. It is notable that the surface-averaged Sherwood number is almost identical for all three R_r values. However, there is an oscillatory behavior in the $\langle Sh \rangle$ value for TB with $R_r = 0.5$ and MB with $R_r = 2$, which is due to the oscillatory dynamics behavior.

4.2.3 Effects of the inelastic time constant, λ

The inelastic time constant is a key parameter in the Carreau model, which characterizes the shear-thinning behavior of non-Newtonian fluids. This parameter represents the time scale associated with the relaxation of the fluid structure in response to applied shear stress, and it has a significant impact on the overall rheological behavior of the fluid. When the inelastic time constant is zero, the Carreau model simplifies to a Newtonian fluid, while large values of λ cause the Carreau model to reduce to a power-law model, which describes a fluid that exhibits a more significant degree of shear-thinning (*35*, *80*). Therefore, understanding the value of the inelastic time constant is critical for predicting the behavior of non-Newtonian fluids in a variety of industrial and environmental applications, including the processing of complex fluids, such as food products or biomedical materials.

In this section, to analyze the dynamics of bubbles and mass transfer rate, two different (Ga, Bo) sets are studied, namely (30, 25) and (50, 2) corresponding to regimes II and III in the $Ga - Bo$ phase plot, respectively. The study is carried out with four different values of λ (0, 3, 6, and 9), where 0 represents a Newtonian fluid.

Regime II

Figure 4.20 shows the evolution of the shape of the bubbles for different values of λ. As λ increases, the fluid becomes more shear-thinning, which causes the bubbles to coalesce sooner. For $\lambda = 0$, the bubbles merge at $t = 6.65$ and the merged bubble (MB) rises vertically. At $t = 8$, there is a small peripheral breakup, resulting in the formation of small satellites. For $\lambda = 3$, the bubbles merge at $t = 5.2$ and MB rises vertically. Then, breakup happens at $t = 8.39$, and MB is divided into two smaller bubbles, B1 and B2 which rise almost vertically. There are also a few small satellites. For $\lambda = 6$, the bubbles merge at $t = 5.15$, leading to the formation of MB. Then,

breakup happens at $t = 8.75$, and MB is divided into three smaller bubbles, B1, B2, and B3, which rise almost vertically. A few small satellite bubbles are also present. For $\lambda = 9$, the bubbles merge at $t = 5.1$, and MB is formed. Then, breakup happens at $t = 8.8$, and MB is divided into three smaller bubbles, B1, B2, and B3, which rise almost vertically. There are also a few small satellite bubbles present. The increase in shear thinning, as λ increases, leads to a higher rising velocity of bubbles, as well as more instability during their rise. This is because the shear-thinning property of the fluid reduces its resistance to deformation, making it easier for the bubbles to merge and breakup. As a result, bubbles coalesce sooner and smaller bubbles are formed during the breakup, leading to a more unstable flow. The presence of small satellites also indicates the presence of unstable regions within the flow, which can further enhance the mixing of the fluid.

The increasing shear-thinning behavior of the fluid with higher λ leads to more instability and oscillations during the bubble rise. This is due to the fact that a higher shear rate around the bubble causes more deformation and stretching of the bubble, which in turn leads to more breakup events and the formation of smaller satellite bubbles. Additionally, the interaction between the bubble and the shear-thinning fluid induces complex flow patterns around the bubble, which can cause instabilities and oscillations in the shape and trajectory of the bubble. Therefore, increasing λ can lead to more complex dynamics of the bubble rise with more instability and oscillatory behavior.

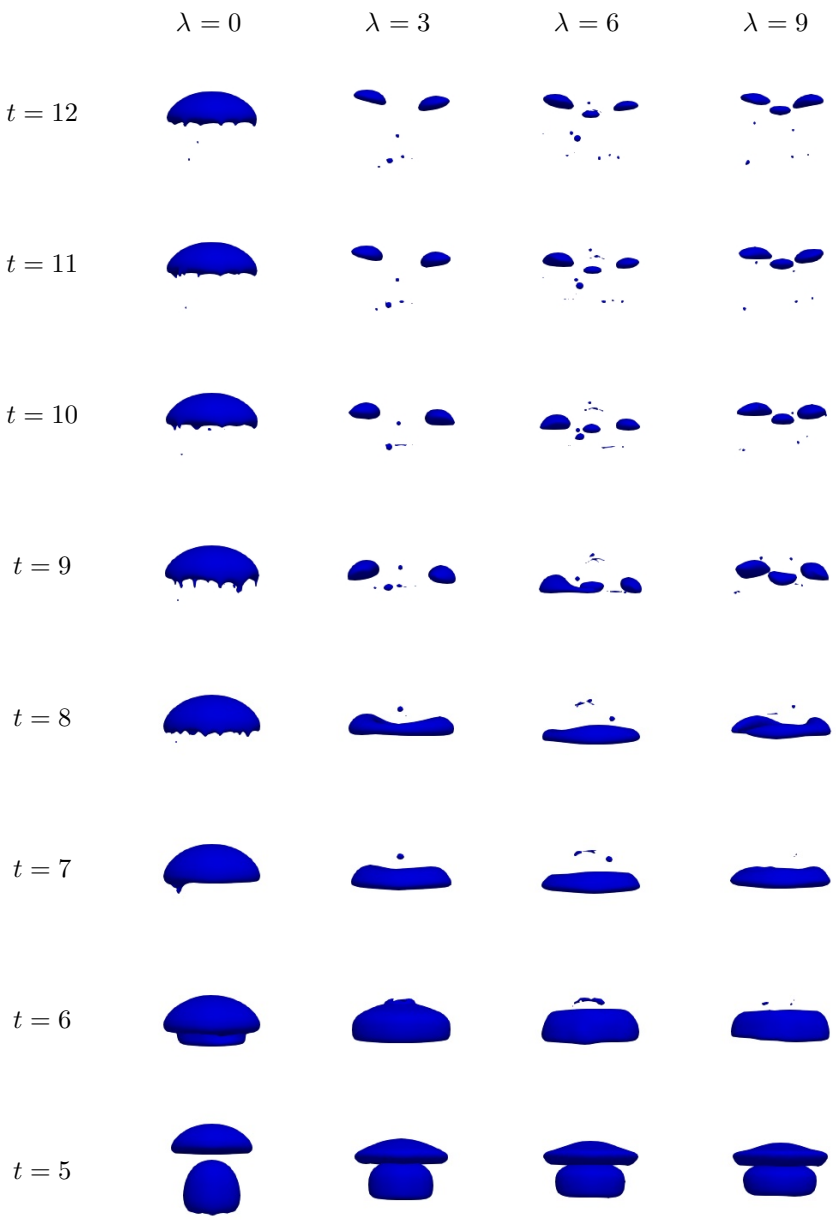

FIGURE 4.20: Shape of the bubbles for different values of λ at different times; regime II with (Ga,Bo)=(30,25).

Figure 4.21 illustrates how the volume-averaged rising velocity magnitude of bubbles changes over time for different values of λ. As λ increases, both the magnitude and oscillatory nature of the plot become more pronounced. The oscillatory behavior of the rising velocity magnitude plot increases as λ increases because a higher value of λ indicates a more shear-thinning fluid. Shear-thinning fluids exhibit a non-linear relationship between the shear rate and the shear stress, which means that as the shear rate increases, the viscosity of the fluid decreases. This can

result in more complex and unstable flow patterns, which in turn can cause the bubbles to experience more erratic and oscillatory motion as they rise through the fluid. Additionally, as the fluid becomes more shear-thinning, the bubbles are more likely to coalesce sooner, which can also contribute to the increased oscillatory behavior of the rising velocity magnitude plot.

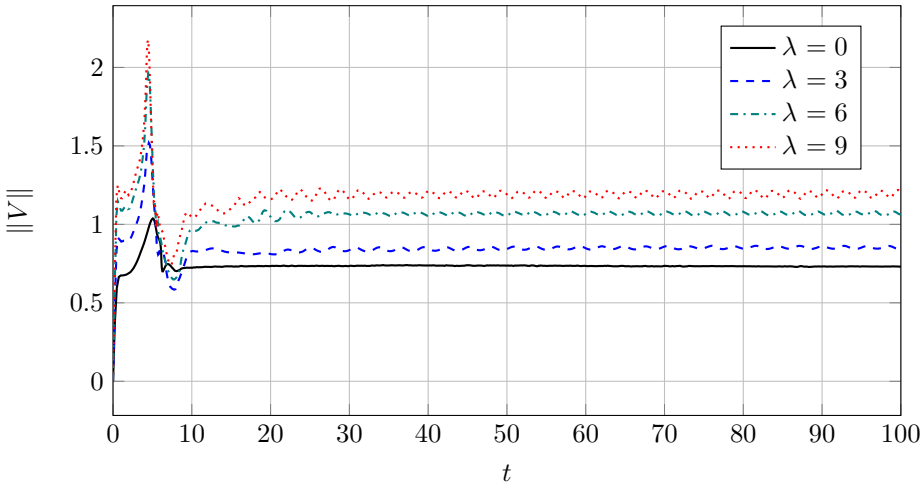

FIGURE 4.21: Volume-averaged rising velocity magnitude of the bubbles versus time for different values of λ; regime II with (Ga,Bo)=(30,25).

Figure 4.22 illustrates the changes in the evolution of $\langle Sh \rangle$ for different values of λ. Initially, a larger value of λ results in a higher $\langle Sh \rangle$. However, over time, the effect of λ on $\langle Sh \rangle$ diminishes, and its impact becomes negligible. At the beginning of the simulation, the effect of fluid rheology on the shear rate around the bubbles is more prominent, leading to larger values of $\langle Sh \rangle$ for higher λ. However, as the simulation progresses, the effect of the bubble behavior becomes more significant, causing the magnitude of $\langle Sh \rangle$ to converge to a relatively constant value, regardless of the value of λ.

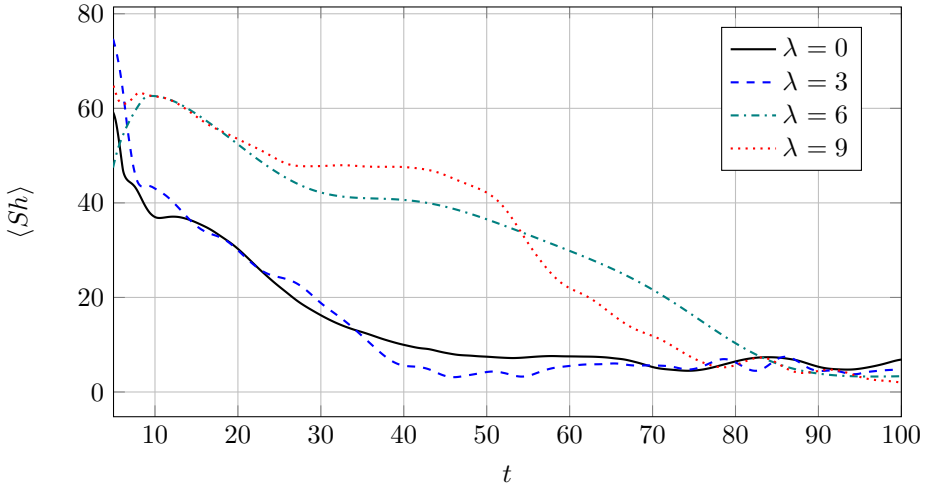

FIGURE 4.22: Surface-averaged Sherwood number versus time for different values of λ; regime II with (Ga,Bo)=(30,25).

Regime III

Figure 4.23 shows the evolution of the shape of the bubbles for different values of λ. For $\lambda = 0$, the dynamics follow the DKT scenario, with the bubbles rising vertically and side-by-side after the initial transient period. For $\lambda = 3$, 6, and 9, all three cases follow the side escape scenario, where the bubbles escape the wake of the leading bubble and rise in a zigzag path.

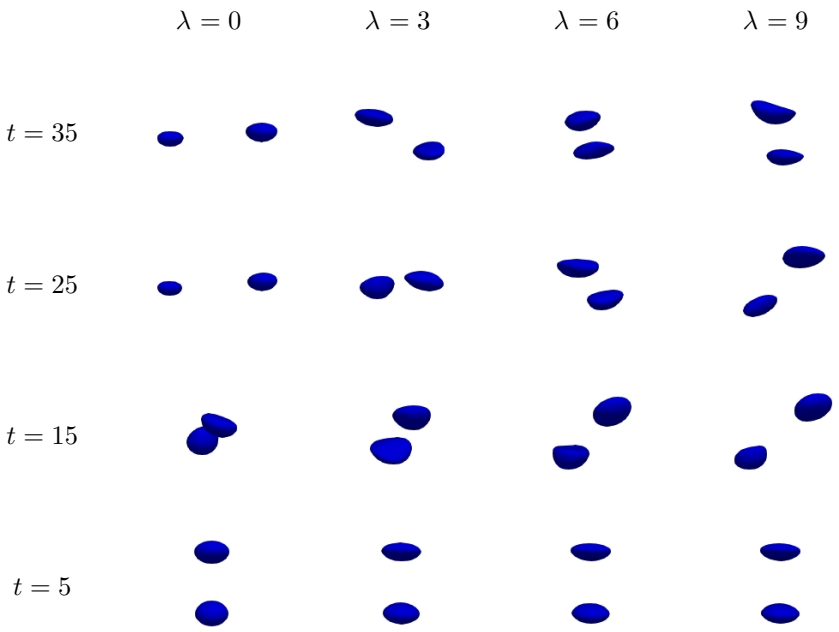

FIGURE 4.23: Shape of the bubbles for different values of λ at different times; regime III with (Ga,Bo)=(50,2).

The distance between the bubbles is illustrated in figure 4.24. It is observed that as λ increases, the oscillatory behavior of the bubbles becomes more intense. As the fluid becomes more shear-thinning with increasing λ, the bubbles experience more deformation and oscillations, which result in a more intense zigzag path and greater oscillation amplitude. This, in turn, affects the distance between bubbles, causing it to fluctuate more for higher values of λ.

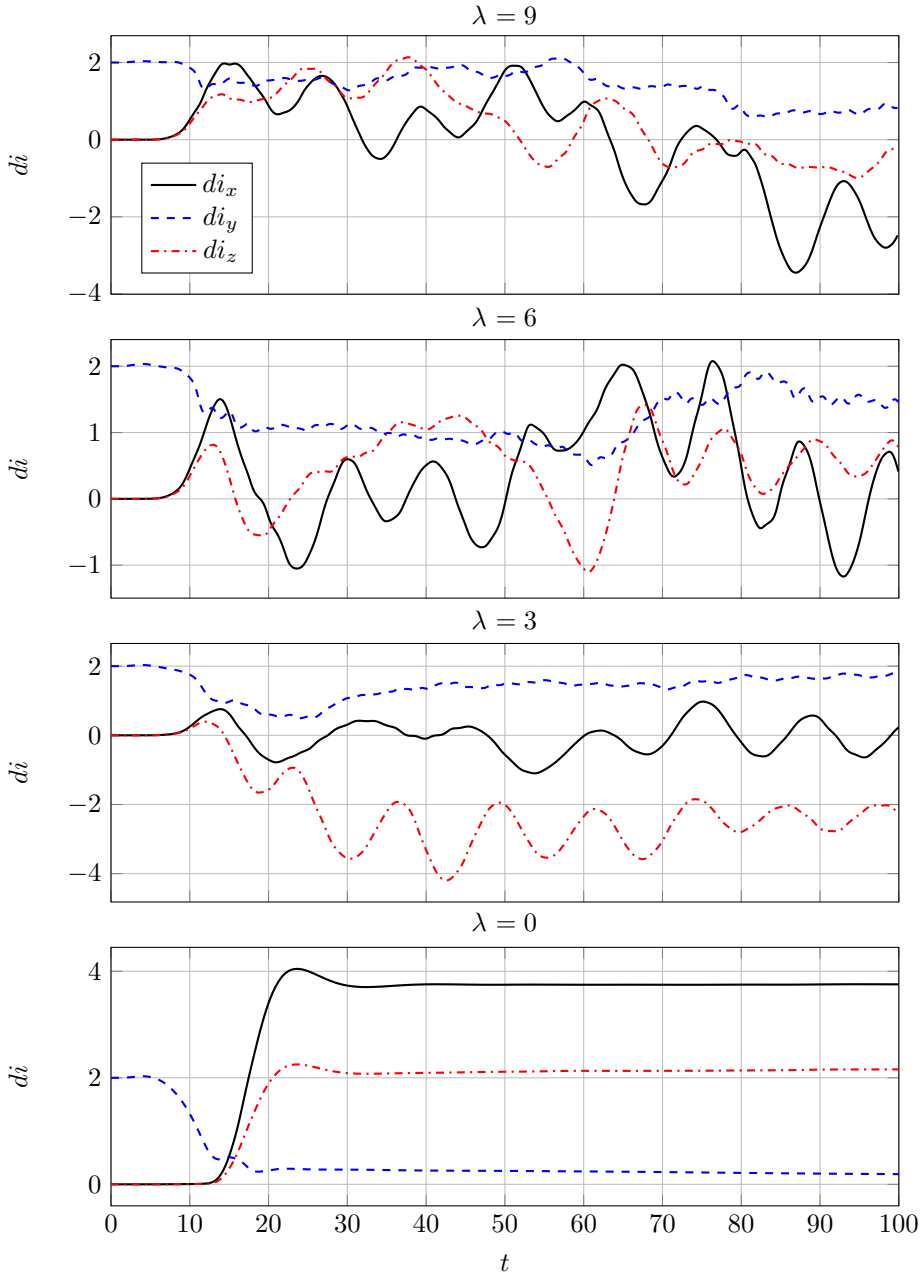

FIGURE 4.24: Instantaneous distance between the bubbles versus time for different values of λ; regime III with (Ga,Bo)=(50,2).

This behavior is also reflected in the rising velocity magnitude, as shown in figure 4.25. It can be seen that by increasing λ, the bubbles rise more irregularly due to the increased shear-thinning behavior of the fluid, resulting in a more oscillatory velocity profile. Although the oscillatory behavior of the rising velocity increases by increasing λ, with more intense fluctuations, it can be observed that the magnitude of the rising velocity fluctuates around a constant value for all three cases. This constant value is nearly equal to the magnitude of the rising velocity of the bubbles for λ=0.

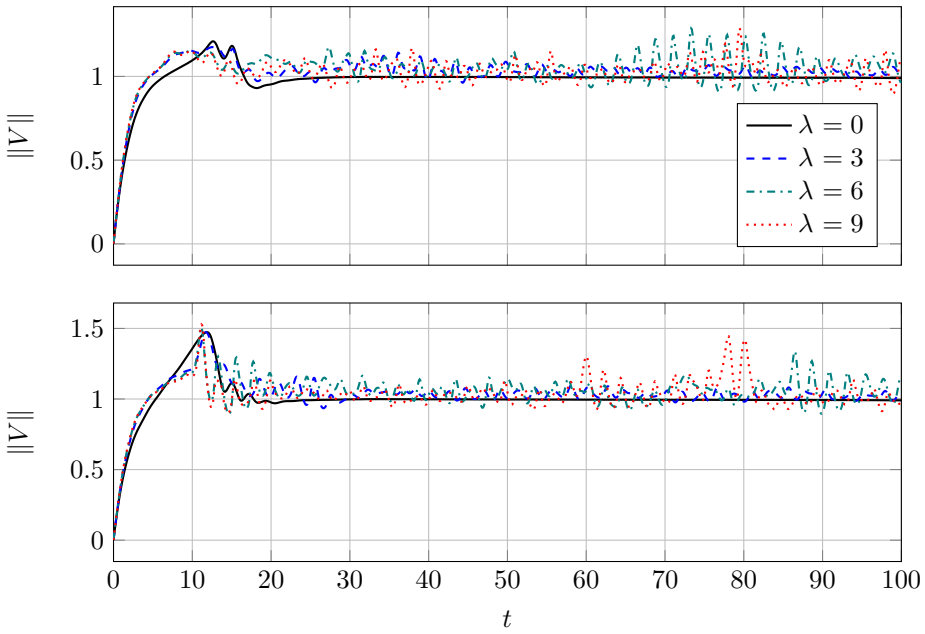

FIGURE 4.25: Rising velocity magnitude of the bubbles versus time for different values of λ; regime III with (Ga,Bo)=(50,2). Top: LB, and bottom: TB.

Fig. 4.26 illustrates that the trend in the evolution of $\langle Sh \rangle$ is comparable to that of the rising velocity magnitude shown in the previous figure. As λ increases, fluctuations in $\langle Sh \rangle$ become more pronounced. Moreover, for all three cases where $\lambda > 0$, $\langle Sh \rangle$ oscillates around a relatively constant value that is slightly lower than the corresponding value for the $\lambda = 0$ case.

The main frequency of the surface-averaged Sherwood number and velocity magnitude versus time can be obtained by performing a fast Fourier transform (FFT). For the cases with λ=3, 6, and 9, the main frequency is found to be 0.4, 0.44, and 0.48, respectively. The main frequency of the surface-averaged Sherwood number and velocity magnitude increases by increasing λ because the increasing value of λ

leads to more intense oscillations of the bubbles. These oscillations lead to a more complex and faster-changing flow field around the bubbles, which results in higher frequency fluctuations in the Sherwood number and velocity magnitude. This helps us understand how the bubble behavior changes as a function of λ. Specifically, the fact that the main frequency increases with increasing λ suggests that the bubbles exhibit more intense and rapid oscillatory behavior at higher values of λ.

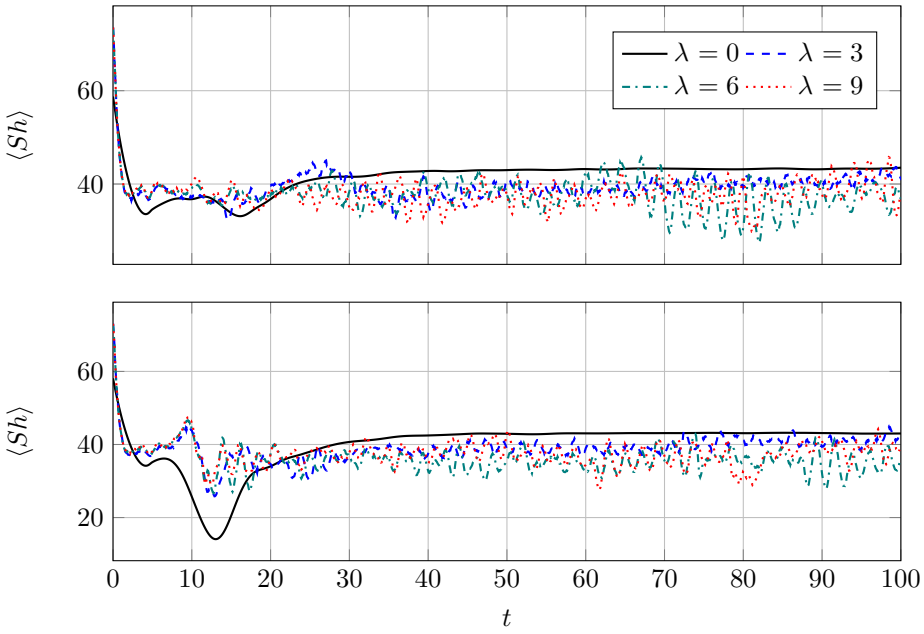

FIGURE 4.26: Surface-averaged Sherwood number versus time for different values of λ; regime III with (Ga,Bo)=(50,2). Top: LB, and bottom: TB.

4.2.4 Effects of the flow index, n

The flow index is an important rheological parameter that characterizes the shear-thinning behavior of non-Newtonian fluids. It is defined as the slope of the logarithm of shear stress versus shear rate and can be used to quantify the extent to which a fluid's viscosity decreases with increasing shear rate. As the flow index decreases, the degree of shear-thinning behavior becomes more pronounced, and the fluid's viscosity decreases at a faster rate with an increasing shear rate. This behavior is in contrast to Newtonian fluids, which have a constant viscosity that is independent of shear rate.

The flow index plays a crucial role in many industrial and environmental applications, such as the design and operation of mixing and pumping systems, oil

recovery, food processing, and wastewater treatment. In these applications, the degree of shear-thinning behavior of the fluid can significantly affect the overall system performance and efficiency (*99*, *100*). Therefore, understanding the effects of the flow index on the behavior of bubbles rising in non-Newtonian fluids is essential for optimizing the performance of multiphase systems in various applications.

To examine the impact of the flow index, this section utilized Bubble25 parameters from Cano-Lozano and Mart'ınez-Baz'an (*96*), specifically $Ga = 88.74$ and $Bo = 8.5$ in regime III. The study then explored the effects of varying flow indexes, namely 0.3, 0.5, 0.7, and 1.0, with λ fixed at 6.

The behavior of the bubbles rising in different fluids with different values of n can provide important insights into the physical properties of the fluids and their effects on fluid flow dynamics. As shown in figure 4.27, the shape of the bubbles changes significantly with changes in the value of n. For non-Newtonian fluids with $n < 1$, the bubbles rise in a zigzag path, indicating the presence of shear-thinning and viscoelastic effects that cause significant deformation of the bubbles. As n increases in non-Newtonian fluids (n =0.3, 0.5, and 0.7), the domain of the zigzag path decreases. The reason for this behavior can be attributed to the viscosity of the fluid. Non-Newtonian fluids exhibit complex rheological behavior, which means that their viscosity changes as the shear rate changes. As the bubbles rise in such fluids, they generate a flow field that changes the local shear rate, leading to a complex and erratic bubble motion. Therefore, the domain of the zigzag path increases by decreasing n, indicating a stronger effect of the fluid's rheology on the bubble's trajectory. In contrast, for Newtonian fluids with $n = 1$, the bubbles initially rise in a zigzag path, but then the domain of the zigzag path decreases as the bubbles rise, eventually transitioning to a vertical path. This behavior can be explained by the fact that the vertical path has the lowest drag coefficient, and the bubbles try to adopt this path to minimize the drag force acting on them.

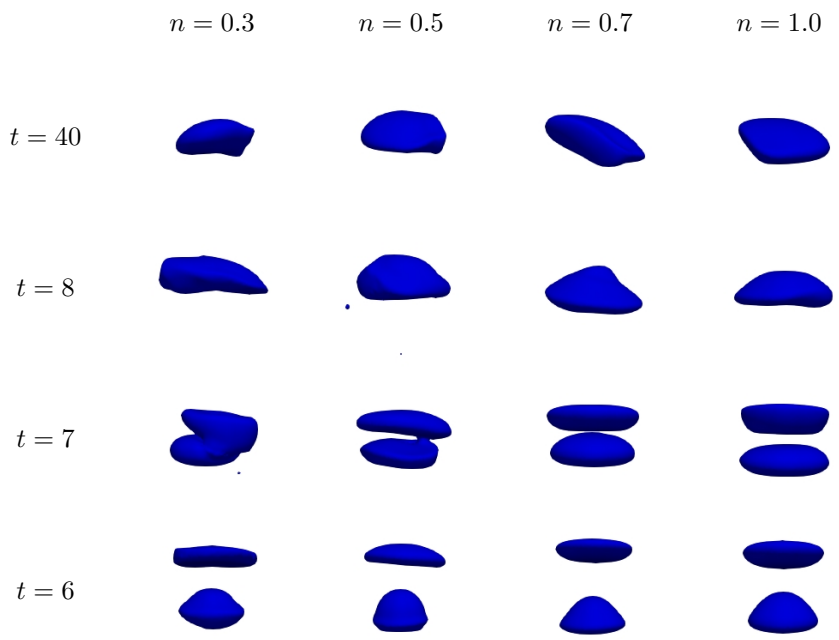

FIGURE 4.27: Shape of the bubbles for different values of n with $\lambda = 6$ at different times; regime III with (Ga,Bo)=(88.74,8.5).

The evolution of rising velocity magnitude shown in figure 4.28 also indicates that the bubbles in the Newtonian fluid ($n = 1$) initially rise with a fluctuating velocity, but then the fluctuations dampen as the bubbles rise and eventually the velocity becomes almost constant. This is because the effect of the fluid viscosity dominates over other fluid effects, such as shear-thinning or shear-thickening, as the bubbles rise. In contrast, the bubbles in the non-Newtonian fluids ($n = 0.3$, 0.5, and 0.7) continue to exhibit oscillatory behavior in their rising velocity magnitude, indicating the continued influence of non-Newtonian effects on the bubbles' trajectory.

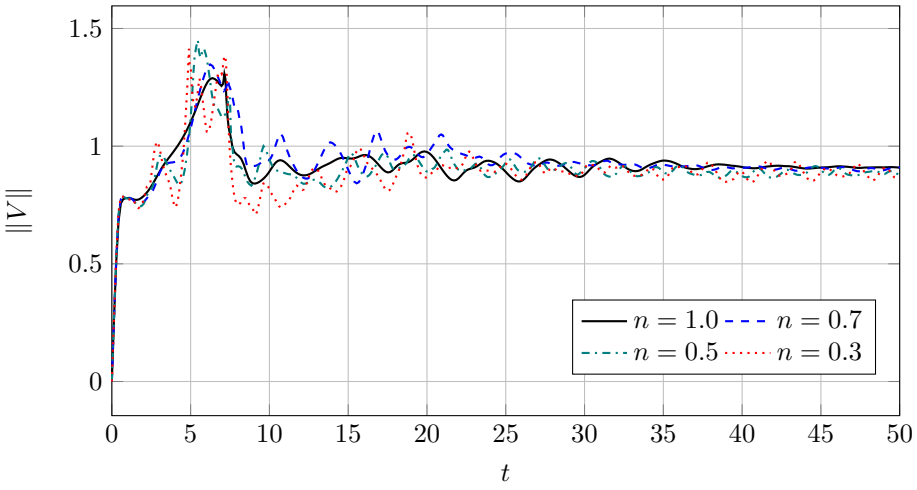

FIGURE 4.28: Rising velocity magnitude of the bubbles versus time for different values of n with $\lambda = 6$; regime III with (Ga,Bo)=(88.74,8.5).

Figure 4.29 illustrates the change in the time evolution of $\langle Sh \rangle$ for MB as it rises in fluids with varying values of n. The final value of $\langle Sh \rangle$ is observed to increase with decreasing n. The Sherwood number $\langle Sh \rangle$ is a measure of the efficiency of mass transfer from the fluid to the surface of the bubble. The final value of $\langle Sh \rangle$ increases by decreasing n because the non-Newtonian fluids with lower n exhibit a higher level of mixing and chaotic motion, which enhances the mass transfer between the fluid and the bubble surface. In contrast, in the Newtonian fluid with $n = 1$, the fluid motion is more regular and laminar, resulting in a lower mass transfer rate and lower $\langle Sh \rangle$.

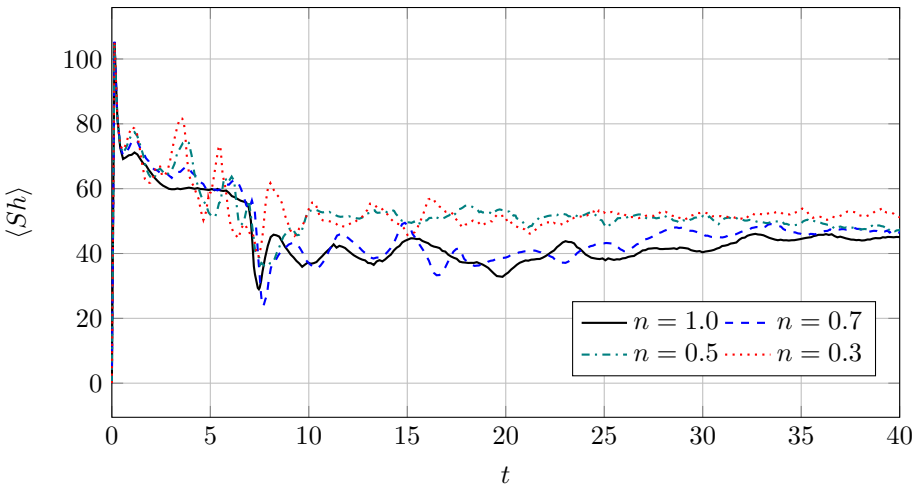

FIGURE 4.29: Surface-averaged Sherwood number versus time for different values of n with $\lambda = 6$; regime III with (Ga,Bo)=(88.74,8.5).

In general, bubbles rising in Newtonian fluids behave differently than bubbles rising in non-Newtonian fluids. Newtonian fluids have a constant viscosity regardless of the shear rate or stress applied to them, while non-Newtonian fluids have a viscosity that changes with the applied shear rate or stress. This means that the behavior of bubbles rising in non-Newtonian fluids can be influenced by the fluid's rheological properties, such as its viscosity, elasticity, and shear-thinning behavior. Non-Newtonian fluids can cause bubbles to deform or break up more easily, or to rise in a zigzag or spiral path due to variations in viscosity or shear rate. In contrast, bubbles rising in Newtonian fluids tend to behave in a more predictable manner and experience less deformation or disruption during their ascent.

UNIVERSITAT ROVIRA I VIRGILI,
NUMERICAL INVESTIGATION OF A SINGLE BUBBLE AND A PAIR OF BUBBLES RISING IN NEWTONIAN AND NON NEWTONIAN FLUIDS WITH INTERFACIAL PASSIVE SCALAR TRANSFER
Koorosh Kazemi

Chapter 5

Conclusions

This thesis consists of two main parts. The first part involves a numerical investigation of a single gas bubble rising in different types of fluids, including Newtonian fluid with a flow index of 1.0, shear-thinning fluids with flow indices of 0.3 and 0.6, and shear-thickening fluid with a flow index of 1.7. The simulation is conducted with a constant set of parameters, including the Galilei number (Ga) and the Bond number (Bo), both equal to 30 and 2, respectively. The study also considers the transfer of a scalar across the bubble interface and analyzes the effects of the Peclet number (Pe), which is varied from 10 to 1000. The second part of the thesis involves the investigation of a pair of bubbles rising in-line in two types of fluids: Newtonian fluid with a flow index of 1.0 and shear-thinning fluid with a flow index of 0.5. The study includes an analysis of heat and mass transfer and considers the effects of several parameters, including Ga, Bo, R_r, λ, and n. The numerical simulation is carried out using *Basilisk* which employs adaptive mesh refinement techniques that are dependent on the velocity magnitude, passive scalar value, and the position of the interface.

The results for a single bubble showed that the behavior of the bubble rising dynamics strongly depends on the flow index of the ambient fluid. Shear-thinning fluids lead to an oscillatory motion of the bubble while shear-thickening fluids cause the bubble to rise along the vertical axis with less deformation. Furthermore, the results indicated that the mass transfer across the bubble interface is strongly influenced by both the flow index and Peclet number. In general, an increase in the Peclet number leads to an increase in the mass transfer rate, while an increase in the flow index results in a decrease in the mass transfer rate. Additionally, it is found that the

oscillatory behavior of the bubble in the shear-thinning fluid results in fluctuations in the mass transfer rate, whereas the mass transfer rate remains relatively constant in the other fluids. The results of the simulation also revealed that in the case of the shear-thickening fluid, the rising velocity is relatively low, and the shape of the bubble does not deform. However, as the flow index decreases, the rising velocity and the deformation of the bubble increase. On the other hand, for the shear-thinning fluids, the surface-averaged Sherwood number exhibits an oscillatory behavior over time due to the oscillatory behavior of the rising velocity magnitude. Finally, a correlation between the surface-averaged Sherwood number and the Peclet number and flow index is proposed in this section. These findings provide important insights into the behavior of the gas bubble in different types of fluids and have implications for a range of industrial processes.

The results presented for a pair of bubbles demonstrated the profound impact that a second bubble can have on the flow dynamics of a rising bubble pair, particularly in the presence of non-Newtonian rheologies. The time evolution of the distance and rising velocity of the bubbles are affected by the wake sheltering, transverse flow disturbances, and bubble interface deformations, ultimately leading to different flow regimes and configurations. Several motion patterns characterizing the behavior of two bubbles, such as side escape, Drafting-Kissing-Tumbling (DKT), and coalescence are described, and a new scenario is defined as coalescence-breakup. The study considered five different sets of (Ga, Bo) values that correspond to five different regimes, highlighting the interplay between these numbers and the dynamic behavior of bubbles in different fluid media as well as the effects of these numbers on the heat/mass transfer rate. The results showed that heat/mass transfer is optimized in regimes I and III where the bubbles follow the side escape scenario or DKT scenario. In contrast, regimes in which the bubbles follow coalescence or CB patterns show a lower rate of heat/mass transfer. The results also indicated that the radius ratio of the leading bubble to the trailing bubble plays a significant role in the behavior of bubbles rising, leading to deformations, breakup, or merging although its effect on the heat/mass transfer rate is not remarkable. Moreover, the results showed that in regime II, the behavior of bubbles rising in shear-thinning fluids is significantly influenced by the value of λ. As λ increases, the fluid becomes

more shear-thinning, leading to earlier coalescence and breakup of bubbles, and the formation of smaller satellite bubbles. This causes more instability and oscillatory motion during the bubble rise. However, the effect of λ on the final value of $\langle Sh \rangle$ is found to be negligible. Additionally, results revealed that the increasing value of the shear-thinning index λ leads to more intense deformation and oscillations of bubbles, causing a more irregular and zigzag path of the bubbles in regime III. The distance between bubbles becomes more fluctuating and the main frequency of the Sherwood number and velocity magnitude increases with increasing λ, indicating more intense and rapid oscillatory behavior of bubbles. Finally, results showed that the flow index is a significant rheological parameter that affects the behavior of the bubbles. The shape of the bubbles changes significantly with changes in the value of n, with non-Newtonian fluids exhibiting a zigzag path due to the presence of shear-thinning and viscoelastic effects that cause significant deformation of the bubbles. It was also observed that the final value of $\langle Sh \rangle$ increases with decreasing n due to the higher level of mixing and chaotic motion, enhancing the mass transfer between the fluid and the bubble surface. These findings suggest that the interaction between bubbles is a crucial factor in the study of multiphase flows, highlighting the need for further investigation into the complex dynamics of bubble pairs and their impact on larger-scale systems.

Overall, this study provides a better understanding of the effects of rheological properties on the dynamics of the bubbles in fluids, which is essential in various industrial and environmental applications, such as wastewater treatment, chemical processing, and oil recovery.

The behavior of bubbles in fluids is a multifaceted phenomenon that is influenced by numerous factors including fluid properties, bubble characteristics (size, shape, and motion), and operational parameters such as pressure, temperature, and flow rate. As a result, the investigation of bubble behavior in non-Newtonian fluids is an intricate and continuous research area with a significant impact on heat and mass transfer rates and overall system functionality. Consequently, the following areas can be proposed as potential avenues for future research based on the findings and limitations of the current study:

- Investigate the effect of different bubble sizes and shapes on the mass transfer and bubble dynamics in different rheological fluids.
- Consider more complex non-Newtonian fluids, such as yield stress fluids or thixotropic fluids, and investigate their effect on the bubble dynamics and mass transfer.
- Incorporate heat transfer effects into the current study and investigate the combined effect of heat and mass transfer in non-Newtonian fluids.
- Study the effect of boundary conditions, such as the presence of walls or confinement, on the bubble dynamics and mass transfer in non-Newtonian fluids.

References

(*1*) Deike, L. (2022). Mass Transfer at the Ocean–Atmosphere Interface: The Role of Wave Breaking, Droplets, and Bubbles. *Annual Review of Fluid Mechanics 54*, 191–224.

(*2*) Wang, S., Gui, Q., Zhang, J., Gao, Y., Xu, J., and Jia, X. (2021). Theoretical and experimental study of bubble dynamics in underwater explosions. *Physics of Fluids 33*, 126113.

(*3*) Yasui, K., Tuziuti, T., and Kanematsu, W. (2019). High temperature and pressure inside a dissolving oxygen nanobubble. *Ultrasonics Sonochemistry 55*, 308–312.

(*4*) Wang, T., Wang, J., and Jin, Y. (2007). Slurry Reactors for Gas-to-Liquid Processes: A Review. *Industrial and Engineering Chemistry Research 46*, 5824–5847.

(*5*) Al-Baroudi, H., Klein, A. C., and Pauley, K. A. (1991). Experimental simulation of the bubble membrane radiator using a rotating flat plate. *AIP Conference Proceedings 217*, 723–727.

(*6*) Haas, T., Schubert, C., Eickhoff, M., and Pfeifer, H. (2021). A Review of Bubble Dynamics in Liquid Metals. *Metals 11*.

(*7*) Plesset, M. S. (1949). The Dynamics of Cavitation Bubbles. *Journal of Applied Mechanics 16*, 277–282.

(*8*) Lü, M., Ning, Z., Yan, K., Fu, J., and Sun, C. (2016). Temporal and spatial stability of liquid jet containing cavitation bubbles in coaxial swirling compressible flow. *Meccanica 51*, 2121–2133.

(*9*) Wu, Z.-W., Zhao, H., Li, W.-F., Xu, J.-L., Wang, S., and Liu, H.-F. (2019). Effects of inner bubble on liquid jet breakup. *Physics of Fluids 31*, 034107.

(*10*) Guo, L.-M., Lü, M., and Ning, Z. (2021). Stability of a Viscous Liquid Jet in a Coaxial Twisting Compressible Airflow. *Processes 9*.

(*11*) Anna, S. L. (2016). Droplets and Bubbles in Microfluidic Devices. *Annual Review of Fluid Mechanics 48*, 285–309.

(*12*) Kantarci, N., Borak, F., and Ulgen, K. O. (2005). Bubble column reactors. *Process Biochemistry 40*, 2263–2283.

(*13*) Mavroudi, M., Kaldis, S., and Sakellaropoulos, G. (2006). A study of mass transfer resistance in membrane gas–liquid contacting processes. *Journal of Membrane Science 272*, 103–115.

(*14*) Sakr, M., Mohamed, M. M., Maraqa, M. A., Hamouda, M. A., Aly Hassan, A., Ali, J., and Jung, J. (2022). A critical review of the recent developments in micro–nano bubbles applications for domestic and industrial wastewater treatment. *Alexandria Engineering Journal 61*, 6591–6612.

(*15*) Kilonzo, P. M., and Margaritis, A. (2004). The effects of non-Newtonian fermentation broth viscosity and small bubble segregation on oxygen mass transfer in gas-lift bioreactors: a critical review. *Biochemical Engineering Journal 17*, 27–40.

(*16*) Zhong, H., Fujii, K., Nakano, Y., and Jin, F. (2015). Effect of CO_2 Bubbling into Aqueous Solutions Used for Electrochemical Reduction of CO_2 for Energy Conversion and Storage. *The Journal of Physical Chemistry C 119*, 55–61.

(*17*) Svetovoy, V., Postnikov, A., Uvarov, I., Sanders, R., and Krijnen, G. (2016). Overcoming the fundamental limit: Combustion of a hydrogen-oxygen mixture in micro-and nano-bubbles. *Energies 9*, 94.

(*18*) Ravelli, S., Perdichizzi, A, and Barigozzi, G. (2008). Description, applications and numerical modelling of bubbling fluidized bed combustion in waste-to-energy plants. *Progress in Energy and Combustion Science 34*, 224–253.

(*19*) Babu, K., and Amamcharla, J. (2022). Application of micro-and nano-bubbles in spray drying of milk protein concentrates. *Journal of Dairy Science 105*, 3911–3925.

(*20*) Patel, S., Agarwal, R., Majumder, S. K., Das, P., and Ghosh, P. (2020). Kinetics of ozonation and mass transfer of pharmaceuticals degraded by ozone fine bubbles in a plant prototype. *Heat and Mass Transfer 56*, 385–397.

(*21*) Nguyen Hai Le, N., Sugai, Y., Nguele, R., and Sreu, T. (2021). Bubble size distribution and stability of CO2 microbubbles for enhanced oil recovery: effect of polymer, surfactant and salt concentrations. *Journal of Dispersion Science and Technology*, 1–11.

(*22*) Heseltine, P. L., Ahmed, J., and Edirisinghe, M. (2018). Developments in pressurized gyration for the mass production of polymeric fibers. *Macromolecular Materials and Engineering 303*, 1800218.

(*23*) Wu, X., and Merchuk, J. C. (2002). Simulation of algae growth in a bench-scale bubble column reactor. *Biotechnology and Bioengineering 80*, 156–168.

(*24*) Yang, G., Du, B., and Fan, L. (2007). Bubble formation and dynamics in gas–liquid–solid fluidization—A review. *Chemical engineering science 62*, 2–27.

(*25*) Pourtousi, M, Sahu, J., and Ganesan, P (2014). Effect of interfacial forces and turbulence models on predicting flow pattern inside the bubble column. *Chemical Engineering and Processing: Process Intensification 75*, 38–47.

(*26*) Saito, T., and Toriu, M. (2015). Effects of a bubble and the surrounding liquid motions on the instantaneous mass transfer across the gas–liquid interface. *Chemical Engineering Journal 265*, 164–175.

(*27*) Jimenez, M., Dietrich, N., and Hébrard, G. (2013). Mass transfer in the wake of non-spherical air bubbles quantified by quenching of fluorescence. *Chemical Engineering Science 100*, 160–171.

(*28*) Tripathi, M. K., Premlata, A. R., Sahu, K. C., and Govindarajan, R. (2017). Two initially spherical bubbles rising in quiescent liquid. *Phys. Rev. Fluids 2*, 073601.

(*29*) Pont, G., Chen, L., Spiller, D. G., and Adams, D. J. (2012). The effect of polymer additives on the rheological properties of dipeptide hydrogelators. *Soft Matter 8*, 7797–7802.

(*30*) Benchabane, A., and Bekkour, K. (2008). Rheological properties of carboxymethyl cellulose (CMC) solutions. *Colloid and Polymer Science 286*, 1173–1180.

(*31*) Ding, J., Li, W., and Z Shen, S. (2011). Research and applications of shear thickening fluids. *Recent Patents on Materials Science 4*, 43–49.

(*32*) Chhabra, R. P., and Richardson, J. F., *Non-Newtonian flow and applied rheology: engineering applications*; Butterworth-Heinemann: 2011.

(*33*) Al-Masry, W. A. (1999). Effect of scale-up on average shear rates for aerated non-Newtonian liquids in external loop airlift reactors. *Biotechnology and Bioengineering 62*, 494–498.

(*34*) Li, H. Z. (1999). Bubbles in non-Newtonian fluids: Formation, interactions and coalescence. *Chemical Engineering Science 54*, 2247–2254.

(*35*) Bird, R. B., Curtiss, C. F., Armstrong, R. C., and Hassager, O., *Dynamics of polymeric liquids, volume 2: Kinetic theory*; Wiley: 1987.

(*36*) Claassen, C. M., Islam, S., Peters, E., Deen, N. G., Kuipers, J., and Baltussen, M. W. (2020). An improved subgrid scale model for front-tracking based simulations of mass transfer from bubbles. *AIChE Journal 66*, e16889.

(*37*) Baird, M., and Davidson, J. (1962). Gas absorption by large rising bubbles. *Chemical Engineering Science 17*, 87–93.

(*38*) Bischof, F., Sommerfeld, M., and Durst, F. (1991). The determination of mass transfer rates from individual small bubbles. *Chemical Engineering Science 46*, 3115 –3121.

(*39*) Ponoth, S. S., and McLaughlin, J. (2000). Numerical simulation of mass transfer for bubbles in water. *Chemical Engineering Science 55*, 1237 –1255.

(*40*) Feng, Z.-G., and Michaelides, E. E. (2001). Heat and mass transfer coefficients of viscous spheres. *International Journal of Heat and Mass Transfer 44*, 4445 –4454.

(*41*) Saboni, A., Alexandrova, S., Spasic, A., and Gourdon, C. (2007). Effect of the viscosity ratio on mass transfer from a fluid sphere at low to very high Peclet numbers. *Chemical Engineering Science 62*, 4742 –4750.

(*42*) Huang, J., and Saito, T. (2017). Influences of gas–liquid interface contamination on bubble motions, bubble wakes, and instantaneous mass transfer. *Chemical Engineering Science 157*, 182 –199.

(*43*) Barnett, S. M., Humphrey, A. E., and Litt, M. (1966). Bubble motion and mass transfer in non-Newtonian fluids. *AIChE Journal 12*, 253–259.

(*44*) Bhavaraju, S. M., Mashelkar, R. A., and Blanch, H. W. (1978). Bubble motion and mass transfer in non-Newtonian fluids: Part I. Single bubble in power law and Bingham fluids. *AIChE Journal 24*, 1063–1070.

(*45*) Kishore, N., Chhabra, R., and Eswaran, V. (2007). Mass transfer from a single fluid sphere to power-law liquids at moderate Reynolds numbers. *Chemical Engineering Science 62*, 6040 –6053.

(*46*) Dhole, S., Chhabra, R., and Eswaran, V. (2007). Mass transfer from a spherical bubble rising in power-law fluids at intermediate Reynolds numbers. *International Communications in Heat and Mass Transfer - INT COMMUN HEAT MASS TRANS 34*, 971–978.

(*47*) Cao, B., Fan, J., Sun, X., and Li, S. (2020). Numerical Simulation of Mass-Transfer Characteristics of a Bubble Rising in Yield Stress Fluids. *ACS Omega 5*, 13878–13885.

(*48*) Vasconcelos, J. M. T., Orvalho, S. P., and Alves, S. S. (2002). Gas–liquid mass transfer to single bubbles: Effect of surface contamination. *AIChE Journal 48*, 1145–1154.

(*49*) Gómez-Díaz, D., Gomes, N., Teixeira, J., and Belo, I. (2007). Oxygen mass transfer to emulsions in a bubble column contactor. *Chemical Engineering Journal 152*, 354–360.

(*50*) Clift, R., Grace, J., and Weber, M. In 1978.

(*51*) Coppus, J., and Rietema, K. (1980). Theoretical derivation of the mass transfer coefficient at the front of a spherical cap bubble. *Chemical Engineering Science 35*, 1497–1499.

(*52*) Kendoush, A. A. (1994). Theory of convective heat and mass transfer to spherical-cap bubbles. *AIChE Journal 40*, 1440–1448.

(*53*) Kendoush, A. A. (2007). Heat, Mass, and Momentum Transfer to a Rising Ellipsoidal Bubble. *Industrial & Engineering Chemistry Research 46*, 9232–9237.

(*54*) Bhaga, D., and Weber, M. (1980). In-line interaction of a pair of bubbles in a viscous liquid. *Chemical Engineering Science 35*, 2467–2474.

(*55*) Katz, J., and Meneveau, C. (1996). Wake-induced relative motion of bubbles rising in line. *International Journal of Multiphase Flow 22*, 239–258.

(*56*) Watanabe, M., and Sanada, T. (2006). In-Line Motion of a Pair of Bubbles in a Viscous Liquid. *JSME International Journal Series B Fluids and Thermal Engineering 49*, 410–418.

(*57*) Sanada, T., Sato, A., Shirota, M., and Watanabe, M. (2009). Motion and coalescence of a pair of bubbles rising side by side. *Chemical Engineering Science 64*, 2659–2671.

(*58*) Kusuno, H., and Sanada, T. (2015). EXPERIMENTAL INVESTIGATION OF THE MOTION OF A PAIR OF BUBBLES AT INTERMEDIATE REYNOLDS NUMBERS. *Multiphase Science and Technology 27*, 51–66.

(*59*) Kusuno, H., Yamamoto, H., and Sanada, T. (2019). Lift force acting on a pair of clean bubbles rising in-line. *Physics of Fluids 31*, 072105.

(*60*) Yuan, H., and Prosperetti, A. (1994). On the in-line motion of two spherical bubbles in a viscous fluid. *Journal of Fluid Mechanics 278*, 325–349.

(*61*) Chen, L., Garimella, S. V., Reizes, J. A., and Leonardi, E. (1997). Motion of interacting gas bubbles in a viscous liquid including wall effects and evaporation. *Numerical Heat Transfer, Part A Applications 31*, 629–654.

(*62*) Hasan, N., and binti Zakaria, Z. (2011). Computational approach for a pair of bubble coalescence process. *International Journal of Heat and Fluid Flow 32*, 755–761.

(*63*) Chen, R., Tian, W., Su, G., Qiu, S., Ishiwatari, Y., and Oka, Y. (2011). Numerical investigation on coalescence of bubble pairs rising in a stagnant liquid. *Chemical Engineering Science 66*, 5055–5063.

(*64*) Zhang, Y., Chen, K., You, Y., and Ren, W. (2018). Coalescence of two initially spherical bubbles: Dual effect of liquid viscosity. *International Journal of Heat and Fluid Flow 72*, 61–72.

(*65*) Cao, Y., and Macián-Juan, R. (2021). The wobbling motion of single and two inline bubbles rising in quiescent liquid. *Physics of Fluids 33*, 073305.

(*66*) Kumar, A., Ray, B., and Biswas, G. (2021). Dynamics of two coaxially rising gas bubbles. *Physics of Fluids 33*, 052106.

(*67*) Vélez-Cordero, J. R., Sámano, D., Yue, P., Feng, J. J., and Zenit, R. (2011). Hydrodynamic interaction between a pair of bubbles ascending in shear-thinning inelastic fluids. *Journal of Non-Newtonian Fluid Mechanics 166*, 118–132.

(*68*) Fan, W., and Yin, X. (2013). Numerical Study on Interaction Between Two Bubbles Rising Side by Side in CMC Solution. *Chinese Journal of Chemical Engineering 21*, 705–713.

(*69*) Islam, M. T., Ganesan, P., and Cheng, J. (2015). A pair of bubbles' rising dynamics in a xanthan gum solution: a CFD study. *RSC Adv. 5*, 7819–7831.

(*70*) Liu, J., Zhu, C., Wang, X., Fu, T., Ma, Y., and Li, H. (2015). Three-dimensional numerical simulation of coalescence and interactions of multiple horizontal bubbles rising in shear-thinning fluids. *AIChE Journal 61*, 3528–3546.

(*71*) Sun, W., Zhu, C., Fu, T., Ma, Y., and Li, H. (2019). 3D simulation of interaction and drag coefficient of bubbles continuously rising with equilateral triangle arrangement in shear-thinning fluids. *International Journal of Multiphase Flow 110*, 69–81.

(*72*) Sun, W., Zhu, C., Fu, T., Ma, Y., and Li, H. (2020). Interaction and drag coefficient of three horizontal bubbles with different sizes rising in the shear-thinning fluids. *International Journal of Multiphase Flow 125*, 103214.

(*73*) Li, S., Liu, M., Hanaor, D., and Gan, Y. (2018). Dynamics of Viscous Entrapped Saturated Zones in Partially Wetted Porous Media. *Transport in Porous Media 125*.

(*74*) Yasuda, K. (2006). A multi-mode viscosity model and its applicability to non-Newtonian fluids. *Journal of Textile Engineering 52*, 171–173.

(*75*) Yasuda, K., Armstrong, R. C., and Cohen, R. E. (1981). Shear flow properties of concentrated solutions of linear and star branched polystyrenes. *Rheologica Acta 20*, 163–178.

(*76*) Bergman, T., Bergman, T., Incropera, F., DeWitt, D., and Lavine, A., *Fundamentals of Heat and Mass Transfer*; Wiley: 2011.

(*77*) Gueyffier, D., Li, J., Nadim, A., Scardovelli, R., and Zaleski, S. (1999). Volume-of-Fluid Interface Tracking with Smoothed Surface Stress Methods for Three-Dimensional Flows. *Journal of Computational Physics 152*, 423–456.

(*78*) Brackbill, J., Kothe, D., and Zemach, C (1992). A continuum method for modeling surface tension. *Journal of Computational Physics 100*, 335–354.

(*79*) Ahmed, B., Hayat, T, Alsaedi, A, and Abbasi, F. M. (2020). Entropy generation analysis for peristaltic motion of Carreau–Yasuda nanomaterial. *Physica Scripta 95*, 055804.

(*80*) Lashgari, I., Pralits, J. O., Giannetti, F., and Brandt, L. (2012). First instability of the flow of shear-thinning and shear-thickening fluids past a circular cylinder. *Journal of Fluid Mechanics 701*, 201–227.

(*81*) Coclite, A., Coclite, G. M., and De Tommasi, D. (2020). Capsules Rheology in Carreau–Yasuda Fluids. *Nanomaterials 10*.

(*82*) Popinet, S. Solitary wave run-up on a plane beach, `http://basilisk.fr/src/test/beach-ml.c`, 2019.

(*83*) Karnakov, P., Litvinov, S., and Koumoutsakos, P. (2020). A hybrid particle volume-of-fluid method for curvature estimation in multiphase flows. *International Journal of Multiphase Flow 125*, 103–209.

(*84*) López-Herrera, J., Popinet, S., and Castrejón-Pita, A. (2019). An adaptive solver for viscoelastic incompressible two-phase problems applied to the study of the splashing of weakly viscoelastic droplets. *Journal of Non-Newtonian Fluid Mechanics 264*, 144–158.

(*85*) Popinet, S. (2009). An accurate adaptive solver for surface-tension-driven interfacial flows. *Journal of Computational Physics 228*, 5838–5866.

(*86*) Brereton, G, and Korotney, D (1991). Coaxial and oblique coalescence of two rising bubbles. *Dynamics of bubbles and vortices near a free surface 119*, 50–73.

(*87*) Chakraborty, I., Biswas, G., and Ghoshdastidar, P. (2013). A coupled level-set and volume-of-fluid method for the buoyant rise of gas bubbles in liquids. *International Journal of Heat and Mass Transfer 58*, 240–259.

(*88*) Bhaga, D., and Weber, M. E. (1981). Bubbles in viscous liquids: shapes, wakes and velocities. *Journal of Fluid Mechanics 105*, 61–85.

(*89*) Clift, R., Grace, J. R., and Weber, M. E. In Courier Corporation: 2005.

(*90*) Tripathi, M., Sahu, K., and Govindarajan, R. (2015). Dynamics of an initially spherical bubble rising in quiescent liquid. *Nature communications 6*, 6268.

(*91*) Zhang, L., Yang, C., and Mao, Z.-S. (2010). Numerical simulation of a bubble rising in shear-thinning fluids. *Journal of Non-Newtonian Fluid Mechanics 165*, 555–567.

(*92*) Premlata, A., Tripathi, M. K., Karri, B., and Sahu, K. C. (2017). Numerical and experimental investigations of an air bubble rising in a Carreau-Yasuda shear-thinning liquid. *Physics of fluids 29*, 033103.

(*93*) Roudet, M., Billet, A.-M., Cazin, S., Risso, F., and Roig, V. (2017). Experimental investigation of interfacial mass transfer mechanisms for a confined high-reynolds-number bubble rising in a thin gap. *AIChE Journal 63*, 2394–2408.

(*94*) Guimerà, R., Reichardt, I., Aguilar-Mogas, A., Massucci, F. A., Miranda, M., Pallarès, J., and Sales-Pardo, M. (2020). A Bayesian machine scientist to aid in the solution of challenging scientific problems. *Science Advances 6*.

(*95*) Vela-Martín, A., and Avila, M. (2021). Deformation of drops by outer eddies in turbulence. *Journal of Fluid Mechanics 929*, A38.

(*96*) Cano-Lozano, J. C., Martínez-Bazán, C., Magnaudet, J., and Tchoufag, J. (2016). Paths and wakes of deformable nearly spheroidal rising bubbles close to the transition to path instability. *Phys. Rev. Fluids 1*, 053604.

(*97*) Talaia, M. (2007). Terminal Velocity of a Bubble Rise in a Liquid. *World Acad. Sci. Eng. Technol. 28*.

(*98*) Heynderickx, G., Kuipers, J., van Swaaij, M., and Zijlmans, P. (2001). Bubble size distribution in bubbly flows: a review. *Chemical Engineering Science 56*, 6465–6488.

(*99*) Saba, N., Iqbal, M., Inayat, A., Hussain, A., and Mehmood, T. (2018). Dynamics of gas bubbles rising in non-Newtonian fluids: A review. *Chemical Engineering Science 184*, 1–27.

(*100*) Xiong, Q., Zhang, Z., Cai, J., and et al. (2019). Effects of shear-thinning behavior on gas bubble dynamics in a high-viscosity liquid. *Chemical Engineering Science 206*, 85–94.

UNIVERSITAT ROVIRA I VIRGILI,
NUMERICAL INVESTIGATION OF A SINGLE BUBBLE AND A PAIR OF BUBBLES RISING IN NEWTONIAN AND NON NEWTONIAN FLUIDS WITH INTERFACIAL PASSIVE SCALAR TRANSFER
Koorosh Kazemi

UNIVERSITAT
ROVIRA i VIRGILI